# Multiferroic properties of doped-$BiFeO_3$ nanoparticles

A THESIS

Submitted to the

FACULTY OF SCIENCE

THAPAR UNIVERSITY, PATIALA

for the degree of

**Doctor of Philosophy**

By

**GITANJALI DHIR**

Regn. No. 901112007

School of Physics & Materials Science

Thapar University

Patiala - 147 004

INDIA

**July 2016**

## DECLARATION

It is certified that the thesis is entirely my own and that the ideas and references cited herein have been duly acknowledged.

(Gitanjali Dhir)

Attestation by supervisor

(Dr. N. K. Verma)

Visiting Professor

School of Physics and Materials Science,

Thapar University,

Patiala – 147 004

INDIA

Attestation by co-supervisor

(Dr. Poonam Uniyal)

Assistant Professor

School of Physics and Materials Science,

Thapar University,

Patiala – 147 004

INDIA

# CERTIFICATE

This is to certify that the thesis entitled, "**Multiferroic properties of doped-$BiFeO_3$ nanoparticles**", submitted by **Ms. Gitanjali Dhir** in the fulfilment of the requirement for the award of the degree of Doctor of Philosophy in the School of Physics and Materials Science, Thapar University, Patiala, is a record of candidate's own work carried out by her under my supervision and guidance. The matter presented in this thesis has not been submitted in part or full for the award of any degree in any other University or Institute.

Attestation by supervisor

**(Dr. N. K. Verma)**

Visiting Professor

School of Physics and Materials Science,

Thapar University,

Patiala – 147 004

Attestation by co-supervisor

**(Dr. Poonam Uniyal)**

Assistant Professor

School of Physics and Materials Science,

Thapar University,

Patiala – 147 004

TO

MY BELOVED

FAMILY

# ACKNOWLEDGEMENT

**I humbly prostrate myself before the Almighty for HIS grace and abundant blessings that he has bestowed on me.**

*Foremost, I would like to express my profound gratitude to my supervisor Dr. N. K. Verma and co-supervisor Dr. Poonam Uniyal for their continuous guidance. motivation, enthusiasm, and wholehearted support. They shared with me a lot of their expertise and research insight. They provided me with persistent encouragement and wholehearted support throughout my work. Their undying passion in research inspired and enriched my growth. Their thoughtful advices always motivated me to take every failure in a positive stride and work even harder towards my goal. It served to give me a sense of direction during my PhD studies and helped me in completing my project in the present form. A heartfelt gratitude to Mrs. (Dr.) Rama Verma for her motherly affection.*

*I am highly obliged to BRNS, Government of India, for awarding me fellowship to pursue my doctoral work.*

*I wish to thank my doctoral committee members, Dr. Puneet Sharma, Dr. Bhaskar Chandra Mohanty, and Dr. Amjad Ali, for carefully scrutinizing the progress of my research work and thoughtful discussions during the hour of need.*

*I am heartily thankful to Dr. Parkash Gopalan, Director, Thapar University, Dr. Manoj Sharma, Professor and Head, School of Physics and Materials Science, Dr. O. P. Pandey, Dean of Research and Sponsored Projects, and the entire faculty of School of Physics and Materials Science for all their encouragement and support.*

*I deeply acknowledge the non-teaching and secretarial staff for all their needful assistance.*

*I would like to record my gratitude towards my seniors and fellow research scholars, Dr. Sanjeev Kumar, Dr. Lavanya Khanna, Dr. Manveen Kaur, Dr. Gurmeet Singh, Dr. Jaspal and Mrs. Kamaldeep Kaur, who played a vital role in this journey of mine and contributed in their own ways towards the fulfilment of my research work. I am tempted to individually thank my friends and best pals Ms. Rajni Mittal, Mr. Pritampal Singh, Mr. Gaurav Kalia, Mr. Kirpal Singh, Mr. Bhupinder Pal Thakur, Mr. Sharad Tiwari, Mr. Arvind Kumar, Ms. Parminder Kaur, Ms. Anju, Ms. Megha Bhushan, Ms .Monika Bharti, Mr. Nikhil Gakkhr, and Mr. Rehman who have genuinely stuck with me through thick and thin.*

*I cannot finish without saying how indebted I am to my family. My parents deserve a very special mention for their everlasting love, inseparable support, and invariable prayers that they blessed me with. My father, Mr. YashPal Dhir, in the first place is the person, who explained to me the joy of hard work ever since I was a child. He is my source of inspiration. My mother, Mrs. Shobha Devi is the pillar of my life. Her passion to see me successful is the driving force inside me. Every time I have fallen, they stood by me as my pillars of strength and pulled me up that reassured my belief in myself. Words of wisdom that I get from them always guide me as my torch-bearers. They have always motivated and inspired me to do my best in all matters of life and left no stone unturned to see me successful and happy. My siblings, Ms. Shallu Dhir and Mr. Hitesh Dhir, whom I madly adore, are my best companions. Their smiling faces just brighten my day. To my family, I dedicate this thesis with all my love and respect - Mum, Dad and My siblings.*

*A sincere gratitude to my grandmother, Late Mrs. Ram Pyari Chopra, my aunt, Mrs. Sushma and my cousins (Mr. Rajeev Kumar, Ms. Preet Rashmi and Mr. Tarun Kumar) for all their unconditional love, support, care and blessings, at the time me and my family needed it the most.*

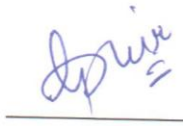

**(Gitanjali Dhir)**

# *CONTENTS*

**Chapter 2 Materials and characterization**

**Chapter 3 Rare earth metal ions doped-$BiFeO_3$ nanoparticles**

# *LIST OF FIGURES*

# *LIST OF TABLES*

# *List of Publications*

## I. Papers published in SCI Journals

1. Gitanjali Dhir, Gurmeet Singh Lotey, Poonam Uniyal, N. K. Verma, Size-dependent magnetic and dielectric properties of Tb-doped $BiFeO_3$ nanoparticles, J Mater. Sci.: Mater. Electron. 24 (2013) 4386-4392.
2. Gitanjali Dhir, Poonam Uniyal, N. K. Verma, Effect of particle size on magnetic and dielectric properties of nanoscale Dy-doped $BiFeO_3$, J. Supercond. Nov. Magn. 27 (2014) 1569–1577.
3. Gitanjali Dhir, Poonam Uniyal, N. K. Verma, 'Effect of particle size on multiferroism of barium-doped bismuth ferrite nanoparticles', Mater. Sci. Semicond. Process. 27 (2014) 611–61.
4. Gitanjali Dhir, Poonam Uniyal, N. K. Verma, Enhancement in magnetic and electrical properties of $Bi_{0.95}Tb_{0.05}FeO_3$ nanoparticles with reducing size, J. Mater. Sci.: Mater. Electron. 26 (2015) 3538-3544.
5. Gitanjali Dhir, Poonam Uniyal, N. K. Verma, Sol–gel synthesized $BiFeO_3$ nanoparticles: Enhanced magnetoelelctric coupling with reduced particle size, J. Magn. Magn. Mater. 394 (2015) 372-378.
6. Gitanjali Dhir, Poonam Uniyal, N. K. Verma, Effect of particle size on multiferroic properties of Tb-doped $BiFeO_3$, J. Supercond. Nov. Magn. (2016) 1-8.
7. Gitanjali Dhir, Poonam Uniyal, N. K. Verma, 'Sol-gel synthesized Sr-doped $BiFeO_3$ nanoparticles : Enhanced multiferroic properties with reduced particle size', Mater. Sci. in Semicond. Process. (Under review with minor revisions).

## II. Papers in Non-SCI Journals

1. Gurmeet Singh Lotey, Gitanjali Dhir, N. K. Verma, Effect of reduced size and Ba doping on multiferroic properties of $BiFeO_3$ nanoparticles, AIP Conference Proceedings 1536 (2013) 969-970.

2. Gitanjali Dhir, Poonam Uniyal, N. K. Verma, Room temperature magnetization in nanoscale $BiFeO_3$, Excel India Publishers (2013) 2149 – 2153.

3. Gitanjali Dhir, Poonam Uniyal, N.K. Verma, Study on structural, morphological and ferroelectric properties of $0.8BiFeO_3$-$0.2BaTiO_3$ nanocomposite, International Conference on Nanotechnology in the Service of Health, Environment & Society, February 13 – 15, 2014 (Panjab University, Chandigarh).

4. Calcination temperature influenced multiferroic properties of Ca-doped $BiFeO_3$ nanoparticles, Gitanjali Dhir, Poonam Uniyal, N. K. Verma, AIP Conference Proceedings (2014) 149.

## III. Papers in Conference Proceedings

1. Gitanjali Dhir, Poonam Uniyal, N. K. Verma, Particle size dependence of multiferroic properties of Tb-doped $BiFeO_3$ nanoparticles, Winter School-2014 on Frontiers in Materials Science, 41, 1-5 December 2014 JNCASR, Bengaluru.
2. Gitanjali Dhir, Poonam Uniyal, N. K. Verma, Size dependent multiferroism in $Bi_{0.90}Tb_{0.10}FeO_3$ nanoparticles, Third International Conference on Nanotechnology for Better Living, 25-29 May 2016, NIT Srinagar.

## IV. Conference Presentations

1. Gitanjali Dhir, Poonam Uniyal, N.K. Verma, Size dependent multiferroism in Tb-doped $BiFeO_3$ nanoparticles, $6^{th}$ National Symposium for Materials Research Scholars, MR-14, 12 – 14 May, 2014 (IIT Bombay, Mumbai).

2. Gitanjali Dhir, Poonam Uniyal, N.K. Verma, Synthesis and characterization of Tb-doped $BiFeO_3$ nanoparticles, CP_26, Poster presentation in National Symposium on Electroceramics Materials and Devices, 21-22 February, 2014 (G.V.M. Girls College, Sonepat).

3. Gitanjali Dhir, N. K. Verma, Multiferroic properties of ferroelectric-ferromagnetic based nanocomposites, CP-06, Poster presentation in National Conference on Functional Materials, 24-25 September, 2012 (G.V.M. Girls College, Sonepat).

# *Abstract*

With the semi-conductor industry facing threats of reaching fundamental limits further miniaturization is not possible. Current trends toward device miniaturization and high-density data storage system thus necessitate integration of multifunctions into a single material. Multiferroics, the rare class of compounds exhibiting co-existence of two or more ferroic orders serves the contemporary demands. Significant advancements in the atomic and nanoscale growth and characterization techniques achieved with the developments in the field of nanotechnology pave the way for multifunctional nanostructural materials. These nanostructured multiferroics offer plenty of horizons for future technology because of the tunability of properties with size and morphology.

Bismuth ferrite ($BiFeO_3$) – the most widely studied single phase multiferroic system in the literature displays room temperature ferroelectric (1100 K) and magnetic (640 K) order that makes it unique of its kind. Though this feature being promising for utilization in devices however, has failed hitherto. Its application is hampered by several serious issues that involve high leakage currents (mainly arising due to oxygen and bismuth vacancies, non-stoichiometery, secondary phase impurities and defects caused by the volatile nature of Bi), and no net magnetization (mainly arising due to incommensurate spin spiral structure of wavelength 62 nm superimposed over G-type antiferromagnetic ordering), which thus leads to low magnetoelectric coupling in $BiFeO_3$. Many studies are devoted to eradicate these problems over the time. Reviewing the literature one observes the rare earth and alkaline earth metal ions-doping and reduction of the size to nanoscale are helpful in addressing these issues.

Particle size plays a crucial role in deciding the overall multiferroic properties of $BiFeO_3$ nanoparticles. Various aspects (structural, magnetism, dielectric behaviour, magnetic transition temperature, photocatalytic activity, etc.) of $BiFeO_3$ nanoparticles scrutinizing their influence on particle size have been studied in details. However, it has been found that not much of studies have been carried out to investigate the influence of the particle size on the multiferroic properties of rare earth and alkaline earth metal ions doped $BiFeO_3$ nanoparticles.

In a nutshell, the present thesis attempts to study the influence of particle size on rare earth and alkaline earth metal ions-doped $BiFeO_3$ nanoparticles . Altogether, six combinations (rare earth (Tb, Dy, Gd) and alkaline earth (Ca, Sr, Ba) metal-doped $BiFeO_3$ nanoparticles) have been studied, which are synthesized using sol-gel method. Their structural, morphological, magnetic, dielectric and ferroelectric analyses have been done by X-ray diffractometer (XRD), Scanning electron microscope/Transmission electron microscope (SEM/TEM), Vibrating sample magnetometer (VSM), LCR meter and P-E loop tracer, respectively. Remarkable influence of particle size on magnetic, dielectric and ferroelectric properties of rare earth and alkaline earth metal ions-doped $BiFeO_3$ has been witnessed. Rare earth metals in comparison to alkaline earth metals have been found to display enhanced magnetic, dielectric and ferroelectric values. Amongst the six ions, $Dy^{3+}$ ions - doped $BiFeO_3$ nanoparticles have been observed to exhibit the maximum enhancement of multiferroic (desirable for device application) properties owing to its smallest ionic radii and highest magnetic moment.

## *Thesis Structure*

In the present thesis, rare (Tb, Dy, Gd) and alkaline earth (Ca, Sr, Ba) metal-doped $BiFeO_3$ nanoparticles of different particle size have been studied. The undoped $BiFeO_3$ nanoparticles of different particle size have also been studied. Therefore, two sections (chapter 3 and chapter 4) have been prepared comprising of three dopants each. One is about rare earth (Tb, Dy and Gd)-doped $BiFeO_3$ nanoparticles. The other deals with alkaline earth (Ca, Sr and Ba)-doped $BiFeO_3$ nanoparticles. The structural, morphological, magnetic, dielectric and ferroelectric analyses of all the combinations mentioned above have been studied. Following is the chapter-wise description of the thesis.

**Chapter 1 - Introduction**

This chapter covers brief and selective introduction to electric and magnetic materials and nanotechnology highlighting the emergence of the multiferroics. The essential details related to the multiferroic materials have been discussed, covering the literature work reported so far. It also includes the insight and grounds on which the objectives for the present thesis were shaped.

**Chapter 2 - Synthesis and characterization techniques**

This chapter provides an overview of the synthesis method used for preparing rare (Tb, Dy, Gd) and alkaline (Ca, Sr, Ba) earth metal ions doped $BiFeO_3$ nanoparticles. The various characterization techniques such as X-ray diffraction (XRD), Transmission electron microscope (TEM), Scanning electron microscope (SEM), Vibrating sample magnetometer

(VSM), LCR meter and P-E loop tracer have been explained in detail. The working principle and instrumentation of all the techniques mentioned above have been covered.

**Chapter 3 - Rare earth doped $BiFeO_3$ nanoparticles**

The present chapter includes the experimental procedures followed for synthesizing rare earth metal ions (Tb, Dy, Gd)-doped $BiFeO_3$ nanoparticles and their particle size variation. Their structural, morphological, magnetic, dielectric and ferroelectric properties have been studied.

**Chapter 4 – Alkaline earth metal ions-doped $BiFeO_3$ nanoparticles**

The present chapter includes the experimental procedures for synthesizing alkaline earth metal ions (Ca, Sr, Ba)-doped $BiFeO_3$ nanoparticles and their particle size variation. Their structural, morphological, magnetic, dielectric and ferroelectric properties have been studied.

**Chapter 5 - Conclusions and future possibilities**

This chapter summarizes the conclusions of the research work presented in the thesis. Also, it gives an insight into the future possibilities for augmentation of the work.

# *Chapter 1*

# *INTRODUCTION*

# Chapter 1

The interplay between electricity and magnetism has fascinated researchers over centuries and has had tremendous impact on the technology. This chapter covers brief introduction to ferroelectric and magnetic materials highlighting the emergence of nanotechnology in the existing device technology. However, the current trends toward device miniaturization demands alternate new multifunctional materials as the semiconductor-based electronic industry is at the verge of fundamental limit of integration. The obscure class of materials, 'multiferroics', is presented as a solution. Their brief definition, history, essential requirements and applications have been discussed.

## 1.1 Introduction

The interplay between electricity and magnetism – fundamental tenet of the classical theory of electromagnetism was at first uncovered by Oersted by an accident in 1820 [1]. It involved deflection of magnetic needle on switching on or off of a battery in its vicinity [1-2]. Following this accidental observation, forty years later, the classical theory of electromagnetism was worked out with decisive contributions from the likes of Ampère and Faraday [3]. The key clues from these experiments, illustrating generation of magnetic fields by electric currents, led to formulation of James Maxwell's equations in 1860. The unified theory magically describes all the physical phenomena governed by the electromagnetic interactions - one of the four fundamental physical forces [2]. The link between magnetism and electricity has remarkably influenced the technology. Materials science defines these two phenomena separately: spin of the electron leads to magnetism while charge of the electron yields electricity [3-6]. Magnetism is a relativistic quantum mechanical second order effect coupled with the spin of the electron and follows the Pauli's exclusion principle for spin of

the electron. However, in electricity the electrostatic Coulomb interaction is the dominant force [3].

Magnetic and ferroelectric materials are time-privileged research subjects that have bagged lot of scientific and technological discoveries. Almost a century ago, large piezoelectric coefficient was observed in Rochelle salt - the first material that commenced the study on ferroelectric materials [7]. Ferroelectricity in one of the most popular perovskite i.e. $BaTiO_3$ was observed in 1940. It invigorated research in the field of ferroelectrics for discovering new ferroelectric materials and their characterization. The basic understanding of fundamentals of ferroelectrics had increased enormously with passing years, and thus, their optimization had successfully resulted in a wide range of applications such as non-volatile memories, promoting the data storage, transducers, actuators and capacitors [6].

Magnetic materials have had a prodigious impact on the science and technology. The research interest drives from the urge to understand its fundamentals and demands of new device applications. The advancement in growth at atomic- and nano scales as well as the related characterization techniques have allowed exhibition of intriguing phenomena by magnetic materials [6]. Some of the important applications are: Enhanced density of storing data, magnetic valves, spin transistors etc. Based on giant and colossal magnetoresistance effect (conductivity tuned by magnetic fields) some applications are memories, sensors and read heads.

Though, the functional magnetic and electronic materials plinth the existing technology, the present day technology is following trend towards device miniaturization. The field of nanotechnology, dealing with the control of matter at atomic scale leading to fabrication of advanced materials with superior performance for device applications, is now maturing rapidly and has invaded all the facets of science and technology [8-14]. The term ‘nano’

derived from the Greek prefix means dwarf and describes one billionth ($10^{-9}$) of a meter [15-17]. The dimension that typically falls in the nanoregime spans from subnanometer to several hundred nanometers [16]. Its inspiration is often referred to R. Feynman's famous talk, entitled 'There is plenty of room at the bottom', to the American Physical Society, in 1965 [18]. The researchers are euphoric about it as novel properties are inherent to the nanosized systems. On moving down from micro to nano scale almost all the physical and chemical properties change drastically [17]. Precisely, this occurs due to large surface to volume ratio, discretion of energy bands, Coulomb blockade and quantum confinement [15-17]. The appropriate variations in size and shape thus enables the tuning of the properties of nanomaterials such as mechanical strength, ductility, melting point, lattice constant, electrical conductivity, thermal conductivity, density, elastic modulus, magnetism etc. [18]. This allows the material to be manipulated as simply as software, which is highly fruitful for the advancement of existing technology.

Though, the cognizance of nanotechnology is new, but research at nanoscale dates back to thousand years ago [18]. Most significant applications of nanotechnology have been found in ferroelectric and magnetic nanostructures based devices. These nanostructures provide highly efficient device applications with novel phenomena. The current fever of nanotechnology derives from the demand of ever shrinking size of devices in the semiconductor industry along with availability of characterization as well as manipulation techniques at the nano scale. The decreasing device dimension follows observation by Gordon E. Moore in 1965 popularly known as Moore's law [19-20]. It states that device dimension gets half approximately every eighteen months [20]. Today's transistors have reached at the edge of fundamental limits i.e. atomic level. Thus, for further miniaturization the current scenario desires materials that are able to perform multifunctional tasks.

Multifunctional nanomaterials best suits the demand. These combine various properties in a material to generate a single device component that can perform more than one task. Multifunctional materials, also known as ‘multiferroics’, are particularly appealing from this point of view. These possess not only the properties of their parent compounds, but also interactions between these properties lead to additional functionalities.

## 1.2 Multiferroics

### 1.2.1 Definition

‘Multiferroics’ represent an uncommon class of materials having simultaneous existence of two or more ferroic orders in the same phase [21-22]. The schematic illustration of the combination of a ferroelectric and ferromagnetic is shown in Fig. 1.1.

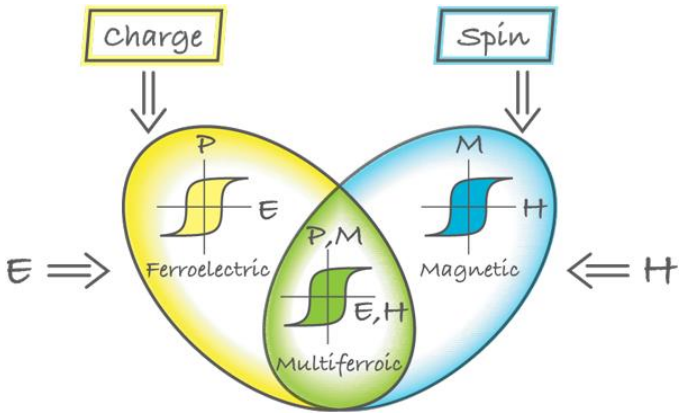


Fig. 1.1 Schematic illustrating multiferroic materials combining the properties of ferroelectrics and magnets where, the magnetic field (H) results in magnetization in ferromagnet (blue), similar to the behavior of ferroelectrics (yellow) on the application of electric field (E). The multiferroics (green) that are simultaneously ferroelectric and ferromagnetic, possess magnetic response to an applied electric field, and, vice versa [5]

### 1.2.2 Ferroics

Compounds that possess one of the four ferroic properties, namely, ferroelasticity, ferroelectricity, ferromagnetism and ferrotoroidicity are known as ferroics [23-24]. It is a material that possesses switchable and spontaneous alignment of ferroic orders [23]. These involve appearance of their respective ferroic order (i.e. strain, spontaneous polarization, magnetization or toroidal moment) during phase transition from higher to lower temperature. The transition reduces symmetry and splits the ferroic phase in domains. These order parameters are switchable in nature and switching results in hysteretic dependence of the order parameter on its respective conjugated field (mechanical stress, electric field, magnetic field and toroidal source vector) [24]. The hysteretic and domain switching of the four ferroic order parameters is illustrated in Fig. 1.2.

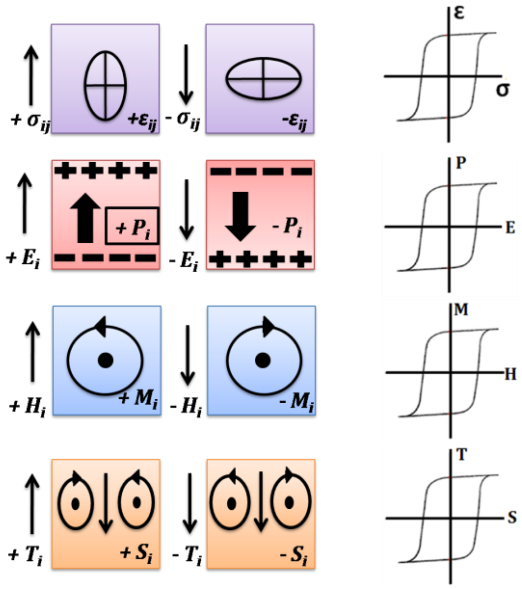


Fig. 1.2 Schematic of domain and hysteretic switching in the four ferroic order parameters by its conjugated field [23]

The glossary of various ferroic orders is given below [25].

**a) Ferroelastic**

It is the property by virtue of which spontaneous deformation ($\varepsilon$ ) displays hysteresis on application of stress ($\sigma$).

**b) Ferroelectric**

It is the property by virtue of which spontaneous polarization (P) displays hysteresis on application of application of electric field (E).

**c) Ferromagnetic**

It is the property by virtue of which spontaneous magnetization (M) displays hysteresis on application of magnetic field (H).

**d) Ferrotoroidic**

It is the property by virtue of which spontaneous order parameter (T) displays hysteresis on application of curl of magnetization or polarization (ExH).

**e) Antiferroelectric**

It is the property by virtue of which ordered dipole moments cancel each other completely within the crystallographic unit cells.

**f) Antiferromagnet**

It is the property by virtue of which ordered magnetic moments cancel each other with in the magnetic unit cells.

All ferroics individually, are of great interest because of both basic physics and technological applications (ferroelectric or magnetic memories, transducers, actuators, capacitors, magnetic valves, spin transistors, etc.). However, multiferroics possessing the co-existence and coupling of these ferroic orders are technologically more prosperous and thus are a focal point of research.

### 1.2.3 Multiferroism

The term 'multiferroic' was first coined by H. Schmid in 1994 to address the materials exhibiting co-existence of two or more primary ferroic orders [26]. However, recent trends exclude the necessity of ferroelasticity and include ferrotoroidic order in principle [25]. Initially, these materials were said to comprise of compounds with two or more ferroic orders. However, as of today, they also include materials with an antiferroic order [27-28].

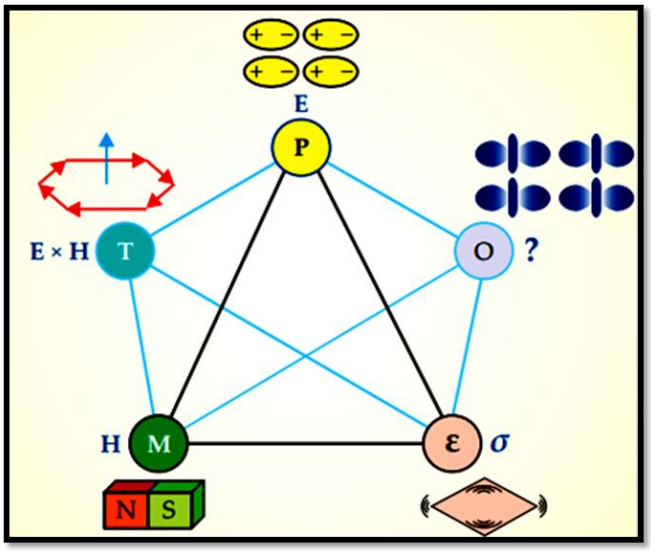


Fig. 1.3 Various ferroic orders and interactions in multiferroics [3]

Fig. 1.3 illustrates the primary ferroic orderings: ferroelectricity, ferrotoroidicity, ferromagnetism and ferroelasticity switchable by their respective conjugate fields i.e. electric, crossed electric and magnetic fields, stress, and magnetic fields. The 'O' denotes other

possibilities for example spontaneous switchable vortices, orbital orderings and chiralities, which are intriguing for upcoming research [3]. Thus, the addressable number of order parameters (chirality, orbital ordering and toroidal moment) has enhanced and discovering their respective conjugate fields further increase the range of parameters for tuning and coupling functionalities in multiferroics. This inspires the physicists to dream entirely new list of devices, which exploits its unique and novel functionalities.

*The present thesis focuses on the multiferroic materials having electric and magnetic orders.*

The glossary of parameters generated due to the coupling of ferroic orders is given below [25].

**a) Magnetoelectric (ME) coupling**

These illustrate the appearance of electric polarization on application of magnetic field and vice versa.

**b) Magnetostriction**

These illustrate quadratically varying strain with the applied magnetic field.

**c) Piezomagnetism**

These illustrate linearly varying strain with the applied magnetic field and vice versa.

**d) Piezoelectricity**

These illustrate linearly varying strain with the applied electric field and vice versa.

**e) Electrostriction**

These illustrate quadratically varying strain with the applied electric field.

These materials possess all the potential applications exhibited by the ferromagnetic, ferroelastic and ferroelectric materials. Moreover, in multiferroics, the order parameters possess ability to couple with each other such as the magnetic and the electric polarization [6]. The coupling of the order parameters offers an extra degree of freedom in the device design [6]. The coupling allows the order parameters to be tuned by the fields other than their respective conjugate fields [25]. The coupling between electric and magnetic orders, known as ME coupling, is of immense significance and possesses high potential in device applications [29]. Hence, multiferroics offer a wide range of opportunity for potential applications. Some of the important applications are listed below.

**a) Multiple state memory**

One important application is multiple state memories. It involves coupling of magnetic and electric orders, which offer design of magnetic random access memory (MRAM) having an electrical writing method (MERAM) or ferroelectric memories having a non-destructive magnetic reading. These possess the potential to replace the existing memory elements in near future [6].

**b) Other applications**

Multiferroic materials lead to better technology by contributing towards advancements in extremely desired device miniaturization. These materials possess tremendous potential for applications such as electrically tunable ferromagnetic resonance devices and microwave devices, spintronic devices, spin valves, solid-state transformers, transducers with magnetically modulated piezoelectricity, highly sensitive magnetic field sensors, quantum electromagnets, electromagneto optic

actuators, optoelectronics, sensors, microelectronic devices, magnetic-electric sensors in radioelectronics, microwave electronics and non-volatile data storage [2, 30-32].

**c) Some novel applications**

Apart from the electric control of magnetism, this class of materials reveal novel applications such as the electric control of resonances resulting in electrically controlled microwave device prototypes; discovery of domain wall associated functionalities for instance magnetotransport; vortex formation and electrical conduction, which could facilitate electrical control of nanoscale storage [3].

Besides the technological perspectives, the quest to unfold the fundamental physics involved in the coupling of order parameters makes this field intriguing. Hence, attracts interests of the researchers worldwide.

However, this class of materials is rare. A few multiferroic materials exist in nature, namely, congolite ($Fe_3B_7O_{13}Cl$) and chambersite ($Mn_3B_7O_{13}Cl$) crystals [33]. The following section shares a brief description on the factors limiting the coexistence of magnetism and ferroelectricity in a single phase.

### 1.2.4 Scarcity

#### 1.2.4.1 Symmetry

The symmetry of a material is dramatically restricted when any two of all four primary ferroic properties (ferroelectricity, ferromagnetism, ferroelasticity, and ferrotoroidicity) coexist. A ME multiferroic material should possess coexisting electric and magnetic orderings [34-35]. However, symmetry consideration requires the absence of space-inversion and time-reversal symmetry for the ferroelectricity and magnetism, respectively to

occur in the same phase [36]. The schematic illustration of spatial-inversion and time-reversal symmetry in ferromagnets, ferroelectric and multiferroics, is shown in Fig. 1.4.

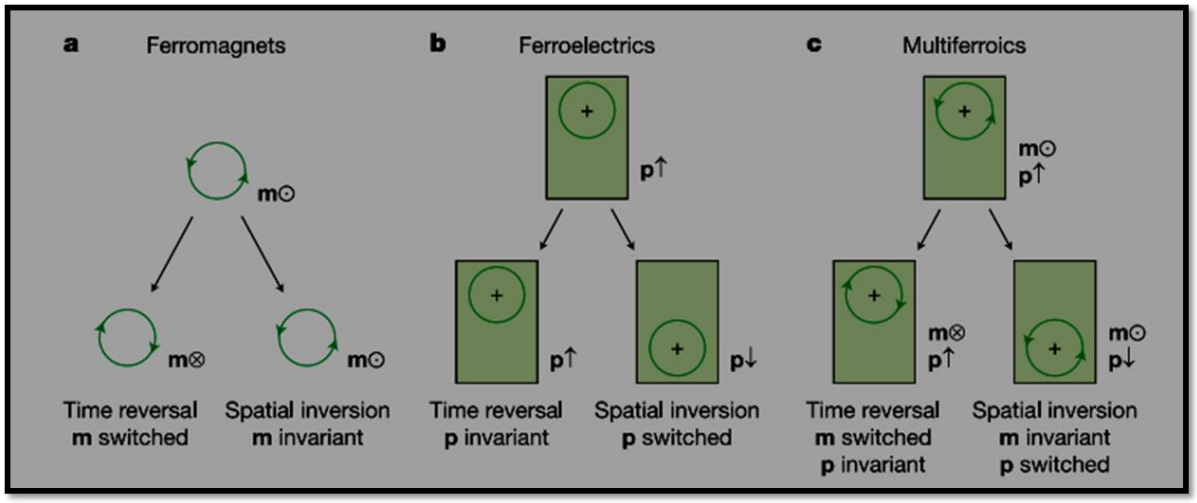


Fig. 1.4 Schematic of spatial-inversion and time-reversal symmetry in ferromagnets, ferroelectrics and multiferroics [25]

The influence of spatial-inversion as well as time-reversal symmetry on the ferroics is discussed below [25].

**a) Ferromagnets**

These possess magnetic moment m (denoted by arrowhead representing a revolving charge, Fig. 1.4 (a)). The time reversal results in switching of the orbit however, no change occurs on spatial inversion.

**b) Ferroelectrics**

These possess dipole moment p (denoted by positive point charge, which is asymmetric in a crystallographic unit cell with no net charge, Fig. 1.4 (b)). The time reversal results in change however, spatial inversion reverses dipole moment.

### c) Multiferroics

These possess both magnetic and electric ordering and do not possess either symmetry (Fig. 1.4 (c)).

Ferroelectricity requires structural distortion of the high-symmetry phase to deteriorate the center of symmetry for the occurrence of electric polarization. There exist 31 point groups, which allow spontaneous electric polarization, and 31, which allow spontaneous magnetization. The 13 point groups, 1, 2, 2′,m,m′,3,3m′,4,4m′m′,m′m2′,m′m′2′,6, and 6m′m′, in both sets are observed to exhibit both ferroic properties in the same phase [23-24]. This demonstrates substantially reduced possible crystal structures out of total 122 Shubnikov point groups. Although, this number being not very large, yet many materials that are not even ferroelectric and ferromagnetic subsist in one of the 13 allowed symmetries. Thus, possibly symmetry considerations are not accountable for the scarcity of multiferroics [6].

#### 1.2.4.2 Chemistry

In order to find its possible reason, N. A. Hill studied the chemistry of these materials using first principle of density functional theory calculations [6]. The chemistry issue involved is briefly given below.

Multiferroism is a mutually exclusive phenomenon, owing to the contrary prerequisites of ferroelectricity and ferromagnetism, thereby making these materials rare [37]. This problem is also addressed as "$d^0$ vs $d^n$ problem" [6]. Ferroelectric materials possess empty 3d electron configuration ($d^0$) and no d electrons implies no magnetic ordering (i.e. either ferro-, ferri-, or antiferromagnetic). When d orbital is partially occupied ($d^n$, where n is the number of electrons), the possibility of distortion, which destroys center of symmetry, is abolished.

### 1.2.5 Necessity of Multiferroics

The need of the hour demands one such material, which is simultaneously non-volatile, robust, fast, less energy consuming and miniature in size. The vast applications offered by electric and magnetic materials stems the desire to chase a new generation of memories, sensors, transducers, actuators that are powered by materials combining the properties of both electric and magnetic materials. Although the existing ferroelectric based random access memories (FeRAMs) are energy efficient and have fast writing speeds due to switching of polarization yet they have size limitations and slow readability owing to its destructive read operation and subsequent reset. Even in case of magnetoresistance random access memories (MRAMs), the material being a hard ferromagnet, possessing high coercivity necessitates larger magnetic field application for switching the magnetic states, and thus consumes large amount of energy [38]. This necessitates the need of a memory device possessing the best features of both MRAMs and FeRAMs (ferroelectric write and magnetic read operations and vice versa). This leads to effective enhancement of the writing speed, reduction of energy consumption and obviously device miniaturization. From this standpoint, multiferroic materials possessing coupled electric and magnetic orders offer new possibilities towards enhancement of data density and fabrication of an “ultimate memory device”. Thus, coupling between the electric and magnetic orders is of immense significance [39-42].

## 1.3 Magnetoelectric effect

The magnetoelectric (ME) effect delineates the coupling between electric and magnetic orders in matter [43-47]. It implies that magnetization can be induced by the application of an electric field and vice versa. This functionality enables an extra degree of freedom and could give rise to novel phenomena such as effect of ferroelectricity on spin transport, electrical tuning of magnetocrystalline anisotropy and exchange bias, etc [43-44].

The electric and magnetic order coupling opens up unexplored avenues for device formation. It may tremendously impact the areas of spintronics, data storage, actuators and transducers, where the electric field control of magnetic spins consumes remarkably low power as compared to magnetic control that needs electric currents to generate the magnetic field [3, 6].

It is an independent phenomenon, which occurs in any material having magnetic and electric orders irrespective of the fact that it's multiferroic or not [43]. The ME coupling can be better understood by expanding the free energy of a material given below [33, 45].

$$F(E,H) = F_0 - P_i^S E_i - M_i^S H_i - \frac{1}{2}\varepsilon_0 \varepsilon_{ij} E_i E_j - \frac{1}{2}\mu_0 \mu_{ij} H_i H_j$$
$$- \alpha_{ij} E_i H_j - \frac{1}{2}\beta_{ijk} E_i H_j H_k - \frac{1}{2}\gamma_{ijk} H_i E_j E_k - \ldots\ldots \quad (1.1)$$

where H and E denote the magnetic and electric field, respectively. The differentiation of the free energy term, as given under, leads, respectively, to the electric and magnetic order parameters.

$$P_i(E,H) = -\frac{\partial F}{\partial E_i} = P_i^S + \varepsilon_0 \varepsilon_{ij} E_j + \alpha_{ij} H_j + \frac{\beta_{ijk}}{2} H_j H_k + \gamma_{ijk} H_i E_j + \ldots \quad (1.2)$$

$$M_i(E,H) = -\frac{\partial F}{\partial H_i} = M_i^S + \mu_0 \mu_{ij} H_j + \alpha_{ij} E_i + \beta_{ijk} E_i H_j + \frac{\gamma_{ijk}}{2} E_j E_k + \ldots\ldots \quad (1.3)$$

where $\varepsilon$ and $\mu$ are, respectively, the electric and magnetic susceptibilities, $\alpha$ is known as the linear ME effect and represents polarization induced by a magnetic field or vice versa. $\beta$ and $\gamma$ denote the higher order ME effect and are smaller in magnitude than the lower order terms.

## 1.4 Types of Multiferroics

On the basis of the experimental studies multiferroics can be characterized into two classes: Type-I and type-II multiferroics. Type-I ferroics have independent ferroelectric and magnetic properties arising from different sources, whereas in the type-II multiferroics magnetism results in ferroelectricity. This class exhibits strong ME coupling although the polarization values are not much high. The details are given below [5].

### I. Type-I multiferroics

These are good ferroelectrics and possess ferroelectric as well as magnetic ordering well above the room temperature. However, ME coupling in these materials is weak. They have been further categorized in four subclasses on the basis of their primary mechanism of ferroelectricity.

#### a) Multiferroic perovskite

Among perovskites there are many magnetic and ferroelectric materials. However, these being mutually exclusive phenomena due to above mentioned "$d^0$ vs $d^n$ problem". The solution to this problem are the mixed perovskites having both $d^0$ and $d^n$ ions (Fig. 1.5 (a)).

**b) Ferroelectrics with lone pairs**

Multiferroics like $BiFeO_3$ and $PbVO_3$ with the lone pairs of $Bi^{3+}$ and $Pb^{2+}$ ions result in ferroelectricity. These lone pairs of 6s orbital are non bonding in nature. Their ordering in one direction causes the ferroelectricity in these materials. Fig. 1.5 (b) illustrates orientation of $6s^2$ electron lone pair (yellow lobes) of $Bi^{3+}$, which results in electric polarization (green arrow) in $BiFeO_3$.

**c) Ferroelectrics with charge ordering**

Another mechanism that results in ferroelectricity in type-I multiferroics is charge ordering. This mechanism occurs in multiferroics comprising of transition metal ions having different valence state.

The ferroelectricity is essentially observed in these systems when there is coexistence of inequivalent sites, together with different charges, as well as inequivalent bonds. The mechanism is illustrated in Fig. 1.5 (c). Examples of the charge ordering system are $Pr_{1/2}Ca_{1/2}MnO_3$ or nickelates $RNiO_3$. However, there exist some of multiferroics where only one of the conditions, either inequivalent sites or inequivalent bonds, leads to ferroelectricity. $Ca_3CoMnO_6$ is a multiferroic where ferroelectricity originates due to ions with unequal charge and $LuFe_2O_4$ represents the example of ferroelectricity due to inequivalent bonds.

**d) "Geometric" ferroelectricity**

In this subclass, the structural instability is the origin of ferroelectricity. Geometerical assumptions like size effects give rise to this phenomenon. Multiferroics like $YMnO_3$ fall in this category. Fig. 1.5 (d) illustrates the mechanism of electric polarization in $YMnO_3$. In it, the tilting of the $MnO_5$ unit in $YMnO_3$ results in ferroelectricity. The tilting decreases the

distance between oxygen and Y ions and generates dipole moments aligned more particularly in one direction as compared to other directions. Consequently, ferroelectricity appears.

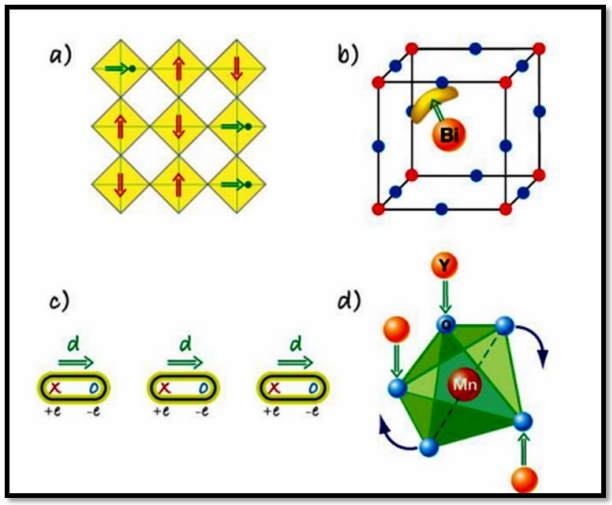


Fig. 1.5 Various subclasses of type-I multiferroics. Schematic showing (a) a mixed perovskite (where green circles represent $d^0$ ions whose shifting from the center of oxygen octahedra leads to ferroelectricity, and red arrows represent magnetic orders corresponding to $d^n$ ions, (b) electric polarization (green arrow) in $BiFeO_3$ by the orientation of $6s^2$ electron lone pair of $Bi^{3+}$ ion (yellow lobes) (c) a charge ordered system generating ferroelectricity from the coexisting inequivalent sites having different charge as well as inequivalent bonds and (d) tilting of $MnO_5$ unit in $YMnO_3$ that leads to ferroelectricity [5]

## II. Type-II multiferroics - Magnetic multiferroics

This class constitutes the novel multiferroics where a specific magnetism results in ferroelectricity. Strong ME coupling is exhibited by type-II multiferroics and therefore are quite attractive. These can be further categorised into two subclasses on the basis of the mechanism of magnetic behaviour as given below.

### a) Spiral type-II multiferroics

Here the ferroelectricity is induced by a spiral magnetic ordering. Multiferroic $TbMnO_3$ is one famous example that falls under this category. The magnetic ordering appears at $T_{N1}$ = 41 K, however, it being sinusoidal, results in no net magnetization (Fig. 1.6 (a)), and, thus ferroelectricity. The magnetic ordering changes at $T_{N2}$ = 28 K, thereby leading to ferroelectricity (Fig. 1.6 (b)). The polarization is created when Mn spins move cycloidally and the dipoles rotate in a plane having wave vector, as shown in Fig. 1.6 (b). However, if the rotation takes place around the axis parallel to wave vector, no polarization occurs [Fig. 1.6 (c)]. This observation cannot be generalized over other symmetries. The polarization in some cases may happen by special movements of cycloidal. The spiral multiferroics are highly influenced by the magnetic fields, which in turn affect the electric polarization.

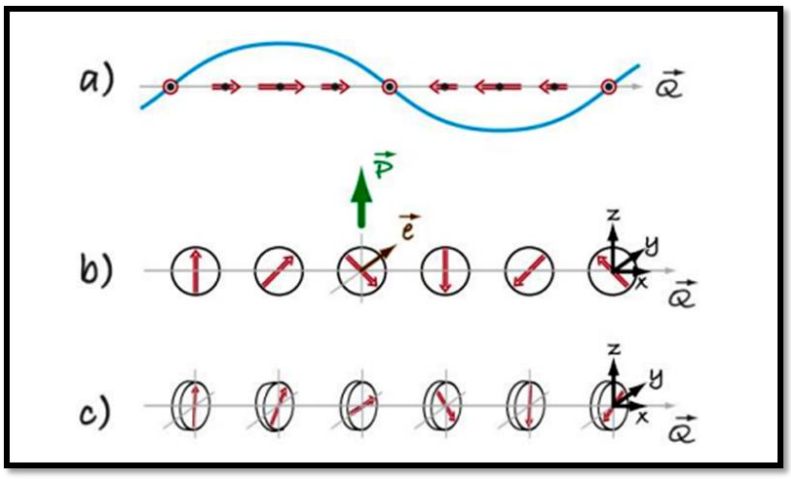


Fig. 1.6 Schematics illustrating several spiral magnetic structures in type-II multiferroics. (a) Magnetic moments of different magnitude are aligned in a particular direction in every half period of sinusoidal spin density wave. The centrosymmetry eliminates ferroelectricity. (b) Spins rotate cycloidally in the plane of wave vector $Q = Q_x$. The polarization appears here. (c) Spins rotate cycloidally in the plane oriented perpendicular to the wave vector. No polarization appears in most cases [5]

### b) Collinear type-II multiferroics

This category involves the multiferroics where electric polarization is derived in structures having collinear magnetic moments. Collinear magnets are structures having magnetic moments aligned parallel to a special axis. Here, spin-orbit interaction is not required to have ferroelectricity, while it's caused by exchange striction. Multiferroic $Ca_3CoMnO_6$ presents one such example. The exchange striction is caused by transition metal ions having different valences i.e. $Mn^{4+}$ and $Co^{2+}$. These are placed at alternate positions in a chain. Moreover, the materials with identical magnetic ions may exhibit this phenomenon as in transition metal oxides exchange happens usually through intermediate oxygen ions.

In summary, type-I multiferroics are older and possess magnetic and electric transition temperatures well above the room temperatures [6]. However, the coupling in magnetic and electric orders is very weak. In type-II multiferroics, the ME coupling is strong but the ordering temperatures are extremely below the room temperature. Thus, efforts are made in the direction of enhancing the ME coupling in type-I multiferroics so as to have their practical applications. Among the entire identified single phase ME multiferroics, $BiFeO_3$ is one of the few candidates that exhibits room temperature ferroic ordering [48]. Hence, it is fascinating from technological standpoint and accordingly, it has received considerable attention by the research community.

## 1.5 Bismuth Ferrite ($BiFeO_3$)

The most promising single phase ME material known till date is '$BiFeO_3$' - a perovskite belonging to type–I category of multiferroics. It has set up a global benchmark, and the research interest in $BiFeO_3$ derives from its well above room temperature ferroelectric (Curie temperature ($T_C$) ~ 1103 K) and G-type antiferromagnetic (Néel

temperature ($T_N$) ~ 643 K) orders [23]. This feature makes it unique and intriguing for research [48]. It is an incommensurate antiferromagnet and commensurate ferroelectric [25]. No other single phase multiferroic material has gained the attention of the same level as $BiFeO_3$. On looking back at the history, it has been found that in the late 1950s the perovskite $BiFeO_3$ was first produced focusing its important feature - the ME coupling [25]. Smolenskii [49] in 1960 started the initial research on $BiFeO_3$ and, was unsuccessful to synthesize single phase $BiFeO_3$. The successful preparation of single phase $BiFeO_3$ was done by Achenbach in 1967 by eliminating secondary phases by using nitric acid (leaching) [50]. Its structural and physical properties were under controversies during the 1960s and 1970s. Until 1960 it was considered to be an antiferromagnetic and ferroelectric multiferroic [51]. However, its ferroelectric nature was doubted to be an antiferroelectric, and, due to its high Curie temperature, it was expected to possess high spontaneous polarization, similar to other ferroelectrics [32]. In 1970, spontaneous polarization value of ~ $6.1 \mu C cm^{-2}$ along [111] was observed from the ferroelectric measurements done at 77 K, which corroborated well with the rhombohedral phase ($R_{3c}$; polar space group) determined using x-ray diffraction (XRD) [52]. These observations were confirmed by the detailed structural analysis of ferroelectric/elastic monodomain of single crystalline $BiFeO_3$ later in 1980s [43]. Finally, the polar nature of $BiFeO_3$ was confirmed by the chemical etching experiments performed on ferroelastic single domains of $BiFeO_3$ and set aside the questions of it being antiferroelectric. It proved the thermodynamic stability of ferroelectric/elastic phase of $BiFeO_3$ ranging from 4 to 1103 K [43]. In 2003, an enormous remnant polarization (50-60 $\mu C/cm^2$) value was reported by Ramesh's group in thin films of $BiFeO_3$ [53]. Later larger polarization values (100 $\mu C/cm^2$) were obtained in single crystals [54]. These studies revealed defects to be the major cause for high leakage currents that resulted in poor polarization and dielectric constant ($\varepsilon$ ) values.

Thus, an increase in interest in $BiFeO_3$ began owing to the advances in the fabrication, characterization and computational systems for modelling the multiferroics [3].

### 1.5.1 Crystal Structure

$BiFeO_3$ crystallizes in rhombohedrally-distorted perovskite structure that belongs to the space group $R_{3c}$ [55].

The crystal structure of $BiFeO_3$ can be characterized by two distorted perovskite units attached along the body diagonal (or pseudocubic axis [111]). The schematic showing crystal structure of $BiFeO_3$ is presented in Fig. 1.7. The two oxygen octahedra connected along [111] rotate clockwise and anticlockwise around [111] by ±13.8º and the Fe-ion shift by 0.135 Å along it away from the center position in oxygen octahedron [45].

The ground-state of the crystal structure is attained from the ideal cubic perovskite ($Pm\bar{3}m$) by implying two symmetry lattice modes [56]: (i) a nonpolar R-point mode that rotates the successive oxygen octahedral opposite to each other around [111] and (ii) a polar $\Gamma_4^-$ distortion, comprising of polar displacements around [111] along with symmetric breathing of adjoining oxygen octahedras. The rhombohedral lattice constant was determined as 5.63 Å and the rhombohedral angle being $\alpha$ = 59.35°, - almost equal to the ideal value, i.e., 60° value [32, 57].

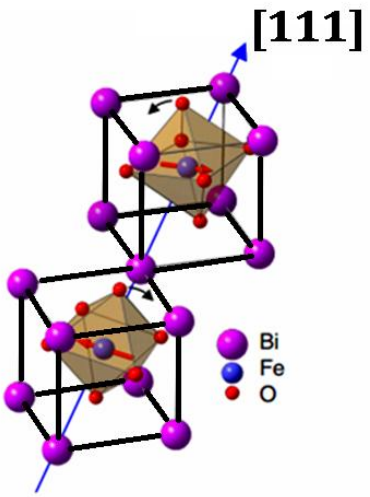


Fig. 1.7 Schematic illustrating the crystal structure of $BiFeO_3$ [56]

The crystal structure of $BiFeO_3$ (Fig. 1.7) has two perovskite unit cells with successive oxygen octahedra rotating opposite to each other along [111]. Red arrows at Fe atoms denote orientations of magnetic moments in (111) plane [56].

This structure results in two important considerations, namely ferroelectric polarization and magnetization.

### 1.5.2 Ferroelectric state in $BiFeO_3$

The ferroelectric state of $BiFeO_3$ is realized by the large displacement of the $6s^2$ lone pair of Bi ions with respect to $FeO_6$ octahedra [43, 58]. The ferroelectric polarization along the [111] direction by the displacement of the $Bi^{3+}$ ions (shown by arrow in Fig. 1.8 (a)) forms the eight polarization variants $P_i^{\pm}$ $i=1,4$ (polarization vectors having negative and positive orientations along four cube diagonals), analogous to four structural variants [59-60]. The central unit denotes the perovskite building block of rhombohedral structure (Fig. 1.8(a)).

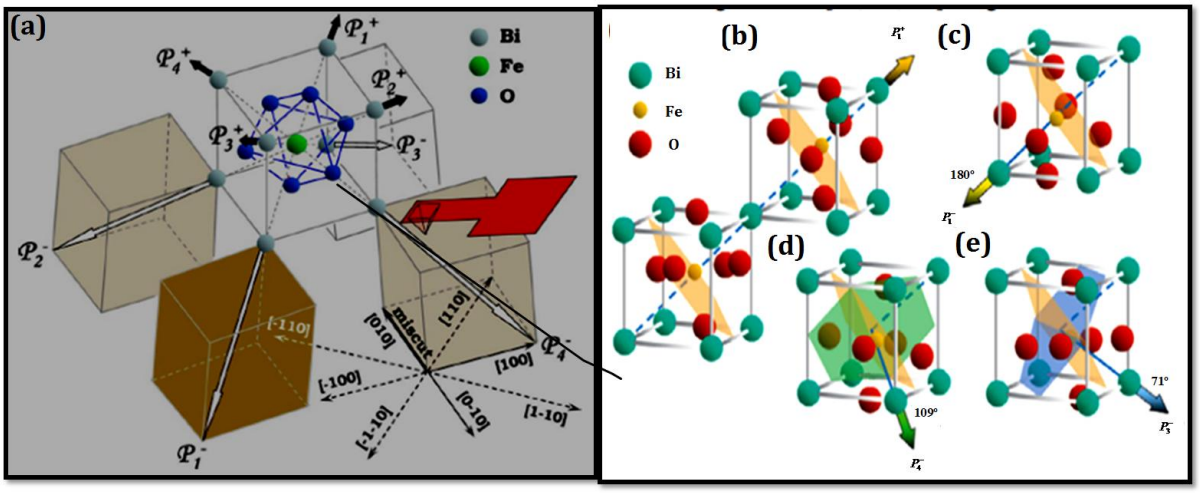


Fig. 1.8 Schematic illustration of (a) four different structural variants [60], polarization (b) before electrical poling with "up" out of plane component, (c) 180º, (d) 109º, and (e) 71º switching mechanisms [61]

Fig. 1.8 (b-e) shows the bold arrows and shaded plane representing ferroelectric polarization and antiferromagnetic planes, respectively in (001)-oriented $BiFeO_3$ crystal structure. It reveals that the switching direction of polarization in $BiFeO_3$ can be 180˚, 109˚, and 71˚ [61-62]. The schematic illustrating the polarization in the above said directions is shown in Fig. 4.

### 1.5.3 Magnetic state in $BiFeO_3$

$BiFeO_3$ is a G-type antiferromagnet (as shown in Fig. 1.9 (a)) having Néel temperature $T_N$ = 643 K [32]. Its antiferromagnetic structure is quite complex - a combination of spin, charge, and lattice degrees of freedom in the multiferroics [63]. The magnetic nature of $BiFeO_3$ was studied in detail during the 1980s [59]. However, Sosnowska in 1982 reported that $BiFeO_3$ is a G-type antiferromagnet [64].

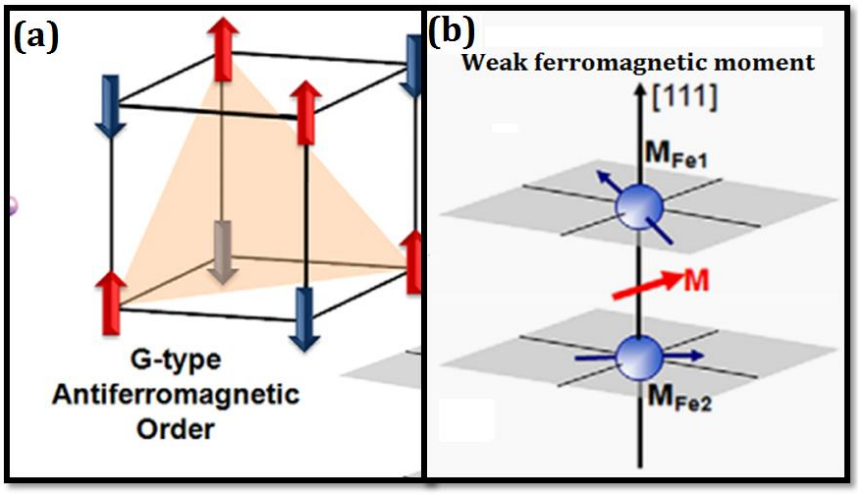


Fig. 1.9 Schematic showing (a) the magnetic structure of $BiFeO_3$ having G-type antiferromagnetic ordering and (b) formation of weak ferromagnetic moment [43]

This implies ferromagnetic coupling of Fe magnetic moments in (111) planes and antiferromagnetic, between the adjacent planes. The symmetry allows canting of the antiferromagnetic sublattices that leads to weak ferromagnetism (of the Dzyaloshinskii–Moriya type) if the orientation of the magnetic moments is perpendicular to the [111] direction, as shown in Fig. 1.9 (b) [65].

However, neutron diffraction studies [66] have revealed incommensurate spin spiral structure (shown in Fig. 1.10) of wavelength of 62 nm superimposed on the antiferromagnetic ordering [65]. This spin spiral structure, leads to cancelation of the overall magnetization and hence, hampers the occurrence of linear ME effect. A quadratic ME effect has been measured in the presence of this spiral spin structure, which, if destroyed, leads to visualization of linear ME effect [27]. This can be achieved by many ways, for example application of high magnetic field (20 T), doping etc.

The reason for small magnetization and a linear ME coupling i.e. spiral spin structure was found by time-of-flight neutron measurements in 1980s [55]. Moreover, the position of

satellite peak observed in these measurements along the $[110]_{hex}$ resulted in the determination of the wavelength of the spiral spin structure to be 62 nm and, also, it is incommensurate with the crystallographic lattice parameters.

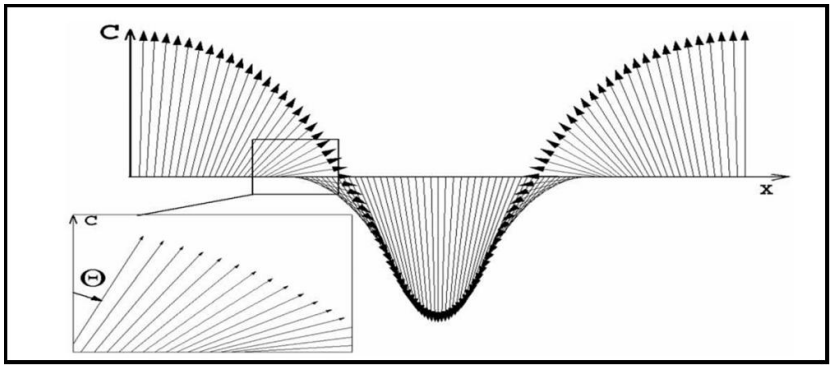


Fig. 1.10 Schematic illustrating the long range spiral spin structure. Arrows represent the antiferromagnetic vector [55]

### 1.5.4 Drawbacks of $BiFeO_3$

The research interest in $BiFeO_3$ derives from its well above room temperature ferroelectric and antiferromagnetic orders [67-70]. Also, as discussed above it possesses rhombohedral crystal structure having space group $R_{3c}$, which allows weak ferromagnetism and linear ME coupling [65]. While these being promising features from application point of view, it has a few inherent problems that restrict its device application; these are listed below.

**a)** Bulk $BiFeO_3$ possesses weak magnetism due to orientation of magnetic moments perpendicular to the rhombohedral axis, magnetic moment canting and spiral spin structure having wavelength of 62 nm. The spin spiral structure superimposed over the G-type antiferromagnetic order prevents the net magnetization [65].

**b)** The high leakage current, which is usually due to the secondary phases associated with the kinetics of its formation, nonstochiometery issues, defects, reduction of $Fe^{3+}$

to $Fe^{2+}$ (i.e. change of oxidation state) thereby giving rise to oxygen vacancies [71]. These lead to low resistivity, which in turn makes the complete polarization impossible.

**c)** It possesses low ME coupling coefficient values [65].

**d)** It possesses wider difference between the electric and magnetic transition temperatures [72].

The above issues altogether contribute towards the disappointingly low values of polarization and magnetization when compared to the standard ferromagnetic and ferroelectric materials. These parameters when taken care of enable its use in device applications.

To overcome the above mentioned issues, a number of studies abound in literature. The literature has been reviewed in detail described in the following section.

### 1.6 Literature review

It all began with the accidental discovery by Oersted in 1820 of magnetic needle fluctuation in the vicinity of an electric battery, as discussed in the beginning [1]. The prediction of ME dates back to 1894 by Pierre Curie. It stated that symmetry conditions allow polarization of an asymmetric crystalline body under the magnetic field [73]. Despite Curie's prediction highlighted the symmetry - a key parameter for the observation of ME effect, it took several decades to observe this effect until pioneering work by Landau and Lifshitz revealed that ME response requires time-asymmetric media [74]. On the basis of crystal symmetry considerations, in 1959, Dzyaloshinskii [5] theoretically predicted this effect in $Cr_2O_3$ followed by its experimental confirmation by Asrov in 1960 [47]. Schimd, in 1966, for the first time, reported experimental observation of the ME effect on the ferromagnetic

ferroelectric material ‘nickel iodine boracites ($Ni_3B_7O_{13}I$) [6]. This material known to be “Rochelle salt” of magnetic ferroelectrics is of high significance for proving the concept; however, it fails to find applications as well as the understanding of this vast field. Suchetelene in 1972, developed first magnetic field sensor in the Philips Laboratories based on ME effect. The sensitive material used was $CoFeO_4$-$BaTiO_3$ composite [75]. This discovery led to the synthesis of several other ferromagnetic ferroelectrics compounds in 1960s and 1970s, primarily by the two Russian groups - Smolenskii and Venevtsev [6]. However, the ME coupling, being weak in most of the materials, hampered their applications and, thus, the research in this area stagnated for almost two decades. However, the revival of interest in the field of ME materials was commenced by the theoretical investigations done by N. A Hill in 2000, employing density functional theory [28]. The theory successfully addressed the fundamental question: Why very few multiferroic materials are present in nature or hard to synthesize in laboratory. It, also, explained the unusual phenomena occurring in existing multiferroics along with predictions of the new ones. This opened up new possibilities for developing new materials with strong ME effect. In the past few years efforts have been made to synthesize new multiferroic materials, such as perovskites $ABO_3$ (A = Bi, Gd, Tb, Dy, Ho, Y, Na etc., B= Fe, Mn, Co, Sc, V, Ti, Nb etc), hexagonal manganites ($RMnO_3$, R = Y, Sc, Ho, Er, In, Dy, Tb, Gd etc.), cuprates, and other compounds ($BaMnF_4$, $CuB_2O_4$, $Ni_3V_2O_8$, spinel $CoCr_2O_4$, delafossite $CuFeO_2$, hexagonal ferrite $(Ba,Sr)_2Zn_2Fe_{12}O_{22}$ and $MnWO_4$ [31, 34-35, 5]. However, due to very small ME coupling in the multiferroic materials [34, 76-77], and, in case the coupling is large, it is attainable at temperatures far below room temperature [78]; Collectively, it hampered their implementation in technological applications.

Among these, $BiFeO_3$ is amongst the few known single-phase ME material exhibiting room temperature magnetic and electric ordering that makes it a centre of attraction for the researchers worldwide [42, 76-77].

A tremendous amount of research has been progressing on $BiFeO_3$ since the year of its production (1950) [60]; this is precisely due to its unique room temperature multiferroism – an important feature required for technological applications. However, its inherent problems (discussed in section 1.7.4) hamper its device application. Thus, globally research is carried on to overcome the issues associated with $BiFeO_3$. The attempts have been made by doping various ions. A lot of reports are available on doping at A (rare earth [79-88], alkaline earth [89-99]) and at B (transition metals [100-105]) sites in $BiFeO_3$ at bulk scale. However, very low values of magnetization and electrical behaviour were witnessed that were poor from technological standpoint. Thus, further attempts continued to overcome its drawbacks.

It has been observed that with the succeeding years, the field of nanotechnology began to invade the various research areas and the work on $BiFeO_3$ at nanoscale began. A lot of reports are available on the synthesis and investigation of various multiferroic properties of $BiFeO_3$ nanoparticles [106-123]. Moreover, it was observed that particle size plays a crucial role in deciding the multiferroic properties of nanoscale $BiFeO_3$ and, consequently, a lot of studies investigating influence of particle size on various aspects of $BiFeO_3$ were reported [106-122]. Park et al. reported strong dependence of magnetism of single crystalline $BiFeO_3$ nanoparticles [110]. The nanoparticles were synthesized by a popular technique – sol-gel [124-128]. Increasing magnetism with decreasing particle size is correlated to increasing suppression of its spin cycloid and uncompensated spins on particle size. Mazumder et al. studied particle size dependence of magnetization and phase transition at Néel temperature [106]. High saturation magnetization ($0.4\mu_B$/Fe) along with calorimetric and dielectric

anomalies at magnetic transition points, which indicate strong coupling of electric and magnetic order parameters in nanoscale $BiFeO_3$ nanoparticles (4-40 nm) [107] were reported. The influence of particle size on lattice parameters and polar displacement of atoms was reported by Selbach et al. [108]. It has been shown by rietveld refinement that rhombohedral distortion, reduced with decreasing particle size, is accompanied with decaying polarization. Significantly high photocatalytic activity in nanoscale $BiFeO_3$, as compared to bulk, is owed to high surface to volume ratio of nanoparticles [109].

It was observed that reducing the size to nano-regime was of immense advantage. It leads to partial destruction of spin spiral structure for the particles having size below its period (i.e. 62 nm) that releases magnetism and results in net magnetization [110]. Also, since the synthesis method of $BiFeO_3$ at nanoscale involves low temperatures that prevent the volatilization of Bi. Consequently, it leads to the reduction of the secondary phase formations, defects, oxygen vacancies and non-stoichiometric related issues thereby enhancing the resistivity [110]. Thus, reduction of size to nano scale has proven to be quite efficient in enhancement of its multiferroism. These studies unveils crucial role of particle size.

Since, it has been revealed that reducing the size surmount the issues by destroying the incommensurate spin spiral structure and reduction of impurities and doping at A- and B-sites in $BiFeO_3$ lead to the enhancement of its multiferroic properties. Thus, it was observed that studies began to be conducted on A - (rare earth [129-136], alkaline earth [137-144]) and B - (transition metal [145-147]) sites of $BiFeO_3$ nanoparticles. It has been revealed that doping of rare earth and alkaline earth metal ions at A-site are of much significance compared to others. Also, A-site substitution is the most popularly employed method for the enhancement of magnetic and electric properties of $BiFeO_3$ [129-143]. It results in lattice

structure variation, suppression of spin spiral structure, and reduction in the non-stoichiometric issues resulting in elimination of oxygen vacancies thereby improving the shortcomings of $BiFeO_3$ [148].

The mechanisms involved in the doping of rare earth and alkaline earth metal ions in $BiFeO_3$ that result in enhancement of multiferroism in $BiFeO_3$ are listed below.

**a)** Mostly rare earth metals (having non-filled f-orbitals and smaller ionic radii than Bi) are substituted as the smaller ionic radii cause large distortion of lattice, which thus suppresses the spin spiral structure and consequently unlocks the magnetism. Also, these result in high magnetization values due to their inherent high magnetic moment and coupling between magnetically active 4f electrons of rare earth ions with $Fe^{3+}$ ions as revealed by the first-principle calculations [132]. The electric properties are also enhanced as the smaller ionic radii induces more buckling in the Fe-O-Fe bond angle that accompanies smaller tolerance factor that results in more insulating character [48].

**b)** When alkaline earth ion (divalent) substitutes $Bi^{3+}$ (trivalent) ions charge imbalance is created in the system. Three possibilities exist to balance the charge [149]: (i) creation of oxygen vacancies, (ii) transformation of some of $Fe^{3+}$ into $Fe^{4+}$ and (iii) coexistence of two or more phases. It has been demonstrated that charge compensation takes place via the creation of oxygen vacancies and $Fe^{3+}$ preserves its oxidation state. These oxygen vacancies suppress the spin spiral structure of $BiFeO_3$ and thus unlock the magnetism. Also, the being less volatile than Bi reduces the secondary phases and other related issues that degrade the insulating behaviour of $BiFeO_3$ [150].

A lot of reports are available revealing that doping of rare earth (Tb, Dy, Gd) and alkaline earth (Ca, Sr, Ba) metals at A-site are of high advantage. A few are listed below.

Doping of $Tb^{3+}$ ions have produced several interesting results. For example, Nan et al. observed the influence of Tb-doping on the crystal structure of $BiFeO_3$ that largely enhances the magnetic and electric properties of $BiFeO_3$ [129]. It stabilizes the valence of $Fe^{3+}$ ions that reduces the leakage current. The effect of nano-size and Tb-doping on structural, magnetic and ME coupling revealed the structural transition from rhombohedral to orthorhombic phase [151]. The substitution driven structural transition resulted in ferromagnetism in the synthesized nanoparticles. The observed ME effect was explained on the basis of quantum confinement, magnetostriction effect, spin-exchange constriction and exchange interactions.

$Dy^{3+}$ ion- doping have been observed to enhance the multiferroism of $BiFeO_3$. Qian et al. addressed Dy-doped $BiFeO_3$ nanoparticles prepared by sol-gel method resulted in change from the rhombohedral to the orthorhombic structure that enhanced the magnetization as well as dielectric ordering in 2009 [130]. In the following year i.e. 2010, Qian et al. synthesized $BiFeO_3$ co-doped with $Dy^{3+}$ and $La^{3+}$ ions, which were indexed to the orthorhombic structure. It was found that that the small amount of substitution of smaller trivalent rare-earth ions at the place of $Bi^{3+}$ ion along with high magnetic moment in the nano-system is a way to improve the multiferroism of $BiFeO_3$ [152].

$Gd^{3+}$ ion having high magnetic moment ($8.0\mu_B$) is optimum candidate for enhancing the magnetism. Guo et al. scrutinized the effect of Gd dopant on the structural, photocatalytic activity, and ferromagnetic properties of $BiFeO_3$ nanoparticles [132]. The compositional-driven phase transition from rhombohedral to orthorhombic distorted spin cycloid that unlocked the magnetization and enhanced the photocatalytic activity. It also reduces the possibility of creation of oxygen vacancies due to the substitution of less volatile $Gd^{3+}$ ions at

Bi site thereby, improving the resistance of the system and thus ME coupling [130]. Hu et al. synthesized $Bi_{1-x}Gd_xFeO_3$ (x= 0, 0.1, 0.2, 0.3) nanoparticles by polyol-mediated method, which possessed improved ferroelectric and ferromagnetic behaviour with the increasing $Gd^{3+}$ ions concentration [134]. Temperature and field dependent magnetic measurements reveal the frustrated magnetic behavior of this system.

Ca-doping has been observed to act as a good proxy for chemical or hydrostatic pressure by Catalan et al., which may be used to bring the magnetic and ferroelectric temperatures close and thus enhancing ME coupling in $BiFeO_3$ [91]. It is reported that structural effects increase the magnetic transition temperature so that charge compensation mechanism occurs by formation of oxygen vacancies [91].

$Sr^{2+}$ ions of comparable ionic radius to that of $Bi^{3+}$ ions have produced several interesting results [137-138, 153]. For example, Bhushan et al. addressed how the dielectric constant decrease with increase in the ionic radius of alkaline earth metal ions (Ba, Sr, Ca) doped in nanoscale $BiFeO_3$ [137]. Wang et al. observed that magnetization enhanced in Sr-doped $BiFeO_3$ nanoparticles, as doping divalent - $Sr^{2+}$ at trivalent ($Bi^{3+}$) site creates charge imbalance and therefore suppresses spiral spin structure [138]. Mandal et al. formed tailorable morphologies ranging from spherical to pillar-like of Sr-doped $BiFeO_3$ nanoparticles by varying calcination temperature and found tunable magnetic and photoluminescence properties [153]. However, the influence of particle size of Sr-doped $BiFeO_3$ nanoparticles on magnetic as well as electric order has not been studied. The corresponding characterization of Sr-doped $BiFeO_3$ nanoparticles would give size-dependent trends under the influence of surface strains induced by confined particle size dimensions unlike strain induced from the substrate in thin films [110].

Doping of $Ba^{2+}$ ions having ionic radius larger than that of $Bi^{3+}$ ions have produced several interesting results. For example, Li et al. prepared $Bi_{1-x}Ba_xFeO_3$ (x=0, 0.01, 0.03, 0.05, and 0.1) nanoparticles by sol–gel process that exhibited strong absorption in visible light region and increased photocatalytic degradation under visible light with the increasing concentration of $Ba^{2+}$ ions [139]. Yang et al. prepared $Ca^{2+}$ and $Ba^{2+}$ ions co-doped $BiFeO_3$ nanoparticles, which exhibited structural transformation from the rhombohedral to orthorhombic and then to tetragonal with increasing dopant concentration [140]. The dielectric as well as magnetic properties of the nanoparticles were improved greatly. Also, the co-doped samples exhibited increased magnetic transition temperature.

It has been summarized that these dopants are a way to improve the shortcoming of $BiFeO_3$. Also, on reviewing the literature it has been demonstrated that particle size plays a crucial role in deciding the overall multiferroism in nanoscale $BiFeO_3$ system (as discussed previously). However, not much of the work has been done that explores the influence of particle size on the magnetic and electric properties of rare earth and alkaline earth metal ions-doped $BiFeO_3$ nanoparticles. Thus, being motivated from the mentioned gap work has been carried out in the said direction.

This thesis reports the particle size influence on structural, morphological, magnetic, dielectric and ferroelectric properties of rare earth (Tb, Dy, Gd) and alkaline earth (Ca, Sr, Ba) metal-doped $BiFeO_3$ nanoparticles prepared by sol-gel method. The particle size was tailored by varying the calcination temperature. Their structural, morphological, magnetic, dielectric and ferroelectric properties have been investigated.

# *Chapter 2*

# *SYNTHESIS METHOD*

# *AND*

# *CHARACTERIZATION TECHNIQUES*

# Chapter 2

Synthesis is the first step in the direction of realizing the various applications of multifunctional nanomaterials. It involves the optimization of experimental parameters so as to ensure the desired structure, phase purity, composition, size, shape etc. Characterizing the synthesized nanomaterials for the confirmation of the above parameters is the second necessary step. The present chapter provides brief description of the synthesis method and various characterization techniques employed for investigating the structural, morphological, magnetic, dielectric and ferroelectric properties of the rare earth and alkaline earth metal ions doped-$BiFeO_3$ nanoparticles.

## 2.1 Synthesis method

In the present work, sol-gel method has been used for the synthesis of undoped rare earth and alkaline metal doped-$BiFeO_3$ nanoparticles [152]. The particle size of synthesized nanoparticles has been tailored by varying the calcination temperature. Following section provides a brief description of the sol-gel method.

### 2.1.1 Sol-gel method

Sol stands for the dispersions of the colloidal particles (particles having dimensions ~ 1 - 100 nm) in a liquid while term gel denotes a rigid network having pores and polymeric chains [154]. It is an attractive as well as versatile technique employed for the synthesis. A wide range of products (thin films, fibers, wires, ceramic powders, nanoparticles, etc.) can be processed for metallic, organic, inorganic and hybrid materials [155]. It has many advantages over other techniques namely, readily available equipments, low temperature synthesis which offers well controlled compositions of materials and also, homogeneity at atomic level [18].

A typical sol-gel processing involves hydrolysis and condensation of precursors [18]. Precursors used are metal alkoxide or organic or inorganic salts while organic or aqueous solvents can be used as solvent for dissolving the precursors. A brief description of sol-gel method is given below [156].

**a)** Firstly, the ligands present in precursor attached to metal atom get replaced by hydroxyl groups and thereby, results in the formation of M-OH bonds (M denotes metal). The reaction is known as hydrolysis since hydroxyl ions get attached to metal atom.

**b)** Partially hydrolyzed molecules link together in the condensation reaction. Condensation releases small molecules (water or alcohol) and links hydrolyzed molecules together to form M-O-M bonds. This process continues to form larger molecules via process known as polymerization and when the dimensions of molecule extends throughout the solution then the gel is said to be formed. The remaining water or other solvent are then dried in order to obtain the final product. A schematic of the sol-gel method is shown in Fig. 2.1.

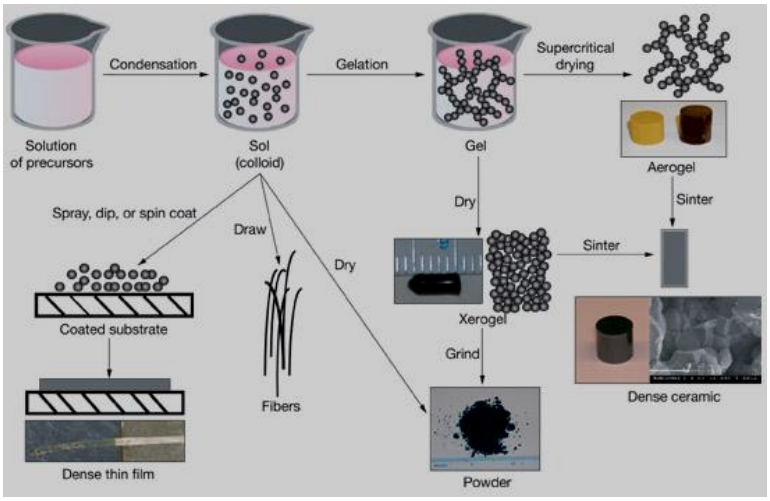


Fig. 2.1 Schematic of sol-gel processing of materials [157]

## 2.2 Characterization techniques

### 2.2.1 X-ray diffraction

#### 2.2.1.1 Introduction

X-ray diffraction (XRD) - the most basic instrument for a material scientist is a non-destructive technique widely employed for addressing issues related to crystalline structure of a material [18].

The energy of accidently discovered x-rays by W.C. Röntgen lies in the range of 3 and 8 keV [158]. After the evidences of wave properties and diffraction of x-rays from the periodic array of atoms in 1912 -13 by von Laue and his student, analytical applications of XRD started developing. The quantification and identification of crystalline compounds by powder diffraction pattern was finally suggested by Debye, Scherrer (1916) and Hull (1917) [158].

#### 2.2.1.2 Instrumentation and working principle

W.L. and W.H. Bragg in 1913 proposed formulation of x-ray diffraction [18]. The crystal is modelled as discrete set of parallel planes having a constant spacing (d). Electromagnetic radiations when incident on the periodic structure having geometrical variations equivalent to their wavelength, diffraction is observed [158] and in x-rays the interatomic distance amounts to 0.15 – 0.4 nm. When x-rays are incident at an angle θ on the regular array of atoms it reflects at the same angle and results in constructive and destructive interference. When the path difference is a whole number multiple of wavelength (i.e. constructive interference), this condition is known as Bragg's law $2d\sin\theta = n\lambda$ where n = 0, 1, 2... and $2d\sin\theta$ is the path difference between reflected rays. A schematic presenting Bragg law is shown in Fig. 2.2. Constructive interference results in enhanced intensity in certain

directions and its measurement helps in determining the crystalline structure of the materials. The intensities of the diffracted beams are dependent on the type of atoms and their arrangement in the unit cell [158]. Atoms with low atomic number scatter less than those having higher one. This difference is thus then reflected in the intensities of the diffracted beams and hence provides the information regarding the arrangement of the atoms in the crystal structure.

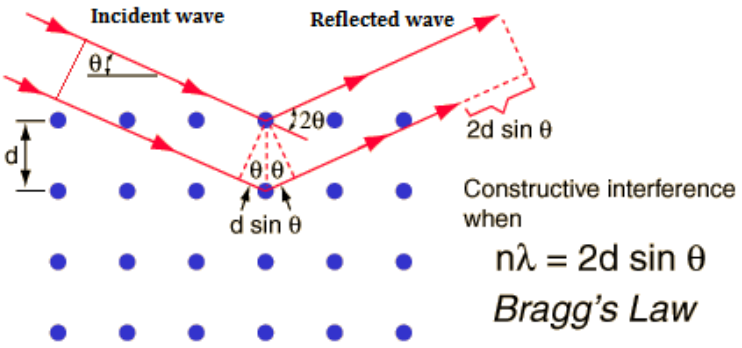


Fig. 2.2 Bragg's Law [159]

The components of a x-ray diffractometer (Fig. 2.3 (a)) consist of: x-ray tube, a goniomter, sample holder, and x-ray detector [160]. The schematic illustrating the various components is shown in Fig. 2.3 (a). X-rays are produced inside cathode ray tube which consists of two electrodes namely, an anode (metal target) at ground potential and a cathode, at highly negative potential. The cathode (tungsten filament) when heated emits electrons, which drifts towards the target under high potential. Electrons having sufficient energy remove inner shell electrons of the target material and results in characteristic x-ray spectra. The spectra so produced have various components: $K_\alpha$, $K_\beta$ and continuous spectrum. The undesired components are reduced relative to $K_\alpha$ by allowing their passage through filters (made of materials with atomic number one less than the target). Copper is the most commonly used target material in single-crystal diffraction, which produces $CuK_\alpha$ radiation

of wavelength 1.5418 Å. Finally, filtered x-rays are collimated and directed onto the sample. The geometry of the diffractometer is set in such a way that the rotation of the sample takes place at θ degrees in the path of the collimated x-ray beam. However, the diffracted beams are collected by the detector rotating at an angle of 2θ [161]. A schematic has been shown in Fig. 2.3 (a). The instrument taking care of the angle and rotation of the sample is known as goniometer. Whenever the Bragg equation is satisfied, constructive interference takes place and peak intensity increases. These varying peak intensities are recorded by a detector and the signals being processed are converted into count rate. This output is finally displayed on a computer.

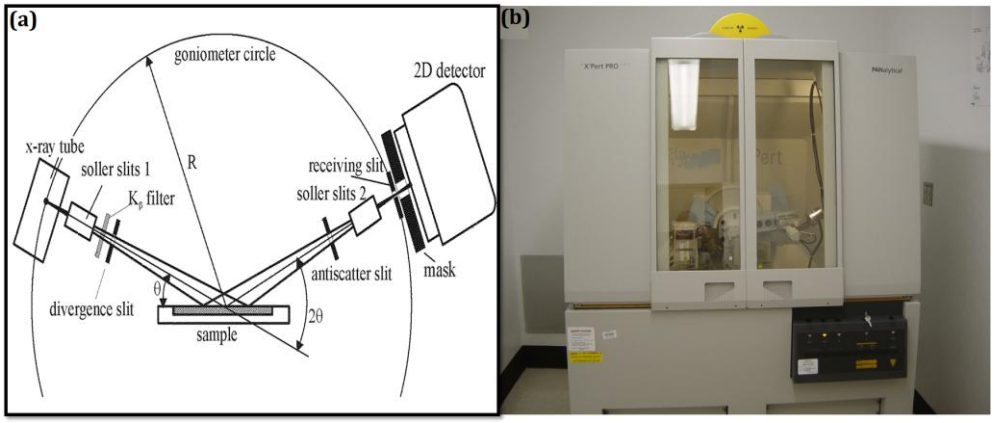


Fig. 2.3 (a) Schematic of goniometer [162] and (b) pictorial view of an x-ray diffractometer [163]

### 2.2.1.3 Sample preparation

Few gram of finely ground powder is required for the measurement. The powder when placed in the sample holder needs to be flattened ensuring that it is in level with the surface of sample holder; else the results will not be appropriate.

### 2.2.1.4 Information from XRD

The diffraction data obtained from XRD is quite informative and involves a wide set of applications. Their details are given below [164].

- Identification of the crystalline structure of solids. The obtained diffraction peaks are compared with the International Center Diffraction Data (ICDD) or formerly known as Joint Committee on Powder Diffraction Standards (JCPDS) data base. The corresponding best match is selected.
- Determination of the structural information involving space group, lattice constants, volume, strain, bond angles, bond lengths, crystallite size, orientation, preferred orientation in case of polycrystals, defects etc.
- Identification of the various phases present in the material and also, their amount.
- Determination of the purity of sample.
- A table summarizing various information that can be obtained from the different features of an XRD pattern is given as under:

Table 2.1 Set of information from various features of x-ray diffraction pattern

| | |
|---|---|
| **Peak positions** | Space group symmetry, crystal system, qualitative phase identification and unit cell dimensions |
| **Peak shapes & widths** | Defects, non uniform micro strain and crystallite size (2-200 nm) |
| **Peak intensities** | Point symmetry quantitative phase fractions and unit cell contents |

*In the present thesis, the X-ray patterns of the synthesized nanoparticles were recorded on x-ray diffraction (XRD, X'Pert PRO Panalytical MRD ML).*

### 2.2.2 Scanning electron microscope

Imaging is the most essential tool in nanotechnology and nanoscience. Scanning electron microscope (SEM) has unique capabilities for analysing surfaces.

#### 2.2.2.1 Introduction

SEM analogous to light microscope uses electron radiations, which results in magnification 2k X times the later [165]. High depth of field (ability to maintain focus) enables micrographs to possess three dimensional view of the surface to be examined by the unaided eye. It enables the investigation of specimens with a resolution down to the nanometer scale.

#### 2.2.2.2 Instrumentation and working principle

Its instrumentation and operation can be mainly divided into the following four parts [165]:

**a) Illuminating/Imaging system**

It consists of an electron gun and magnetic lenses which together form a collimated and coherent beam of electrons to be focused on the sample. Electron gun comprises of (i) filament; that generates electron and hence is negative with respect to ground, (ii) aperture shield; at a slight positive potential to that of filament and (iii) anode; held at very high positive potential relative to filament. Electrons are produced by passage of current through filament and it is heated till the voltage gradient

amongst filament and anode produces electrons. These electrons then get accelerated in the potential difference of anode and filament. Tungsten hairpin is the most regular electron source in use nowadays. The diameter of the electron beam exiting the gun needs to be narrowed for efficient image analysis as the smaller it is better is the resolution. This purpose is solved by a series of convergent magnetic lenses that demagnifies the beam to ~100 Å.

**b) Information system**

It comprises of (i) sample; that produces a variety of signals on interaction with the electron beam and (ii) series of detectors which identify and analyze the signals. The sample placed on a conductive substrate (aluminum stub or carbon planchet) is put inside the sample stage of SEM. The sample stage possesses electrical pathway to ground and control over the sample movement in X, Y and Z directions. Information regarding data signals originating from electron beam and atoms of sample interaction is important in order to control the sample movement. The data signals results from elastic (electron-nucleus) and inelastic (electron-electron) collisions of electron beam and atoms of the sample. Elastic collisions give rise to backscattered electrons which give topographical as well as compositional information of the sample. However, inelastic collisions deposit energy in the sample and return to its ground state by releasing energy in various forms such as secondary electrons, x-rays, photons and non-radiative transitions like phonons producing heat. A schematic presenting various data signals is shown in Fig. 2.4. All SEMs detect secondary and back scattered electrons (used for conventional imaging) by Everhart-Thornley electron detector. Its position is at 90° with respect to optical axis and is

aligned in the direction of sample so that more number of electrons enter the detector, which in turn improves image quality.

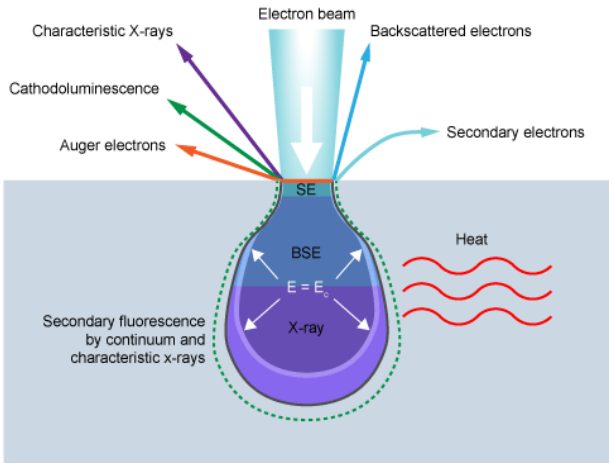


Fig. 2.4 Various data signals in a SEM [166]

**c) Display system**

The images thus, produced are displayed on the screen of cathode-ray tube (CRT) and the micrographs are recorded. Two CRTs are preferred as (i) the perseverance of light emission by fluorescent screen coating of the CRT after removing excitation, produces noise thereby, degrades the resolution of micrograph and (ii) fine-grained fluorescent coatings in the record CRTs give fine resolution relative to coarse grained visual CRTs. Nowadays SEMs have only one CRT incorporated with fine-grained, low halation phosphors, which eliminates above problems.

**d) Vacuum system**

The operation of optical column and specimen chamber of SEM is done under high vacuum ($\geq 10^{-4}$ torr) owing to many reasons: (i) presence of gas would result in scattering of the electron beam with its molecule, which would result in degradation

of image resolution due to chromatic aberration, (ii) low vaccum conditions accelerate the oxidation of tungsten filament, haphazard discharge along the optical axis and hence, contamination of the sample. Thus, SEM is employed with high vacuum system consisting of diffusion and turbo molecular pumps, which are backed up by low-vacuum rotatory pumps.

A schematic presenting working principle and pictorial of SEM view is shown in Fig. 2.5 (a) and (b), respectively.

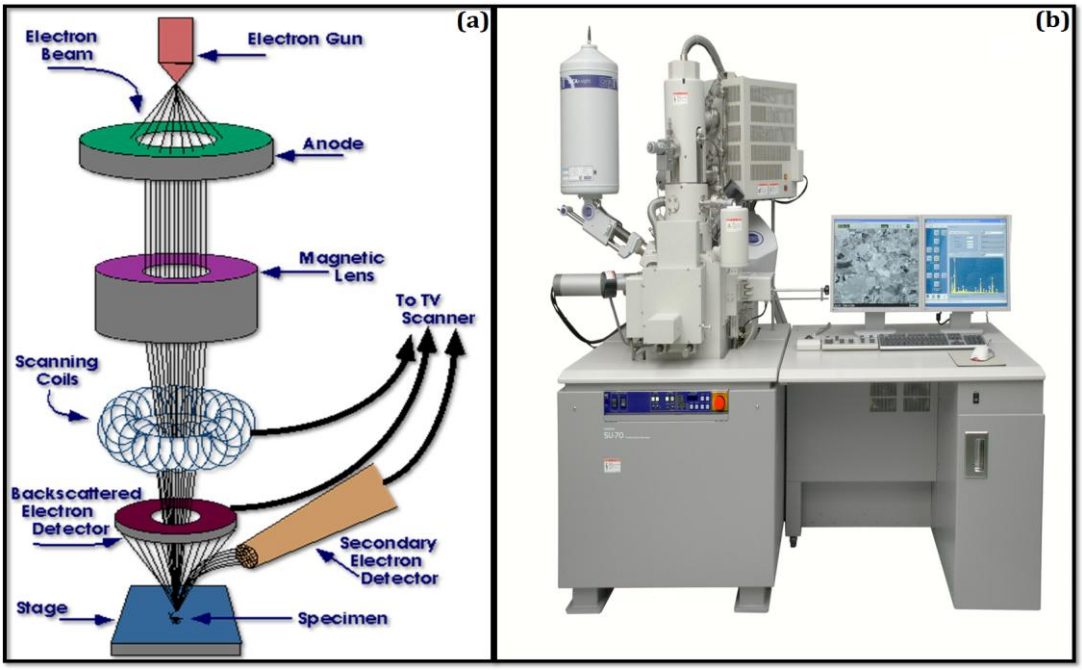


Fig. 2.5 Working principle [167] and pictorial view [168] of a SEM

### 2.2.2.3 Sample preparation

Firstly, during sample preparation, the size of the sample should be such that it fits into the specimen chamber and able to perform X, Y, Z, tilt and rotation translation of the stage freely. Secondly, cleanliness of the sample surface is necessary as presence of any unwanted material on the surface of the sample will hamper the image analysis. The contaminants such

as non conductive particles are shown as area of charging in SEM, which hides the sample surface. These not only create problem in analysis but also when exposed to vacuum vaporise and get deposited on the detector, apertures, etc. The sample can be ultrasonically cleaned by organic solvents followed by blast of compressed gas. It can also be gently brushed if the sample can't be solvent cleaned. After cleanliness the sample can be mounted on aluminium or carbon stub, which is placed inside specimen stage of SEM. Thirdly, non-conductive samples such as ceramics, glasses, plastics, etc. display charging artifacts and thus are examined at low voltages which result in limited resolution and magnification. These need to be coated with a conductive thin film so that it raises the density and conductivity of the sample, which previously absorbed the beam. The thin film remarkably enhances the magnification and resolution. Mostly, gold is employed as the coating.

In the present work powder was compacted for the microstructure analysis. The gold coating was done by sputtering technique and then the sample was placed on the aluminium stub with the help of double adhesive carbon tape.

### 2.2.2.4 Information from SEM

- The data signals generated from the electron beam and sample interaction reveals topography, morphology, chemical composition, crystalline structure and orientation [169].
- It's of immense use for analyzing the fractured surfaces [169-170].
- It is able to perform selected point analysis, which is used in qualitative determination of chemical compositions and also, their spatial variation [170-171].

*In the present thesis, micrographs of the synthesized nanoparticles were recorded on SEM: LEO 435VP and FEG SEM (field emission gun scanning electron microscope): JSM-7600F.*

### 2.2.3 Transmission electron microscope

#### 2.2.3.1 Introduction

Imaging, measuring, modelling, and manuplating matter is possible by transmission electron microscope (TEM) [172]. It is an important research tool, whose working principle is same as that of SEM except that the electron beam used for analysis is transmitted through the sample under investigation. Thus, this instrument provides compositional, topographical, morphological and crystalline information [173]. Ernst Ruska and Knoll in 1932 developed first TEM [174] and its goal was to achieve resolution higher than the optical microscope. The electron beam employed allows the probing of materials at atomic scale. The greatest advantage of using TEM is its ability to provide both image as well as diffraction information, simultaneously [18]. The electron when scattered by sample determines the kind of information obtained. Elastic scattering results in diffraction patterns and inelastic interactions at heterogeneities such as defects, grain boundaries, and dislocations lead to spatial varying intensity due to the complex absorption and scattering effects. TEM employs switching between the diffraction pattern and image viewing via controlling strength of the intermediate lens.

#### 2.2.3.2 Instrumentation and working principle

TEM consists of three basic systems (Fig. 2.6 (a)) namely, an electron gun and condenser system, image producing system, and image recording system [175]. The pictorial view of a TEM is shown in Fig. 2.6 (b). The detailed functioning of these systems is given as under:

### a) Electron gun and condenser system

The electron gun consists of an anode and cathode. The electron source (cathode), usually a tungsten filament or lanthanum hexaboride, emit electrons when heated. The filament is surrounded by control grid known as Wehnelt cylinder. Both the control grid and cathode are set at negative potential that equals the required accelerating voltage. Both of them are insulated from the instrument. The electrons on leaving the cathode, accelerate towards anode. The beam passes at a constant energy through the central aperture when the high voltage stabilizes. Now the intensity and angular aperture of the beam is controlled by the condenser lens system. Two lenses are required to converge the beam on the object. The first lens is used to form a reduced image, which is finally imaged by the second lens. The electron beam when impinges on the sample under investigation, it results in various interactions namely, coherent elastic scattered electrons, incoherent elastic forward scattered electrons, incoherent inelastic electrons, transmitted beam, backscattered electrons, secondary electrons, characteristic, auger electrons and continuum x-rays etc. These interactions are then detected by different detectors in order to view the images.

### b) Image producing system

The specimen stage is movable. The objective lens having short focal length of 1–5 mm is used that forms a real image, which is again magnified by projector lens/lenses. Modern instruments consist of two projector lenses for greater magnification. The various mechanical and electrical adjustments, i.e. alignment of various lenses with respect to each other as well as the illuminating system, decide the final quality of the image. For the high resolution, the operation of lenses requires power supplies having high degree stability. The modern electron microscopes are controlled via software installed in the computer.

### c) Image recording

Monochromatic image is formed by electrons, in order to make the image visible to the eye the electrons are fallen on a fluorescent screen present in the microscope column or another way by digital capture of the image. The images are saved in computers and finally, can be used for analyzing purposes.

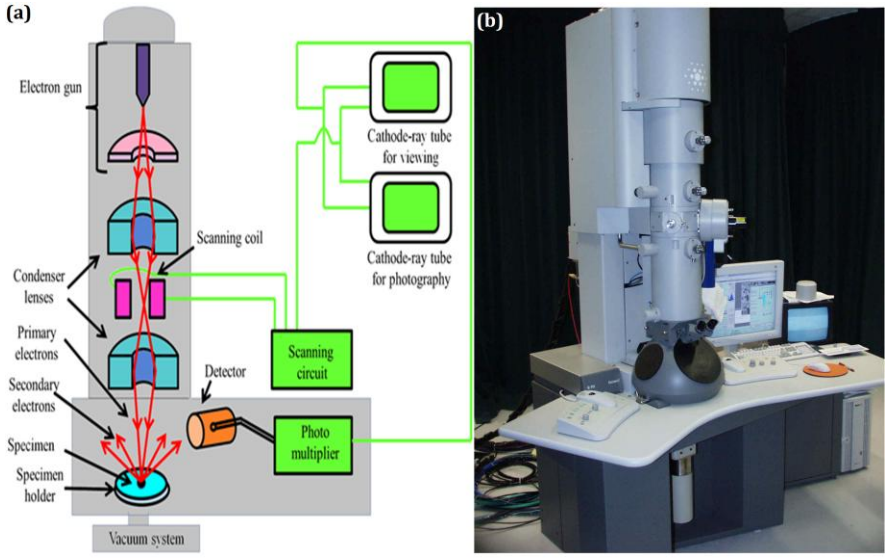


Fig. 2.6 (a) Schematic outline [176] and (b) pictorial view of a TEM [177]

### 2.2.3.3 Sample preparation

Firstly, the powdered samples were ground to form a smooth powder. Then the powdered sample was dispersed in ethanol, and subjected to ultrasonication. A drop or two of this solution was spread on carbon coated copper grid to perform the analysis.

### 2.2.3.4 Information from TEM

It finds wide applications in the field of nanotechnology, biology, materials research, industry, metallurgy, forensic sciences, geophysics, etc. The details of information are given as under:

- It provides topographical, morphological, particle size and crystalline information of the material.
- Compositional analysis.
- Crystalline investigations are done by switching to the diffraction pattern (Selected area electron diffraction; SAED) of a specimen region at the same time. It helps in identification of crystalline structure from the lattice distances of the material. It also helps in determining crystallinity of the material.
- High resolution transmission electron microscopy (HRTEM) enables imaging of lattice fringes, which again provides structural details. One can visualize the defects and interfaces at atomic scale.

*In the present thesis, TEM micrographs of the synthesized nanoparticles were recorded on transmission electron microscope (TEM; Hitachi (H-7650) and Philips (CM200)).*

### 2.2.4 Vibrating sample magnetometer

#### 2.2.4.1 Introduction

The vibrating sample magnetometer (VSM) is a simple yet an effective technique employed for characterizing the magnetic properties. This instrument is credited to S. Foner and thus, sometimes known as Foner magnetometer [178-179]. It is based on the Faraday's law of induction [180] and relies on the detection of induced emf in a coil when a magnetized sample is vibrated in its vicinity. The induced emf generates electrical signal in the pick-up coils. The electrical signal is directly proportional to the magnetization of the sample.

### 2.1.4.2 Instrumentation and working principle

The operation of VSM is quite simple. Fig. 2.7 (a) shows the block diagram of VSM. The pictorial view of a VSM has been shown in Fig. 2.7 (b). The main components of a VSM can be mainly divided into four categories and their details are as under [180]:

**a) Oscillating sample mount**

Firstly, the sample under investigation is placed in a DC uniform magnetic field so that the magnetic domains get aligned. Then sample is placed on a non magnetic rod, which is oscillated by a mechanical drive. It is mounted to a x-y-z translator so as to ensure centre positioning of the sample between the magnet poles. Drinking straws also provide enough strength and rigidity and hence are used as the shaft of the sample mount.

**b) Experimental magnetic field**

The magnetic field is provided by an air-cooled electromagnet in between whose pole pieces the sample is placed. The magnetic field is measured by a Gauss-meter whose Hall probe is placed close to the sample position. The detection coils are mounted to the electromagnet. The pick-up coils assembly are important as these determine the resolution of the system.

**c) Signal detection**

The ac signal is measured and in order to reduce the signal-to-noise ratio lock-in amplifier is used. Its purpose is to provide a signal to the mechanical vibrator and also, serve as the reference signal for the lock-in. The oscillatory motion of the sample induces voltage in the pick-up coils, which is proportional to the magnetization, in accordance with the Faraday's law. The induced voltage is amplified and recorded with the lock-in amplifier.

### d) Automated data collection

At each field setting, the induced signal read by the lock-in amplifier is transferred to the computer having software that enables the experimental control as well as data acquisition. Once a field cycle is complete, the data is plotted and saved.

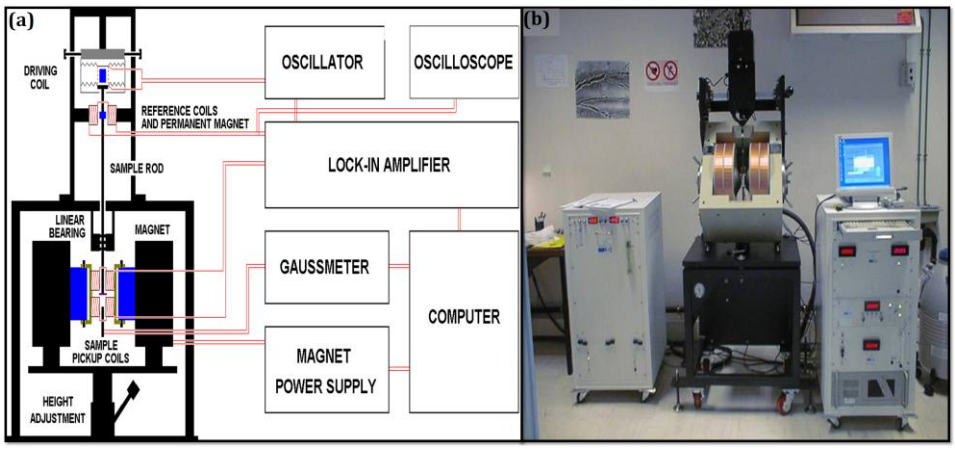


Fig. 2.7 (a) Block diagram [181] and (b) pictorial view of a VSM [182]

### 2.2.4.3 Sample preparation

The measurements were carried out using finely ground powder having weight 3 mg to 0.1 g.

### 2.2.4.4 Information from VSM

- Determination of the hysteresis curve of a magnetic material.
- Identification of nature of magnetism i.e. paramagnetism, ferromagnetism, diamagnetism, antiferromagnetism and ferrimagnetism can be done.
- Determination of various magnetic parameters such as magnetic saturation, retentivity, coercivity, exchange bias and vertical asymmetry.

- The magnetic recording materials, CMR, GMR, spin valve, magneto-optical materials can also be studied using VSM.
- The temperature response of the various magnetic parameters, hysteresis curves can also be checked with additional accessories in VSM. These can enable the both below and above room temperature dependent studies.

*In the present thesis, M-H curves of the synthesized nanoparticles were recorded on VSM: Princeton Applied Research Model 151/155* and *Lake Shore Cryotronics 7400.*

### 2.2.5 Dielectric measurement

#### 2.2.5.1 Introduction

Dielectric materials exhibit the unique property of storing electric charge on application of external electric field. The dielectric constant of a material placed between two parallel plate capacitors of area $A$ and distance $d$ with air as the medium having dielectric constant $\varepsilon_o$ can be given as under:

$$\varepsilon = \frac{C}{C_o} \tag{2.1}$$

where $C_o = \frac{\varepsilon_o A}{d}$ and $C = \frac{\varepsilon \varepsilon_o A}{d}$ are the capacitances with and without the dielectric material, respectively [183]. In these materials, the electrons do not flow under applied electric field however; these slightly shift from their equilibrium positions and create an internal field. The dielectric measurements in the present thesis have been performed by LCR meter 4284 A. The name LCR meter derives from the measurement of inductance, capacitance and resistance.

### 2.1.5.2 Instrumentation and working principle

The measurement system of a typical LCR meter is based on the automatic balancing bridge method, as shown in Fig. 2.8 (a) [184]. A brief explanation of the circuit is given as follows [185-186]:

A high gain amplifier set the gain level automatically so that electric current starts drawing through the resistor (R). Here, R always equals the current flowing through the device under test (DUT). In other words, the lower voltage side i.e. potential of DUT is always equal to the zero electric potential i.e. virtual ground level. At this condition the impedance value of DUT is calculated from the R, output ($E_1$) and input ($E_2$) voltage as under:

$$Z_x = R\frac{E_1}{E_2} \tag{2.2}$$

where $E_1$ and $E_2$ are given as

$$\begin{aligned} E_1 &= |E_1|\theta_1 = |E_1|\cos\theta_1 + |E_1|\sin\theta_1 \\ E_2 &= |E_2|\theta_2 = |E_2|\cos\theta_2 + |E_2|\sin\theta_2 \end{aligned} \tag{2.3}$$

$\theta_1$ and $\theta_2$ - the phase angles of $E_1$ and $E_2$ are calculated at the same time. The pictorial view of LCR meter is shown in Fig. 2.8 (b).

### 2.2.5.3 Sample preparation

For the measurement, the powder was finely ground along with PVA (Poly vinyl alcohol) as a binder. Further, these were compacted in a uniaxial press at pressure of 10ton/cm$^2$ to form cylindrical pellets of diameter 10 mm and thickness 1 mm. Finally, the

pellets were sintered at 500 °C and there circular surfaces were coated with silver paste to form contacts.

### 2.2.5.4 Information

- Determination of the dielectric constant and loss of a material.
- The temperature as well as frequency dependent studies of the dielectric constant and loss can be performed. These provide information regarding the type of relaxation behaviour, defects, conductivity, etc. in a system.
- Determination of various electric parameters such as capacitance, real and imaginary impedance, real and imaginary permittivity, conductivity and activation energy.

*In the present thesis, frequency response of dielectric constant as well as loss were recorded on LCR meter: Agilent 4284 A* and *PSM 1735.*

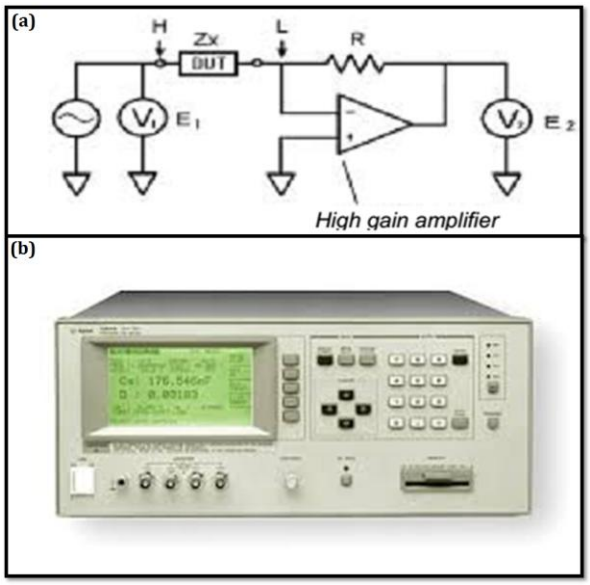


Fig. 2.8 (a) Block diagram [186] of automated balancing bridge and (b) pictorial view of a Agilent LCR meter 4284 A [187]

### 2.2.6 P-E loop tracer

#### 2.2.6.1 Introduction

On application of electric field to a material having positive and negative charges, these charges get displaced in a direction towards the opposite ends of the electric field. The local dipoles are created inside the material. The dipole moment per unit volume of the material is the summation over the individual dipole moments in that volume and is known as polarization. Several mechanisms are responsible for the polarization in a material and a brief description of each is given as under [188]:

**a) Electronic polarization**

The displacement of nucleus (positively charged) and electrons (negatively charged) away from each other in an atom on application of electric field results in electronic polarization. The extent of the displacement depends on the strength of the applied electric field.

**b) Ionic polarizability**

In case of ionic solids, when an electric field is applied the cations and anions are displaced in opposite directions. The ionic polarizability may be defined as the shift of the ions with respect to other oppositely charged neighbour. It is different from electronic polarization as in it the shift of electron cloud relative to nucleus is involved.

**c) Orientation polarization**

This type of polarization occurs in molecules having electronegativity difference (for e.g. $CH_3Cl$). These carry net dipole moment even in the absence of electric field. On application

of electric field these align themselves in its direction. This alignment results in polarization known as orientation polarization.

**d) Space charge polarization**

It results from the accumulation of the charges at the electrodes, grain boundaries or any other interface due to their limited motion.

Thus, the total polarization of a material is the sum of the above contributions from various sources.

The Sawyer Tower circuit was firstly used by C. B. Sawyer and C. H. Tower to measure the ferroelectric hysteresis loop of Rochelle Salt in 1930 [189]. It is a very practical circuit for characterizing ferroelectrics and studying their fundamental parameters spontaneous polarization, remanent polarization, coercive field and polarization reversal [190].

### 2.1.6.2 Instrumentation and working principle

The ferroelectric measurements were carried out using P-E loop tracer based on Sawyer Tower circuit, as shown in Fig. 2.9 (a). It is the original method for measurement of ferroelectric hysteresis measurements and possesses quite simple principle of operation [191]. When two capacitors are connected in series, the charge on them is same. Following are the components of the Sawyer Tower circuit [192]:

**a)** two capacitors: fixed capacitor of known capacitance and ferroelectric sample to be measured

**b)** function generator

**c)** an oscilloscope.

The function generator generates ac voltage and the x- and y-axes of oscilloscope shows potential across the standard capacitor. The voltage drop across the standard capacitor is proportional to the charge ($V = \frac{Q}{C}$). However, if the voltage across the standard capacitor increases then the voltage drop across the sample decreases (back voltage effect) [193]. Thus, the standard capacitor is chosen in such a way that it is very large than the sample under investigation. It implies that the standard capacitor has to be adapted to every investigated sample. The pictorial view of a P-E loop tracer has been shown in Fig. 2.9 (b).

#### 2.2.6.3 Sample preparation

The sample preparation procedure for the ferroelectric measurements is same as that of the dielectric measurement.

#### 2.2.6.4 Information

- Determination of the polarization-electric hysteresis loop of a material.
- Determination of various electric parameters such as remanent polarization, coercive field, saturation polarization, maximum field applicable i.e. breakdown.
- The temperature dependent polarization measurements can be performed to check the temperature response of the hysteresis curve and its various parameters.
- The fatigue measurements can be performed to check the performance of the ferroelectric sample over a number of cycles.
- The response of fatigue measurements at various temperatures can also be performed to determine the performance of the sample at various temperatures.

*In the present thesis, polarization electric field hysteresis loops have been measured using P-E loop tracer: Marine India.*

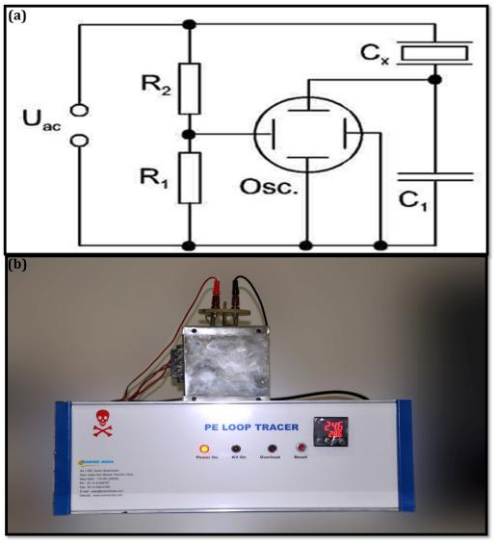


**Fig. 2.9** (a) Block diagram [194] of Sawyer Tower circuit and (b) pictorial view of P-E loop tracer [195]

# *Chapter 3*

---

# *RARE EARTH METAL IONS DOPED-*

# *$BiFeO_3$*

# *NANOPARTICLES*

# Chapter 3

The present chapter deals with the experimental procedures employed to the undoped and rare earth (Tb, Dy, Gd)-doped $BiFeO_3$ nanoparticles as well as varying their particle sizes. Their structural, morphological, magnetic, dielectric and ferroelectric properties have been discussed.

Following are the communications corresponding to undoped and rare earth doped-$BiFeO_3$ nanoparticles. Some of the results have been discussed in this chapter.

1. Gitanjali Dhir, Poonam Uniyal, N. K. Verma, Sol–gel synthesized $BiFeO_3$ nanoparticles: Enhanced magnetoelelctric coupling with reduced particle size, J. Magn. Magn. Mater. 394 (2015) 372-378.

2. Gitanjali Dhir, Gurmeet Singh Lotey, Poonam Uniyal, N. K. Verma, Size-dependent magnetic and dielectric properties of Tb-doped $BiFeO_3$ nanoparticles, J Mater. Sci.: Mater. Electron. 24 (2013) 4386-4392.
3. Gitanjali Dhir, Poonam Uniyal, N. K. Verma, Effect of particle size on magnetic and dielectric properties of nanoscale Dy-doped $BiFeO_3$, J Supercond. Nov. Magn. 27 (2014)1569–1577.
4. Gitanjali Dhir, Poonam Uniyal, N. K. Verma, Enhancement in magnetic and electrical properties of $Bi_{0.95}Tb_{0.05}FeO_3$ nanoparticles with reducing size, J Mater. Sci.: Mater. Electron. 26 (2015) 3538-3544.
5. Gitanjali Dhir, Poonam Uniyal, N. K. Verma, Effect of particle size on multiferroic properties of Tb-doped $BiFeO_3$, J. Supercond. Nov. Magn. (2016) 1-8.

.

## 3.1 $BiFeO_3$ nanoparticles

### 3.1.1 Synthesis

$BiFeO_3$ nanoparticles were prepared by sol-gel method [152]. A stoichiometric ratio of $Bi(NO_3)_3.5H_2O$ and $Fe(NO_3)_3.9H_2O$ were dissolved in ethylene glycol under constant magnetic stirring at 70 $^0$C. Tartaric acid was added in the ratio of 1:1 molar ratio with respect to precursors to the above solution. After continuous stirring of above solution for 15 h, sol completely turned into brownish gel. The gel was dried at 90 °C and ground into powders. The so-obtained powder were calcined at different temperatures viz. 450 °C (Bi4), 550 °C (Bi5), and 650 $^0$C (Bi6) for 4 hour.

### 3.1.2 Results and discussion

#### 3.1.2.1 Structural and phase analyses

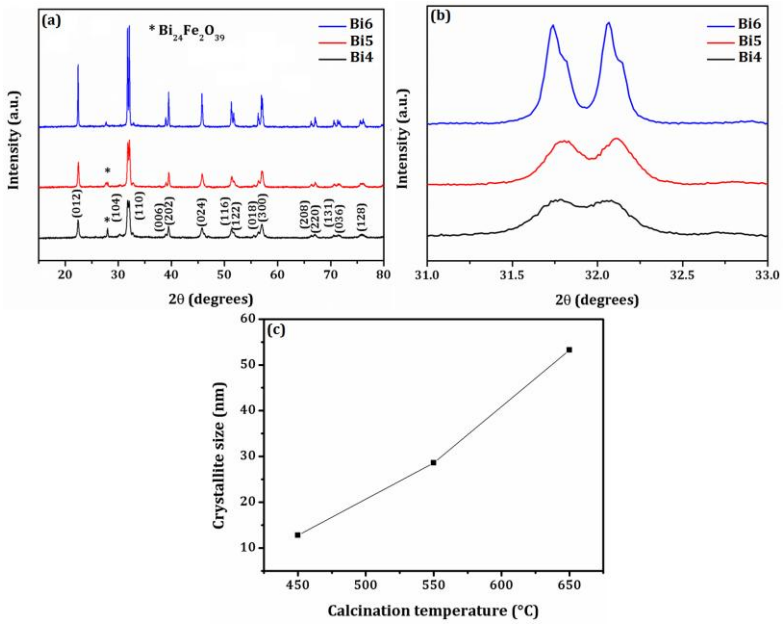


Fig. 3.1 (a) XRD patterns of Bi4, Bi5 and Bi6 nanoparticles (b) their enlarged XRD patterns at around 2θ ~ 32° and (c) variation of crystallite size with calcination temperature

Fig. 3.1 (a) shows XRD patterns of the synthesized nanoparticles, where all diffraction peaks characterize rhombohedral structure (JCPDS Card No. 86-1518). Peaks denoted by (*) are attributed to $Bi_{24}Fe_2O_{39}$ (JCPDS Card No. 42-0201). Typical broadened peaks in XRD patterns illustrate formation of nanocrystallites. The average crystallite size (D) of the synthesized nanoparticles was calculated using Debye-Scherrer equation given below [196].

$$D = \frac{0.9\lambda}{\beta \cos\theta} \tag{3.1}$$

where $\beta$ is the full width at half maximum of the most intense peak, $\lambda$ is the Cu target wavelength (1.5406 Å) and $\theta$ is the glancing angle. The values obtained are given in Table 3.1.

The influence of different calcination temperatures on the crystal structure of the synthesized nanoparticles has also been investigated with the help of XRD data. Rhombohedral phase remains consistent with increasing calcination temperature. Enlarged (Fig. 3.1 (b)) view of XRD patterns reveal broadening of peaks with decreasing calcination temperature, indicating decreasing crystallite size. The variation of crystallite size as a function of calcination temperature has been shown in Fig. 3.1 (c). This observation corroborates well with crystallite size values, determined from Eq. 3.1.

### 3.1.2.2 Morphological analysis

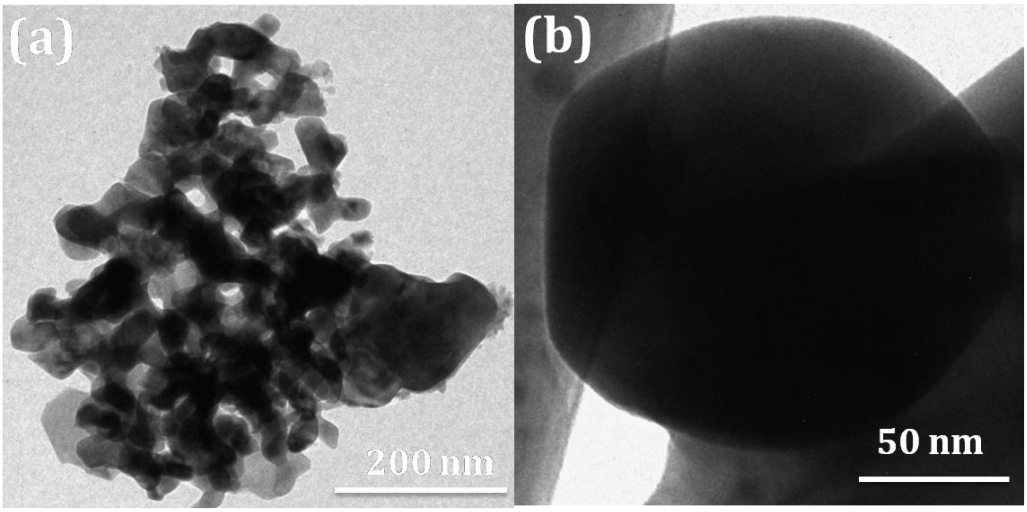


Fig. 3.2 TEM micrographs of (a) Bi4 and (b) Bi6 nanoparticles

Topographical investigations, carried out using TEM, revealed agglomerated nanoparticles (Fig. 3.2 (a) and (b)). Agglomeration is an inherent property of nanoparticles owing to their high surface to volume ratio. Similar observations, reported earlier, are attributed to high surface energy [108, 130].

Tuning of size via calcination temperature has shown immense influence over the multiferroic properties of nanoscale $BiFeO_3$. However, the underlying growth phenomenon has not been well studied. Many phenomena (ostwald ripening, heterogeneous nucleation, homogeneous nucleation, etc.) describe growth of nanoparticles [153]. Here the growth mechanism of nanoparticles formed by sol-gel can be explained by thermodynamic homogeneous nucleation [18]. It is based on minimization of Gibb's free energy. Nucleation of a solid phase from a supersaturated (exceeding the solubility) solution involves high Gibb's free energy and it reduces through segregation of solute for maintenance of equilibrium. The reduced Gibb's free energy leads to both nucleation and growth. The Gibb's

free energy per unit volume ($\Delta G_v$) having atomic volume $\Omega$, supersaturation $\sigma$ and temperature $T$ is given below [18].

$$\Delta G_v = -\frac{kT}{\Omega}\ln(1+\sigma) \tag{3.2}$$

where $\sigma = \frac{C - C_o}{C_o}$, $C$ and $C_o$ are the concentration of the solute and equilibrium concentration and k is the Boltzmann constant. The conditions for the occurrence and non-occurrence of nucleation are $C \geq C_o$ and $\sigma = 0$, respectively. The reduction in Gibb's free energy is balanced by increase in surface energy due to the formation of new phase and the total change in chemical potential ($\Delta G$) for forming a nucleus of radius r can be written as below.

$$\Delta G = \frac{4\pi r^3 \Delta G_v}{3} + 4\pi r^2 \gamma \tag{3.3}$$

where $\Delta G_v$ is the Gibb's free energy per unit volume and $\gamma$ is the surface energy per unit area. However, a nuclei formed will be stable only if its radius is greater than critical size ($r^* = -2\frac{\gamma}{\Delta G_v}$) and possess critical energy ($\Delta G^* = \frac{16\pi\gamma}{(3\Delta G_v)}$). Subsequent to the initial nucleation, concentration of growth species starts decaying and so does the Gibb's free energy. Hence, no further nuclei are formed but the growth continues until equilibrium concentration is achieved. The critical size of the formed nuclei can be reduced by reducing the surface energy of the new phase ($\gamma$) and increasing the change in Gibb's free energy ($\Delta G_v$). Further, $\Delta G_v$ can be enhanced by increasing supersaturation and

Eq. 3.2 indicates that supersaturation increases with decreasing temperature. Thus, smaller nuclei are formed at lower formation temperature. It can be concluded that the formation temperature has significant influence on the shape and size of the nanoparticles, which is well exhibited in the TEM micrographs (Fig. 3.2). Average particle size was found to be 27.3 and 153.2 nm for Bi4 and Bi6 nanoparticles, respectively.

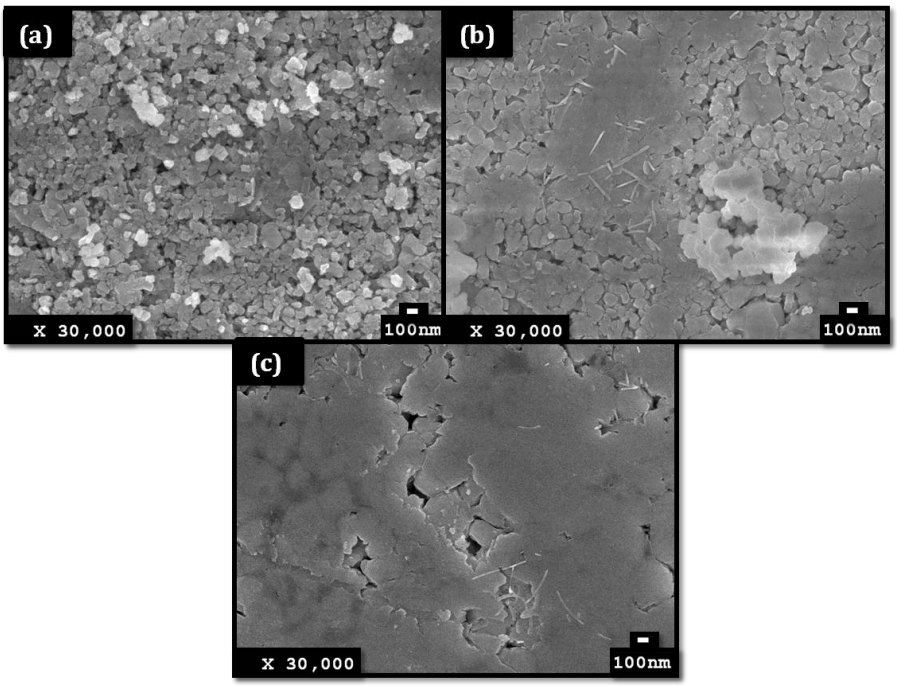


Fig. 3.3 FEG-SEM micrographs of (a) Bi4 (b) Bi5 and (c) Bi6 nanoparticles at 30k X and length scale of 100 nm

The microstructural surface properties were investigated by FEG-SEM, which revealed densely packed grains having well-defined boundaries (Fig. 3.3) thereby indicating their crystalline nature. The variation in microstructure and average grain size with increasing calcination temperature, at 30k X and length scale of 100 nm, is presented in Fig. 3.3. Significant effect of calcination temperature on the grains has been observed: The grains formed at smaller calcination temperature coalesce to form bigger ones via diffusion through grain boundaries [197] - this observation is also in agreement with the XRD results.

### 3.1.2.3 Magnetic analysis

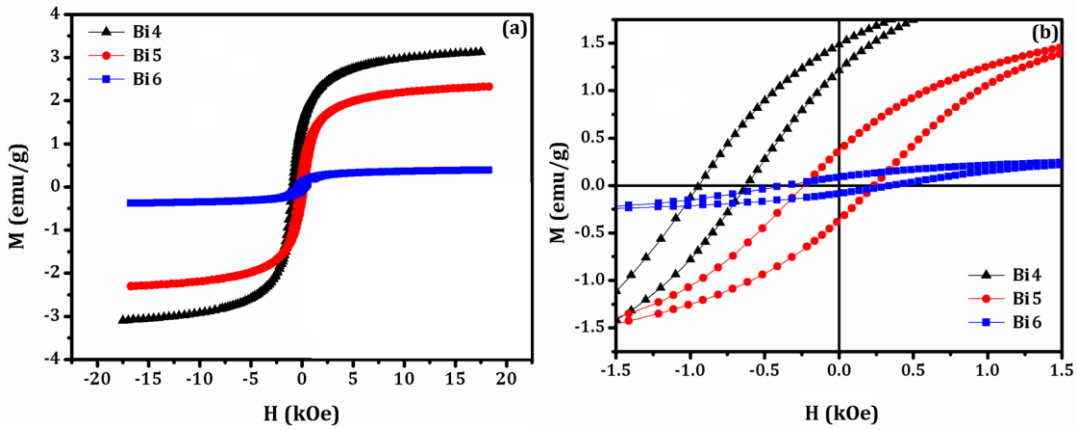


Fig. 3.4 (a) Room temperature M-H loops of Bi4, Bi5, and Bi6 nanoparticles and (b) their enlarged views

Fig. 3.4 shows room temperature M-H loops of the synthesized nanoparticles. The contribution of the impurity revealed in XRD (Fig. 3.1), towards the observed magnetism, is ruled out as it doesn't exhibit room temperature ferromagnetism [130]. The nanoparticles are found to exhibit ferromagnetism, contrary to its bulk counterpart (antiferromagnetic) [108]. Following are the attributed reasons [110]: (i) according to Néel's theory, nanoparticles possessing small antiferromagnetic display measurable magnetization due to incomplete spin compensation between two spin sublattices (ii) the larger surface to volume ratio of the nanoparticles enhances the contribution of uncompensated surface spin and (iii) the particle size suppresses spin spiral structure of $BiFeO_3$ being below 62 nm (TEM) due to grain size confinement effect.

Saturation magnetization value ($M_s$) has been found to increase with reduction in particle size (Table 3.1) - it is typical for antiferromagnetic nanoparticles [152]. On reducing size, surface to volume ratio increases and so does uncompensated spin's contribution. Also, grain size confinement effect comes into play below 62 nm [110]. This effect modulates spin

cycloid, which results in strongly size-dependent magnetism. The observed $M_s$ values are higher than the $BiFeO_3$ nanoparticles of comparable size reported by Park et al. [110].

A material can be put to device applications by using exchange bias mechanism, which exploits the magnetoelectrically coupled antiferromagnetic and ferroelectric orders; this is so because the control of exchange bias by electric field via magnetoelectric coupling results in change of magnetization. Thus, magnetization can be tuned by electric field, which would result in electronically writable spintronics devices [198]. Exchange interaction between pinned uncompensated spins in antiferromagnetic core and moments in ferromagnetic surface result in exchange bias [135]. The exchange bias field ($H_{eb}$) has been calculated using equation [107].

$$H_{eb} = \frac{H_{C1} - H_{C2}}{2} \tag{3.4}$$

where $H_{C1}$ and $H_{C2}$ are the absolute positive and negative coercive field values. The calculated $H_{eb}$ values are shown in Table 3.1. A highly shifted hysteresis loop in Bi4 has been observed (Fig. 3.4 (b)). Particle size variation leads to exchange bias variation in the system. It is observed to increase with decreasing particle size. The reason may be attributed to the lowering density of uncompensated spins with the decreasing particle surface area, which is also well in agreement with the Néel's theory implied on the synthesized samples. Moreover, the unstable charge configuration of $Fe^{2+}$ would require generation of oxygen vacancies, which, in turn, decrease the uncompensated spins and consequently decrease the exchange bias. This observation indicates increasing oxygen vacancies with calcination temperature. The decreasing uncompensated spins also well explain the decrease of $M_s$ with reduction in particle size.

The magnetic hysteresis curves of nanoparticles unveil the presence of vertical shift ($M_{shift}$), which has been calculated using equation [199].

$$M_{shift} = \frac{M_{sat}^{+} + M_{sat}^{-}}{2} \tag{3.5}$$

where $M_s^+$, $M_s^-$ are the absolute positive and negative saturation magnetization values. This rarely found $M_{shift}$ indicates the uncompensated spins at the ferromagnetic-antiferromagnet interface. This intriguing observation of vertical shift, present in the synthesized nanoparticles, has been found to vary with particle size. Both $H_{eb}$ and $M_{shift}$ have been found to follow the same trend i.e. increase with reducing particle size (Table 3.1). Thus, particle size is an essential factor that controls $M_s$, $H_{eb}$ and $M_{shift}$.

Table 3.1 Structural, magnetic, and electrical parameters of Bi4, Bi5 and Bi6 nanoparticles

| Sample | Structural parameters | | | | Magnetic parameters | | | Electric parameters | | | | |
|---|---|---|---|---|---|---|---|---|---|---|---|---|
| | D nm | a Å | c Å | V $Å^3$ | $M_s$ emu/g | $H_{eb}$ Oe | $M_{shift}$ emu/g | $\varepsilon$ @ 0.1 kHz | Loss @ 0.1 kHz | $P_r$ $\mu C/cm^2$ | $P_s$ $\mu C/cm^2$ | $E_c$ kV/cm |
| Bi4 | 12.7 | 5.585 | 13.822 | 431.1 | 3.12 | 0.1650 | 0.2001 | 272 | 0.03 | 3.32 | 4.82 | 11.59 |
| Bi5 | 28.6 | 5.582 | 13.825 | 430.7 | 2.13 | 0.0025 | 0.0203 | 246 | 0.08 | 1.41 | 2.00 | 4.08 |
| Bi6 | 53.2 | 5.573 | 13.842 | 429.9 | 0.38 | 0.0020 | 0.0052 | 233 | 4.20 | 9.03 | 0.80 | 3.63 |

### 3.1.2.4 Electrical analysis

#### 3.1.2.4.1 Dielectric analysis

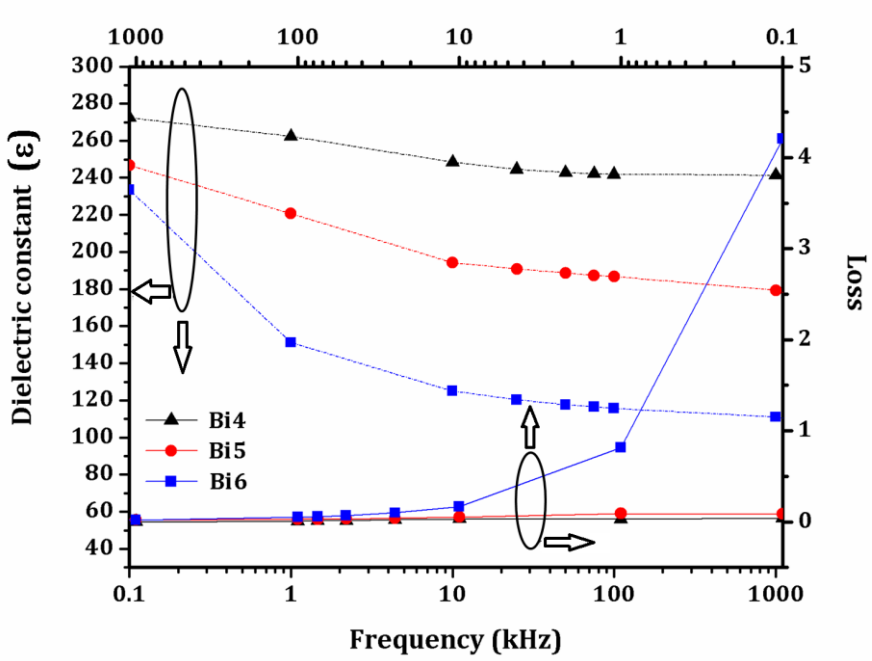


Fig. 3.5 Frequency response of dielectric constant and loss of Bi4, Bi5 and Bi6 nanoparticles in the range 0.1-1000 kHz

All the nanoparticles display Debye-type relaxation [137]. Dielectric constant (ε ) decreases with increasing frequency, as shown in Fig. 3.5. The dispersions observed in the dielectric behavior indicate the space charge polarization [137]. In $BiFeO_3$, oxygen and bismuth vacancies, lattice distortions and defects are sources of space charges [152]. These space charges follow applied field at lower frequencies, but do not get time to undergo relaxation at higher frequencies. Also, amongst four types of polarizations (electronic, dipolar, ionic, and interfacial), only electronic polarization contributes at high frequencies. This also decays dielectric constant at higher frequencies [76-77].

Enhanced dielectric constant at 100 Hz (Table 3.1), with reducing particle size, is attributed to the presence of nanosize grains (Fig. 3.3) [130]. These result in low leakage current and hence, low loss. These provide large insulating barrier to conduction current [130, 152]. Thus, smaller grains efficiently prevent conductivity than the larger ones and consequently, the dielectric constant decreases. The decrease in number of oxygen vacancies, indicated by increasing exchange bias in magnetic analysis, is well supported by the reducing loss observed with decreasing particle size.

### 3.1.2.4.2 Ferroelectric analysis

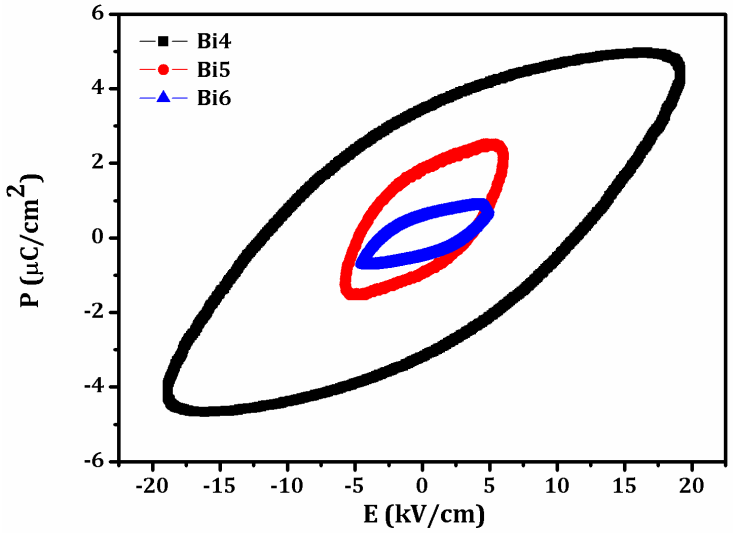


Fig. 3.6 Room temperature P-E loops of Bi4, Bi5 and Bi6 nanoparticles

To obtain a well saturated P-E loop has been a challenge for $BiFeO_3$ owing to its low resistivity [110]. The variable oxidation states of iron i.e. $Fe^{2+}$, $Fe^{3+}$ need oxygen vacancies for the compensation of charge, which, thus, leads to conductivity in the system. Table 3.1 shows electrical parameters (spontaneous polarization ($P_s$), remanent polarization ($P_r$) and coercive field ($E_c$) obtained from the hysteresis loops. Fig. 3.6 demonstrates P-E loops of the synthesized nanoparticles. Relatively high polarization values, at low applied electric field,

have been observed as compared to the report on $BiFeO_3$ nanoparticles by Wang et al. [121]. Reduction in particle size has quite effective influence on ferroelectric properties. No saturated hysteresis loops have been observed for Bi6 and Bi5 nanoparticles, which indicate high conductivity of the samples. However, Bi4 nanoparticles exhibit well saturated hysteresis loop with high polarization value. The reason may be attributed to the reduced loss due to the insulation provided by smallest nanosize grains (FEG-SEM) [130]. It has been observed that $P_s$ as well as applied electric field decay drastically with increasing particle size. This observation corroborates well with the dielectric analysis, which also shows enhanced conductivity with particle size [200]. Thus, higher resistivity has enabled the observation of better P-E loops in reduced size. Moreover, the increasing $P_r$ with reducing size approves of the decreasing losses due to leakage current.

## 3.2 Tb-doped $BiFeO_3$ nanoparticles

### 3.2.1 Synthesis of Tb-doped $BiFeO_3$ nanoparticles ($Bi_{1-x}Tb_xFeO_3$; x = 0, 0.05, 0.10, 0.15 and 0.20)

Undoped and Tb-doped $BiFeO_3$ ($Bi_{1-x}Tb_xFeO_3$; x = 0, 0.05, 0.10, 0.15 and 0.20) nanoparticles were synthesized using sol-gel method [152]. A schematic presenting the various synthesis steps is shown in Fig. 3.7. A stoichiometric ratio of $Bi(NO_3)_3.5H_2O$, $Tb(NO_3)_3.5H_2O$ and $Fe(NO_3)_3.9H_2O$ dissolved in ethylene glycol, was taken, and stirred magnetically at 70 $^0$C. The low heating temperature ensures homogeneous and small size of the nanoparticles. This was followed by addition of tartaric acid in 1:1 molar ratio with respect to the precursors. It acts as the fuel for combustion and chelating agent to form complexes with metal ions. The solution so obtained was stirred till it became gel. The gel was then dried for overnight at 90 $^0$C in an oven, and ground into powder. Undoped (x = 0)

and Tb-doped $BiFeO_3$ (x = 0.05, 0.10, 0.15 and 0.20) nanoparticles were obtained by calcination at 450 $^0$C for 4 hour.

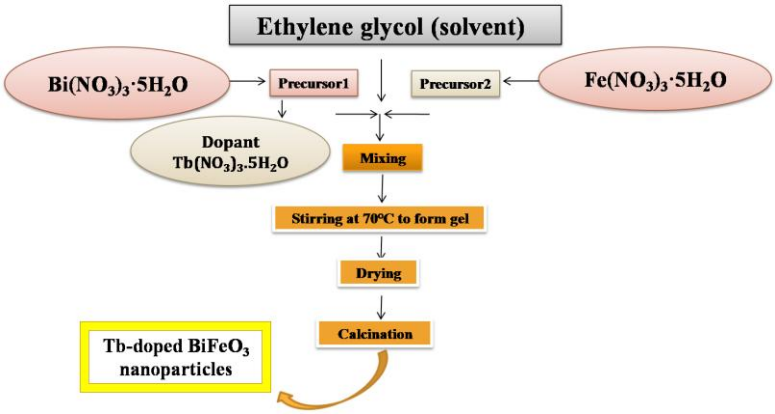


Fig. 3.7 Schematic representation of synthesis of Tb-doped $BiFeO_3$ nanoparticles

### 3.2.2 Results and discussion

#### 3.2.2.1 Structural and phase analyses

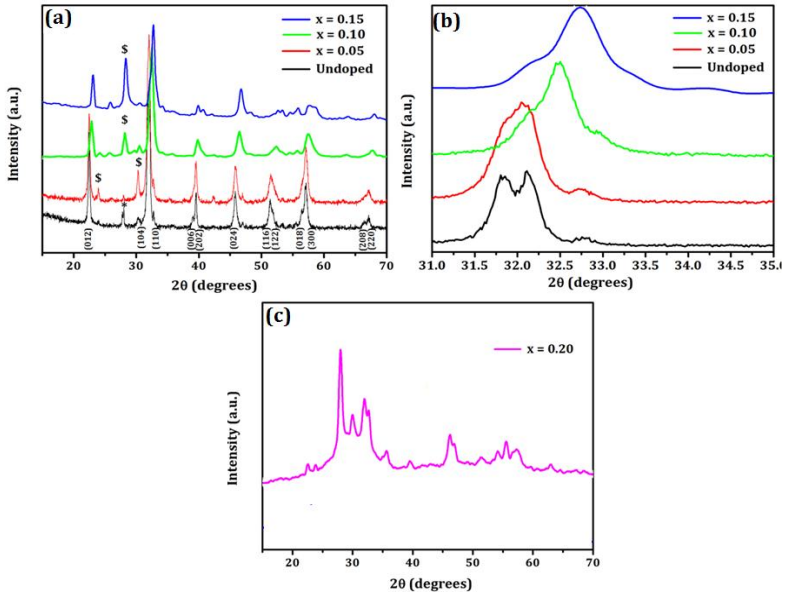


Fig. 3.8 (a) XRD patterns of undoped (x = 0) and $Bi_{1-x}Tb_xFeO_3$ (x = 0.05, 0.10 and 0.15) nanoparticles at room temperature (b) their enlarged view around 2θ ~ 32° (c) XRD patterns of $Bi_{1-x}Tb_xFeO_3$ (x = 0.20) nanoparticles

Fig. 3.8 (a) shows XRD patterns of $Bi_{1-x}Tb_xFeO_3$ (x = 0, 0.05, 0.10 and 0.15) nanoparticles. The diffraction peaks of undoped $BiFeO_3$ characterize rhombohedral structure having $R_{3c}$ space group (JCPDS Card No. 86-1518). Minor traces of impurities (Fig. 3.8 (a)) have been observed in the XRD patterns denoted by * and $, which correspond to $Bi_{24}Fe_2O_{39}$ (JCPDS Card No. 42-0201) and $Tb_2O_3$ (JCPDS Card No. 26-0177), respectively. Fig. 3.8 (b) shows the enlarged view of XRD patterns at around 2θ ~ 32° and the obvious effects on the $BiFeO_3$ crystal structure has been found on Tb-doping. With increasing Tb-doping concentration, some noticeable features have been observed in the XRD patterns. Tb-doping has resulted in distortion of the rhombohedral structure of $BiFeO_3$. The merging of peaks (104) and (110) at around 2θ ~ 32° (Fig. 1 (b)) into a single broad peak, which further shifts towards higher 2θ, indicates the onset of orthorhombic structure [132]. This result is consistent with the other rare earth doped $BiFeO_3$ nanoparticles in which the contribution from the rhombohedral phase decreases while from orthorhombic phase increases at the 15% concentration of rare earth ion [76-77, 136]. The shifting of peak towards higher 2θ with increasing Tb content confirms successful substitution of $Tb^{3+}$ ions at $Bi^{3+}$ site [129]. Also, the diffraction peaks tend to broaden with the increasing Tb-concentration, which indicates the decrease of crystallite size. The reason may be attributed to the smaller ionic radii of $Tb^{3+}$ ions (0.923 Å) as compared to $Bi^{3+}$ ions (1.17 Å) [129].

On increasing the concentration of $Tb^{3+}$ ions to x = 0.20 (Fig. 3.8 (c)) high impurity content has been observed thereby indicating good dispersivity of $Tb^{3+}$ ions into $BiFeO_3$ lattice upto x = 0.15. This observation indicates the solution limit of the system to be around x = 0.15.

It has been observed from the XRD patterns that in our case x = 0.15 is the solubility limit and also literature reveals enhancement in electric and magnetic properties with

increasing concentration [129-141]. Accordingly, the concentration has thus been optimally chosen to be x = 0.15, in the present thesis, to carry out the further studies (particle size dependent studies).

### 3.3 Tb-doped $BiFeO_3$ nanoparticles ($Bi_{1-x}Tb_xFeO_3$; x= 0, 0.15)

#### 3.3.1 Synthesis

The procedure followed for the synthesis of undoped and Tb-doped $BiFeO_3$ (x = 0.15) nanoparticles is same as described in section (3.2.1). The undoped $BiFeO_3$ nanoparticles were obtained by calcination at 450 $^0$C (undoped) for 4 hour. Nanoparticles of Tb-doped $BiFeO_3$ of different sizes have been obtained by the calcination at different temperatures viz., 450 $^0$C (Tb4), 550 $^0$C (Tb5) and 650 $^0$C (Tb6) for 4 hour.

#### 3.3.2 Results and discussion

#### 3.3.2.1 Structural and phase analyses

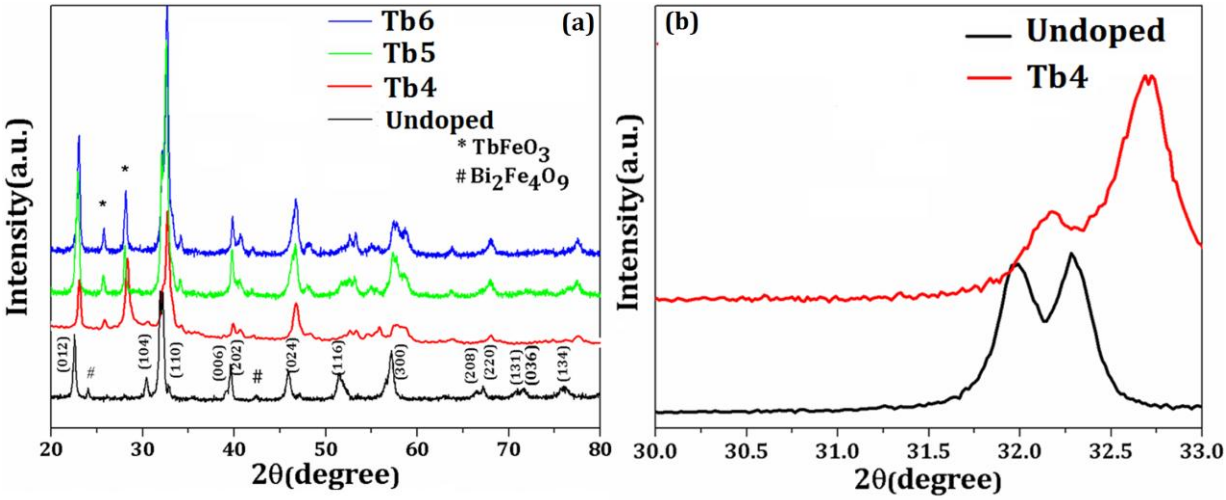


Fig. 3.9 (a) XRD patterns of undoped, Tb4, Tb5 and Tb6 nanoparticles and (b) enlarged view of XRD patterns of undoped and Tb4 nanoparticles around 2θ ~ 32$^0$

The effects of doping and particle size on the crystal structure have been studied by the XRD. Fig. 3.9 (a) shows the XRD patterns of undoped, Tb4, Tb5 and Tb6 nanoparticles. The peaks associated with the undoped $BiFeO_3$ nanoparticles are well matched with the rhombohedral structure (JCPDS Card No. 86-1518). Doping of $Tb^{3+}$ ions in $BiFeO_3$ nanoparticles resulted in some notable features as shown in the Fig. 3.9 and Fig. 3.10. First, its doping induces structural transformation from rhombohedral phase to orthorhombic phase, which is in well agreement with previous reports [129-130] as well as match with $TbFeO_3$ having orthorhombic structure (JCPDS Card No. 74-1477). Fig. 3.9 (b) clearly reveals the merging of two distinctive diffraction peaks i.e. (104) and (110) around $2\theta \sim 32°$ in the Tb-doped $BiFeO_3$ nanoparticles, which are found to shift further to the higher $2\theta$. This indicates that the structural transformation has been induced by the substitution of $Tb^{3+}$ ions ($x = 0.15$). This observation confirms the distortion of rhombohedral structure of undoped $BiFeO_3$ nanoparticles by the substitution of $Tb^{3+}$ ions in the $BiFeO_3$ lattice. This result is consistent with the other rare earth doped $BiFeO_3$ nanoparticles in which the contribution from the rhombohedral phase decreases while from orthorhombic phase increases at the 15% concentration of rare earth ion [76-77, 136]. The average crystallite size of the nanoparticles was calculated using the Debye–Scherrer equation [196]. It has been found that the doping leads to remarkable reduction of the crystallite size (Table 3.2) that resulted in the broadening of the diffraction peaks (Fig. 3.10 (a)). This is due to the substitution of larger $Bi^{3+}$ ions (1.03 Å) with the smaller $Tb^{3+}$ ions (0.923 Å). The significant shift of diffraction peaks toward the larger $2\theta$ in doped nanoparticles with respect to the undoped one indicates that the $Tb^{3+}$ ions has substituted the $Bi^{3+}$ ions in the lattice and hence is responsible for the above features.

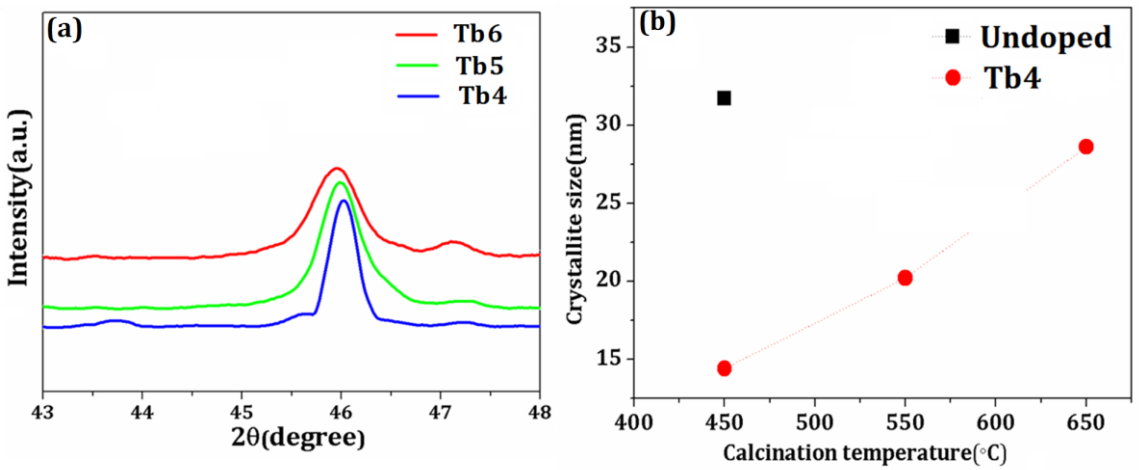


Fig. 3.10 (a) Enlarged view of XRD patterns around 2θ ~ 43 - 48° and (b) Crystallite size of undoped and Tb-doped $BiFeO_3$ nanoparticles calcined at different temperatures

The investigation of the effect of different calcination temperatures on the crystal structure has also been done with the help of XRD data. The peaks for Tb4 nanoparticles are more broadened and tend to sharpen as the temperature rises to 550 °C and then to 650 °C. The peaks denoted by (*) in Tb-doped $BiFeO_3$ are attributed to terbium oxide ($Tb_2O_3$) matching with the JCPDS Card No. 74-2131.However, it does not display any room temperature ferromagnetism [201], thereby ruling out the possibility of its contribution towards magnetization. The significant effect of different calcination temperatures on the Tb-doped $BiFeO_3$ nanoparticles has been revealed by Fig. 3.9 and Fig. 3.10. The enlarged view of peaks around 2θ ~ 43 - 48°, displays the sharpening of the XRD peaks (Fig. 3.10 (a)) with the increase in calcination temperature, thereby indicating their higher crystallite size and crystallinity as compared to undoped $BiFeO_3$ nanoparticles. Fig. 3.10 (b) shows the variation of average crystallite with calcination temperatures and Tb-doping, revealing that the crystallite size increases with increase of calcination temperature in doped samples. The shifting of diffraction peaks with the doping as well as with the variation of calcination temperature in illustrates the change of lattice parameters. The values of lattice parameters (a,

b, c) and volume (V) have been summarized in Table 3.1. It has been found that compression of lattice takes place by the substitution of $Tb^{3+}$ ions in $BiFeO_3$. The reason may be attributed to the substitution of smaller $Tb^{3+}$ ions in place of larger $Bi^{3+}$ ions.

### 3.3.2.2 Morphological analyses

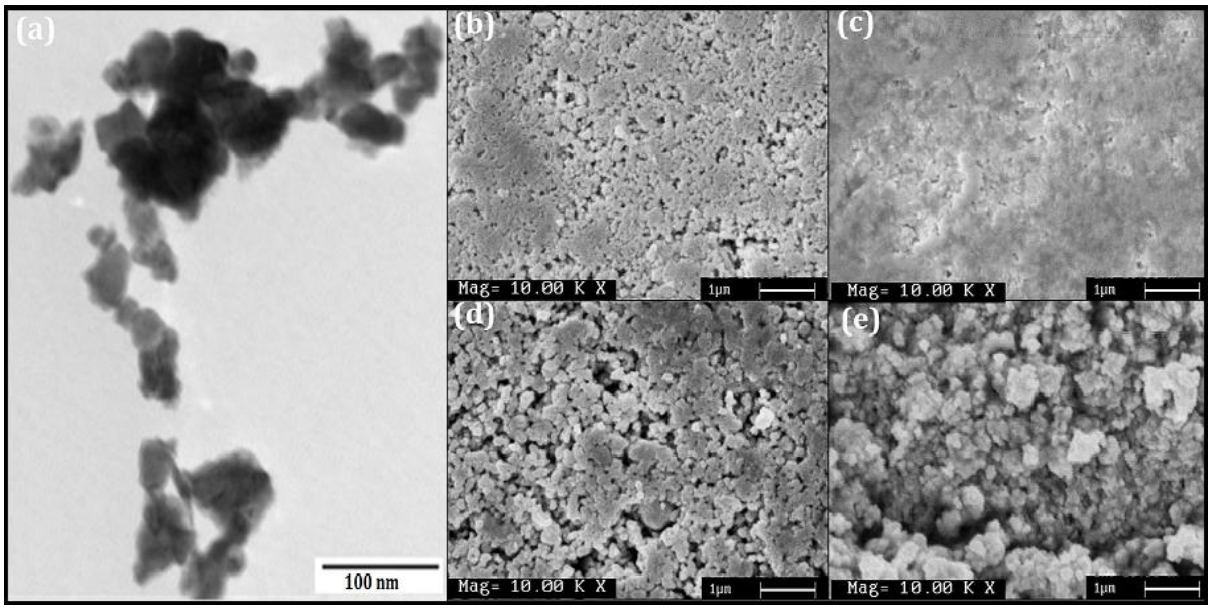


Fig. 3.11 (a) TEM image of undoped $BiFeO_3$ nanoparticles and SEM micrographs of (b) undoped (c) Tb4, (d) Tb5 (e) Tb6 nanoparticles at the same magnification (10,000 X)

TEM has been carried out in order to investigate the topography of the nanoparticles. Fig. 3.11(a) shows that the synthesized undoped $BiFeO_3$ nanoparticles are in agglomerates. The agglomeration is due to two reasons: one, high surface to volume ratio, and second, magnetic interactions in nanoparticles. The average particle size has been found to be 40 nm. The mean crystallite size, as determined by Scherrer's equation is slightly smaller than the average particle size. The typical agglomerates found in the TEM image are the reason for such an observation [110]. Such phenomenon has also been reported previously [108, 130, 133]. Many phenomena are attributed to the growth of nanoparticles [18]. Here the growth mechanism of the nanoparticles formed by sol-gel method can be explained by

thermodynamic homogeneous nucleation [153]. The detailed description of the mechanism is given in section 3.1.2.2.

Scanning electron micrographs of undoped, Tb4, Tb5 and Tb6 nanoparticles are shown in Fig. 3.11 (b)-(e). All the micrographs were captured at the same magnification i.e. 10,000 X. It has been observed that the decrease of grain size takes place with the doping of 15% Tb in $BiFeO_3$ nanoparticles as shown in Fig. 3.11 (b) and 3.11 (c). The grain size has been witnessed to increase as the calcination temperature increased from 450 $^0$C (Fig. 3.11 (c)) to 550 $^0$C (Fig. 3.11 (d)) and, it further increased at 650 $^0$C (Fig. 3.11 (e)). Fig. 3.11 illustrates that the coalescence of the Tb-doped $BiFeO_3$ nanoparticles increases as the calcination temperature increases. So, it is apparent that the increase of crystallite size takes place as a function of increasing calcination temperature.

### 3.3.2.3 Magnetic analysis

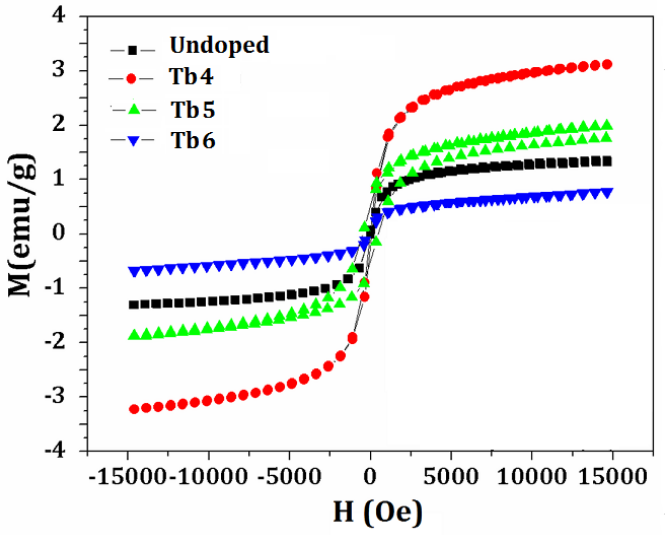


Fig. 3.12 The room temperature magnetization versus applied magnetic field (M-H) curves of undoped, Tb4, Tb5 and Tb6 nanoparticles

Fig. 3.12 shows the room temperature M-H curves of undoped, Tb4, Tb5 and Tb6 nanoparticles. The magnetic hysteresis loops of the samples indicate the typical ferromagnetic behavior, as reported in the rare earth ion doped $BiFeO_3$ nanoparticles [130-131, 133, 202]. A significant increase in magnetization has been observed with doping of $Tb^{3+}$ ions. The saturation magnetization value for undoped $BiFeO_3$ nanoparticles has been found to be 1.33 emu/g while that of Tb4 nanoparticles has been found to be 3.11emu/g. The enhancement in ferromagnetism with doping can be possibly attributed to the following three reasons. First, in accordance with the Néel's theory, the enhancement in magnetization in small antiferromagnetic $BiFeO_3$ nanoparticles is attributed to the spin non-compensation between the magnetic sub-lattices. As the antiferromagnetic order at the particle's surface gets interrupted, incomplete spin compensation gives rise to a measurable magnetization [130]. Also, the surface to volume ratio is large in nanoparticles; the uncompensated spins at the surface give a noticeable contribution to the particles overall magnetization [110]. Secondly, on the suppression of the spin cycloid structure [135] of $BiFeO_3$, by the reduction of particle size to 40 nm (below 62 nm, as revealed by the TEM image) and substitution of smaller $Tb^{3+}$ ions in place of $Bi^{3+}$ ions, a large lattice distortion takes place. This lattice distortion is due to the structural transformation (rhombohedral to orthorhombic) with 15% Tb ion doping in $BiFeO_3$ nanoparticles, which destroys the spin spiral structure and thereby leading to enhanced magnetization. Third, the $Tb^{3+}$ ions are magnetically active with the effective magnetic moment of 9.72 $\mu_B$/mol, and when it couples with $Fe^{3+}$ ion, it leads to the enhancement of the magnetization [132]. The obtained saturation magnetization value is higher than sol-gel synthesized Tb-doped $BiFeO_3$ nanoparticles reported by Lotey et al. [151].

The influence of the size of the synthesized nanoparticles on the magnetic moment has also been observed. The saturation magnetization value has been found to decrease with the increase in size of Tb-doped nanoparticles (Table 3.2). The monotonic decrease in the magnetization with the increase in particle size (below 62 nm) is quite obvious. As the particle size increases, the surface to volume ratio decreases and so does the contribution of the non-compensated spins present on the surface. This observation is consistent with the previous reports on size dependent studies of $BiFeO_3$ nanoparticles [107, 110]. The magnetic response of $Bi_{1-x}Tb_xFeO_3$ (x = 0, 0.15) below 62 nm is size dependent, which is due to the grain size confinement that modifies its spin spiral structure [110].

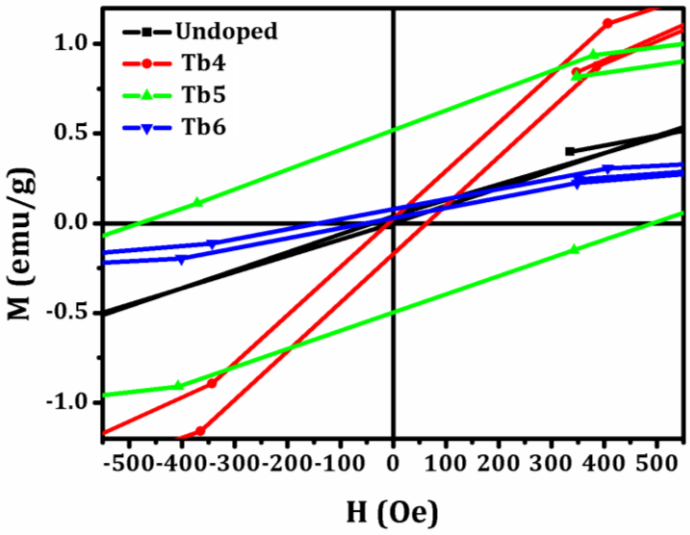


Fig. 3.13 Shifting in hysteresis loops of the undoped, Tb4, Tb5 and Tb6 nanoparticles

Fig. 3.12 exhibits the enlarged view of central region of the M-H curves of all the synthesized nanoparticles. The presence of finite $H_{eb}$ and $M_{shift}$ has been observed in all the synthesized nanoparticles. Their respective values have been calculated using Eq. 3.4 and 3.5, which are summarized in Table 3.2.

The shift in the hysteresis loops is due to exchange coupling between the ferromagnetic surface and antiferromagnetic core [135]. The presence of finite coercivity and exchange bias field rules out the possibility of superparamagnetic behavior in the nanoparticles; this confirms the ferromagnetic order and pinning of spins at the antiferromagnetic-ferromagnetic interfaces [107, 135, 147].

The presence of rarely observed vertical shift has been revealed by the M-H loops. It confirms the presence of uncompensated spins at the ferromagnetic-antiferromagnet interface. The intriguing $M_{shift}$ shows significant particle size dependence. It has been observed to increase with reduction in particle size (Table 3.2). It may be owed to the lowering density of uncompensated spins with the decreasing particle surface area, which corroborates well with the Néel's modelling of the system. Thus, particle size is of immense importance in deciding the various magnetic parameters.

Table 3.2 Structural, magnetic and electric parameters of undoped, Tb4, Tb5 and Tb6 nanoparticles

| Sample | Structural parameters | | | | | Magnetic parameters | | | Electric parameters | | | | |
|---|---|---|---|---|---|---|---|---|---|---|---|---|---|
| | D nm | a Å | b Å | c Å | V $Å^3$ | $M_s$ emu/g | $H_{eb}$ Oe | $M_{shift}$ emu/g | $\varepsilon$ @ 0.1 kHz | Loss | $P_s$ $\mu C/cm^2$ | $P_r$ $\mu C/cm^2$ | $E_c$ kV/cm |
| Undoped | 31.7 | 5.574 | 5.574 | 13.781 | 428.2 | 1.3 | 5.2 | 1.3 | 725 | 0.4 | 2.6 | 1.4 | 10.4 |
| Tb4 | 14.5 | 5.411 | 5.573 | 7.700 | 232.2 | 3.1 | 11.2 | 3.2 | 4163 | 1.2 | 10.0 | 6.2 | 30.1 |
| Tb5 | 20.2 | 5.570 | 5.590 | 7.710 | 232.4 | 2.0 | 7.9 | 1.94 | 2083 | 1.0 | 6.1 | 4.1 | 25.4 |
| Tb6 | 28.6 | 5.577 | 5.578 | 7.754 | 234.0 | 0.8 | 44.3 | 0.72 | 1388 | 1.1 | 4.2 | 2.4 | 26.3 |

### 3.3.2.4 Electrical analysis

#### 3.3.2.4.1 Dielectric analysis

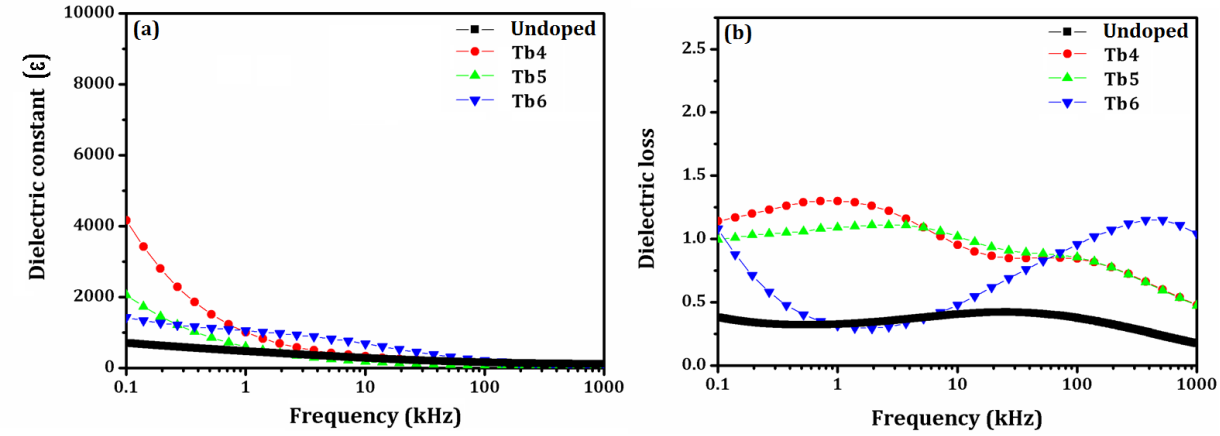


Fig. 3.14 Frequency dependence of (a) dielectric constant and (b) dielectric loss of undoped, Tb4, Tb5 and Tb6 nanoparticles in the range 0.1-1000 kHz

Fig. 3.14 shows room temperature frequency dependence of dielectric constant and dielectric loss for the undoped, Tb4, Tb5 and Tb6 nanoparticles. In all the synthesized nanoparticles, the dielectric constant value has been found to decrease as the frequency increases. Since, the contribution to the dielectric constant value in the low frequency region is from the different kind of polarizations (electronic, atomic, interfacial, and ionic etc.) while at higher frequencies only the electronic polarization contributes [203]. Hence, the dielectric constant value decreases at higher frequencies. But, at higher frequencies the trend of dielectric constant has been found to be constant for all the samples. This phenomenon is attributed to space charge relaxation due to the fact that the space charges follow the applied field at low frequencies while, at high frequencies, they are unable to undergo relaxation; thus, the dielectric value remains constant [204].

The increase in the dielectric constant value has been observed with the doping of $Tb^{3+}$ ions in $BiFeO_3$ nanoparticles (Table 3.2). This increase in the value may be due to the structural distortion (as revealed by XRD) induced by the substitution of Tb in the $BiFeO_3$ [76-77]. Also, Tb-doped $BiFeO_3$ nanoparticles have been found to show significant frequency dispersion. However, low frequency dispersion has been observed for undoped $BiFeO_3$ nanoparticles due to the presence of oxygen vacancies, leading to finite conductivity [203]. This indicates the presence of less charge defects in the Tb-doped $BiFeO_3$ nanoparticles.

The significant effect of the particle size on the dielectric constant has been observed. The dielectric constant values have been found to decrease with the increase in the size of Tb-doped $BiFeO_3$ nanoparticles (Table 3.2). This observation is in contradiction to the other studies. Since, grain and grain boundaries present in the polycrystalline nanoparticles have an important role in deciding the electrical properties. The reason for such an observation may possibly due to the role of the nanosize grains [130, 202], which act as large insulating barriers, thereby giving rise to increase in the dielectric constant and low loss values for the smaller size of Tb-doped $BiFeO_3$ nanoparticles. Since, the average grain size for Tb4, Tb5 and Tb6 are nearly same so, another deciding factor may also be the porosity of the samples, which also plays an important role in deciding the dielectric properties.

The dielectric loss proportional to imaginary part of the dielectric constant represents the energy dissipation of the system. The resonance peaks observed in the loss spectra are indicative of correlation of dielectric polarization of the sample and conduction mechanism [133]. The low losses (Table 3.2) may be attributed to the nanosized grains, giving rise to large insulating barriers between the grains, i.e., low leakage current [130]. Thus, the observed decrease in loss with the Tb doping in $BiFeO_3$ nanoparticles may be possibly due to the lowering of the grain size, which further improves the dielectric properties.

### 3.3.2.4.2 Ferroelectric analysis

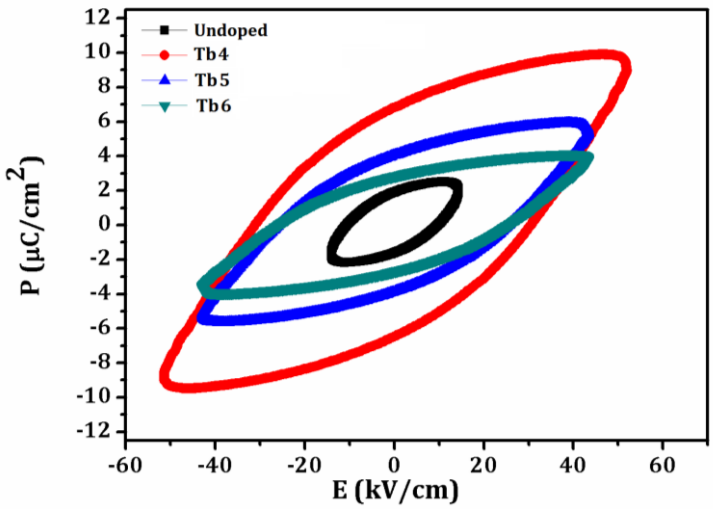


Fig. 3.15 Ferroelectric hysteresis loops of undoped, Tb4, Tb5 and Tb6 nanoparticles at room temperature

Fig. 3.15 shows room temperature P-E hysteresis loops of the synthesized nanoparticles at frequency of 100 Hz. The electric hysteresis parameters obtained from the P-E loops are summarized in Table 3.2.

The polarization in $BiFeO_3$ results due to displacement of Bi vis a vis $FeO_6$ octahedra, which is the result of stereochemically active $6s^2$ lone pair of Bi [133]. In general, the defects and non-stoichiometric issues prevent the observation of well-saturated P-E loops in $BiFeO_3$ [205]. To measure the P-E loops, voltage was varied in steps until the breakdown of the sample. All the synthesized nanoparticles have been found to show different breakdown voltages. The doping of $Tb^{3+}$ ions in $BiFeO_3$ lattice has resulted in enhanced ferroelectric properties. The spontaneous polarization as well as the applied electric field values have been found to increase with doping of $Tb^{3+}$ ions (Table 3.2). The enhancement in ferroelectric behavior may be attributed to two reasons [76-77, 129]. One, rhombohedral distortion of $BiFeO_3$ lattice into orthorhombic structure (as revealed by XRD) due to ionic radii mismatch

indicating the reduction of centre of symmetry with the introduction of $Tb^{3+}$ ions in $BiFeO_3$ lattice. Second, the lowering of space charges and leakage current density due to decrease in average grain size by Tb-doping. The substitution of $Tb^{3+}$ ions at volatile $Bi^{3+}$ ions site reduces the secondary phase formation, and thus enhances the resistivity if the system.

Particle size has been found to play a vital role in deciding the ferroelectric properties of the synthesized nanoparticles. The $P_s$ value decays with increasing particle size. Also, the samples are unable to withstand higher electric field with increasing particle size. This indicates that increasing particles size leads to increase in leakage current. The presence of nanosized grains in the synthesized nanoparticles (FEG-SEM) acts as a large insulating barrier to the mobile charge carriers [130]. The particle size, found to increase with the grain size, decreases the insulating behaviour, which, in turn, decays ferroelectricity. This observation points towards the increasing defects and vacancies (oxygen and bismuth) with the increasing particle size as both of these are well known sources for enhancing the conductivity and thus lead to leakage current in $BiFeO_3$.

## 3.4 Dy-doped $BiFeO_3$ nanoparticles ($Bi_{1-x}Dy_xFeO_3$; x= 0, 0.15)

### 3.4.1 Synthesis

The synthesis of $Bi_{1-x}Dy_xFeO_3$ (x = 0.15) nanoparticles was carried out via sol-gel method same as described in section (3.2.1). $BiFeO_3$ nanoparticles were acquired by calcining at 450 $^0$C (P4). 15% Dy-doped $BiFeO_3$ nanoparticles of different sizes were then obtained by the calcination at different temperatures viz., 450 $^0$C (Dy4), 550 $^0$C (Dy5) and 650 $^0$C (Dy6) for 4 hour.

### 3.4.2 Results and discussion

#### 3.4.2.1 Structural and phase analyses

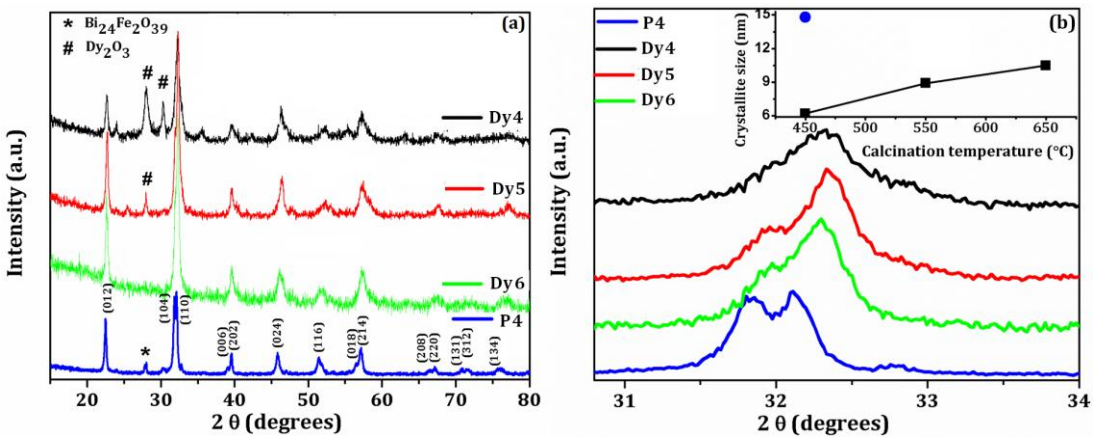


Fig. 3.16 (a) XRD patterns of P4, Dy4, Dy5 and Dy6 nanoparticles at room temperature and (b) enlarged view of XRD patterns around 2θ ~ 31 - 34°. Inset shows the variation of crystallite size as a function of calcination temperature.

The structural and phase investigations were carried out in order to study the influence of Dy-doping and calcination temperature on $BiFeO_3$ nanoparticles. Fig. 3.16 (a) shows the XRD patterns of P4, Dy4, Dy5 and Dy6 nanoparticles. The lattice parameters, crystal structure and crystallite size related to the synthesized nanoparticles are summarized in the Table 3.3. From the XRD patterns of P4 nanoparticles, it has been observed that all the diffraction peaks characterize a rhomb-centered lattice of $BiFeO_3$ having $R_{3c}$ space group (JCPDS Card No. 86-1518). One additional peak observed at 2θ = 28º is attributed to $Bi_{24}Fe_2O_{39}$. The presence of this minor secondary phase does not contribute towards magnetism since; it's not room temperature ferromagnetic [130].

Remarkable features have been observed with the substitution of $Dy^{3+}$ ions in $BiFeO_3$ lattice. It has been observed that the doping of $Dy^{3+}$ ions led to a structural transformation. As, XRD patterns of Dy4, Dy5 and Dy6 nanoparticles correspond to the orthorhombic phase

of $DyFeO_3$ having Pbnm space group (JCPDS Card No. 46-0135). This observation is well supported by the merging of (104) and (110) peaks at around 2θ ~ 32º in $BiFeO_3$ nanoparticles into a single peak with the doping of $Dy^{3+}$ ions (Fig. 3.16 (b)). It is indicative of the distortion of structure from rhombohedral to orthorhombic structure due to doping [132].This is consistent with the other rare earth doped $BiFeO_3$ reports [129, 132]. The reason for the structural transformation due to $Dy^{3+}$ ions substitution is attributed to the size effects [129]. In the $R_{3c}$ structure of $BiFeO_3$ when the $Dy^{3+}$ ions with smaller ionic radius (0.912 Å) replaces $Bi^{3+}$ ions with larger ionic radius (1.17 Å) the tolerance factor (t) decreases given by the expression given below [206].

$$t = \frac{R_A + R_O}{\sqrt{2}(R_B + R_O)} \tag{3.6}$$

where $R_A$, $R_B$, and $R_O$ are the ionic radii of the atoms at A, B, and O sites.

The decrease in tolerance would lead to compression amongst Fe-O bonds and stiffness amongst $Bi^{3+}$/$Dy^{3+}$- $O^{2-}$ bonds. The stress in the lattice is relieved by the oxygen octahedra rotation [206]. The relative angle of rotation between two oxygen octahedra in the $R_{3c}$ structure along [111] polarization axis increases with the substitution of $Dy^{3+}$ ions thereby, inducing distortions in the structure [151]. Thus, the rhombohedral phase of $BiFeO_3$ becomes unstable and transforms into orthorhombic phase along with the reduction of lattice parameters and overall volume of the lattice.

It can be well observed from Fig. 3.16 (b) that, two separated peaks merged into a single broad peak which is shifted towards higher 2θ with respect to undoped one. This shift of the diffraction peaks towards the higher angle approves the substitution of $Dy^{3+}$ ions in place of $Bi^{3+}$ ions in the lattice. Since, in case of the interstitial site substitution diffraction peaks shift toward the lower angle [152]. According to the criterion of the incorporation of

guest ion into the host lattice, the substitution may be interstitial or substitutional. For the substitution to be interstitial, the ionic radius ratio of solute and solvent is 0.59. From the Shannon's ionic radius values, the ratio of $Dy^{3+}$ ion to $Bi^{3+}$ ion has been found out to be 1.28 [152]. The higher ratio indicates that the $Dy^{3+}$ atoms substitute the $Bi^{3+}$ atoms. Traces of impurity related to $Dy_2O_3$ (JCPDS Card No. 22-0259) indicated by (#) have been found in Dy4 nanoparticles. However, its contribution towards the magnetism is ruled out as, it does not display any room temperature magnetism [207]. The impurity phase detected in the XRD pattern of Dy4 nanoparticles was however, found to diminish with the raising of calcination temperature.

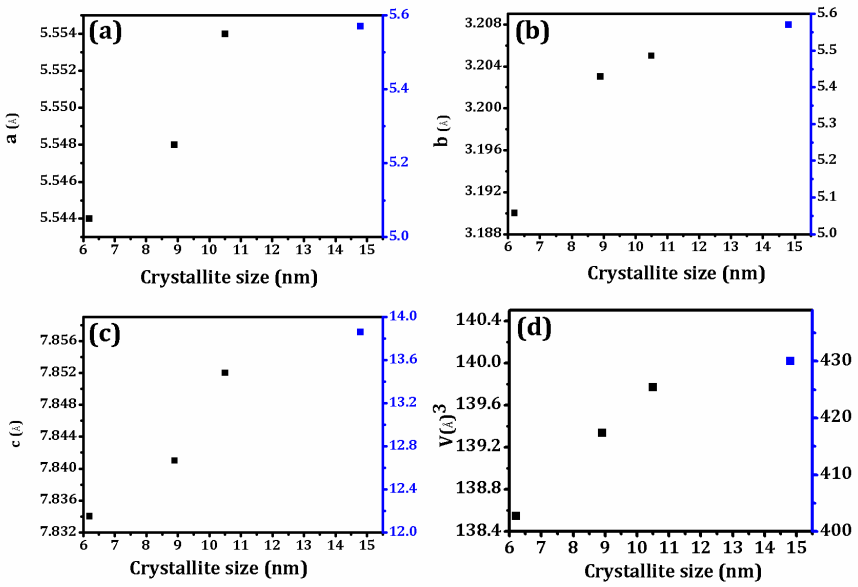


Fig. 3.17 Lattice parameters (a) a, (b) b, (c) c and (d) volume of P4, Dy4, Dy5 and Dy6 nanoparticles at room temperature

The average crystallite size of the synthesized nanoparticles has been calculated using Debye-Scherrer equation [196]. The values thus, obtained are summarized in Table 3.3. The variation of crystallite size as a function of calcinations temperature has been shown in Fig. 3.16 (b). It has been revealed that the doping of $Dy^{3+}$ ions lead to a remarkable reduction in

the crystallite size. The shifting of diffraction peaks with the doping as well as with the variation of calcination temperature in Fig. 3.16 (b) illustrates the change of lattice parameters. This can be observed in Fig. 3.17 as well, where the variation of lattice parameters (a, b, c) and volume (V) has been depicted. It has been observed (Fig. 3.17) that compression of lattice takes place by the substitution of $Dy^{3+}$ ions in $BiFeO_3$. The reason may be attributed to the substitution of $Dy^{3+}$ (0.912 Å) with smaller ionic radius in place of $Bi^{3+}$ (1.17 Å) having comparatively larger ionic radius [152].

The influence of variation of calcination temperature for the 15% Dy-doped $BiFeO_3$ nanoparticles is clearly revealed by Fig. 3.16 (b) and its inset. Along with the consistency in the phase i.e. orthorhombic, the broadening of peaks take place as the calcination temperature is decreased (Fig. 3.16 (b)). This therefore, reveals the decrease of crystallite size, which is also well in agreement with the values of average crystallite size calculated using Debye-Scherrer equation (Table 3.3).

### 3.4.2.2 Morphological analysis

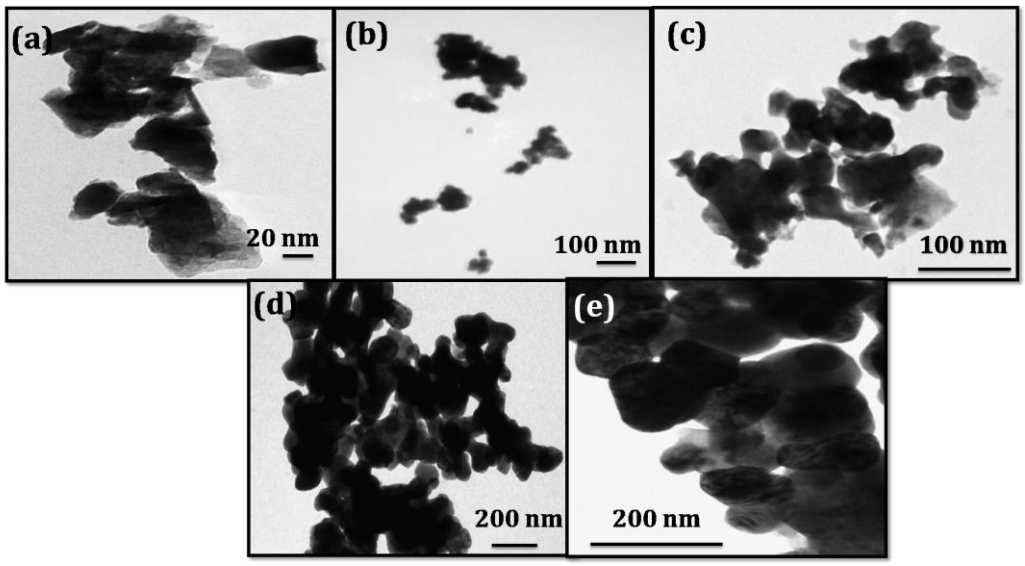


Fig. 3.18 TEM micrographs of (a) P4, (b) Dy4, (c) Dy5 and (d) Dy6 nanoparticles and (e) enlarged view of Dy6 nanoparticles

TEM micrographs of P4, Dy4, Dy5 and Dy6 nanoparticles are shown in Fig. 3.18 (a-e). It exhibits agglomerated nanoparticles of average particle size 30, 20, 45 and 86 nm for P4, Dy4, Dy5 and Dy6 respectively. Similar formation of agglomerated nanoparticles has also been reported previously [108, 130, 133]. The reason of agglomeration is attributed to the high surface energy of nanoparticles [108]. High agglomeration witnessed for Dy4, Dy5 and P4 nanoparticles than Dy6 nanoparticles is attributed to their comparatively smaller particle size. Fig. 3.19 (e) shows the enlarged view of the micrograph shown in Fig. 3.18 (d). It reveals the morphology of Dy6 nanoparticles to be nearly elliptical. Many phenomena can be (Ostwald ripening, kinetically controlled, homogeneous nucleation) attributed to the growth of nanoparticles [153]. For the present nanoparticles synthesized by sol-gel method, the growth mechanism is described by homogeneous nucleation as explained in section 3.1.2.2.

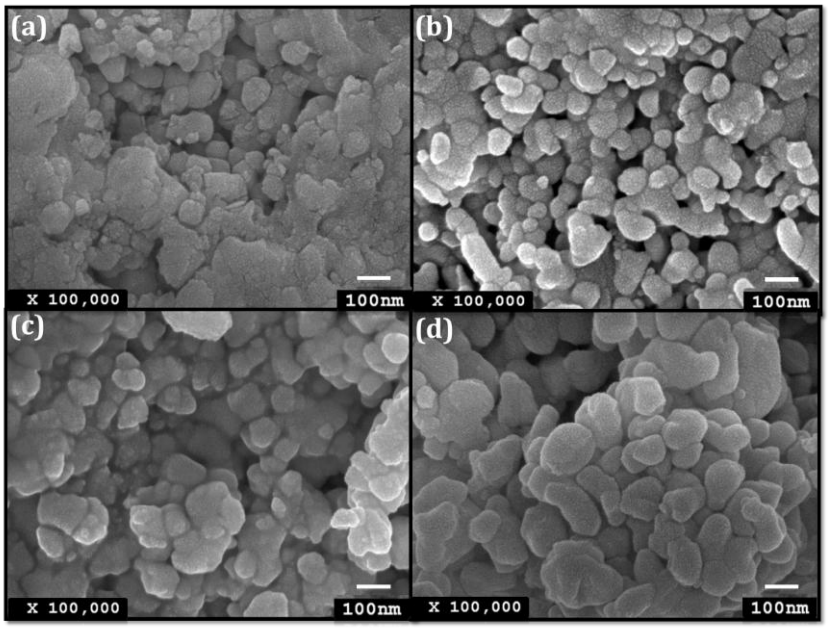


Fig. 3.19 FEG-SEM micrographs of (a) P4, (b) Dy4, (c) Dy5 and (d) Dy6 nanoparticles at the same magnification (100,000 X)

The morphological and microstructural surface properties are depicted by FEG-SEM micrographs of P4, Dy4, Dy5 and Dy6 nanoparticles (Fig. 3.19). The FEG-SEM micrographs of all the synthesized nanoparticles reveal uniform distribution of densely packed grains having well-defined boundaries indicating their crystalline nature. The morphology has been witnessed to be spherical for all the nanoparticles. Fig. 3.19 compares the microstructure and average grain size amongst all the nanoparticles at the same magnification i.e. 100, 000 X. It has been observed that doping of $Dy^{3+}$ ions in $BiFeO_3$ lattice remarkably reduced the grain size (Fig. 3.19 (b)). The reason may be attributed to the inhibition of grain growth by smaller $Dy^{3+}$ ions which, thereby, help in densification [97]. Fig. 3.19 (b), (c) and (d) clearly reveals the influence of increase of calcination temperature on the Dy-doped nanoparticles. The grains with smaller size (450 ºC) aggregate to form bigger ones (550 ºC) which further expands as the calcination temperature was raised to 650 ºC. Raising calcination temperature results in the coalescence of grains via grain boundaries [197]. This observation corroborates well with the XRD results, which also indicate the increase of crystallite size with the increasing calcination temperature. Thus, it is evident that calcination temperature has a direct influence on the size of synthesized nanoparticles.

### 3.4.2.3 Magnetic analysis

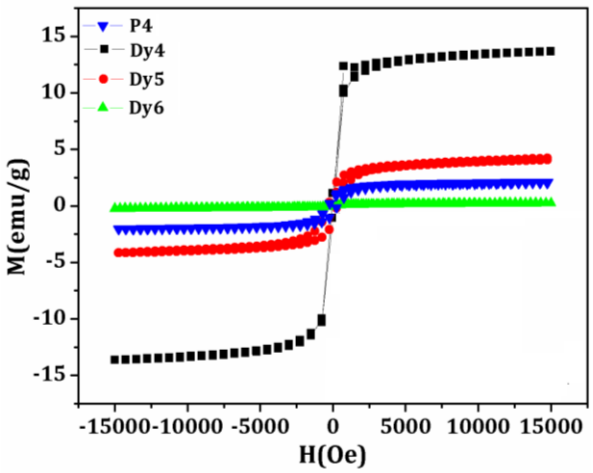


Fig. 3.20 Room temperature magnetization hysteresis loops of $BiFeO_3$ nanoparticles P4, Dy4, Dy5 and Dy6 nanoparticles

Room temperature magnetic hysteresis loops of P4, Dy4, Dy5 and Dy6 nanoparticles are shown in Fig. 3.20. The values related to magnetic parameters such as, saturation magnetization, exchange bias field and vertical asymmetry are summarized in Table 3.3. Ferromagnetism has been displayed by all the synthesized nanoparticles, which is consistent with the previous reports on rare earth doped $BiFeO_3$ nanoparticles [130, 133, 135, 152, 202].

The origin of ferromagnetic ordering in $BiFeO_3$ nanoparticles has mainly two causes. Firstly, it is owed to the magnetic ordering in $BiFeO_3$. Being an antiferromagnetic system, it comprises of spin sublattices having ferromagnetic interactions inside them but antiferromagnetic interactions amongst each other [130]. In accordance with the Néel's theory, the observation of ferromagnetic behavior in these small antiferromagnetic nanoparticles is ascribed to incomplete spin compensation amongst two spin sublattices [152]. This gives rise to a measurable magnetic moment in case of small antiferromagnetic systems as; the antiferromagnetic ordering gets interrupted at the surface of particle. Owing to the large surface to volume ratio in the nanoparticles, the non-compensated spins contribute substantially towards the enhancement of particle's overall magnetization. Secondly, it is the modification of spin cycloidal structure due to the particle size of synthesized $BiFeO_3$ being below 62 nm (spin cycloid wavelength). The average particle size of 30 nm, as revealed by TEM image, remarkably modifies the spin cycloidal structure due to grain size confinement [110]. Due to this effect, the long range spin cycloidal structure gets partially destroyed hence, gives rise to ferromagnetism.

The hysteresis loops shown in Fig. 3.20 indicate a remarkable rise in the saturation magnetization value with the doping of $Dy^{3+}$ ions. This observation is consistent with the other rare earth doped $BiFeO_3$ nanoparticles [130, 133, 135, 152, 202]. The enhancement in magnetization due to Dy - doping is attributed to three reasons. Firstly, it is the large lattice

distortion induced due to the substitution of the smaller $Dy^{3+}$ ions (0.912 Å) in place of larger $Bi^{3+}$ (1.17 Å) [129]. This results in structural change of $BiFeO_3$ (from rhombohedral to orthorhombic as revealed by XRD) which further leads to the destruction of spin cycloid. Hence, giving rise to the enhanced magnetization [132]. Second reason is the coupling of magnetically active 4f electrons of $Dy^{3+}$ ions with $Fe^{3+}$ ions as revealed by the first-principle calculations by Liu [131] and Guo [132] et al. Quite large magnetic moment of $Dy^{3+}$ ions (10.6 $\mu_B$) leads to enhancement of ferromagnetism in the present system. Thirdly, it is the suppression of oxygen ion vacancies with the doping of less volatile $Dy^{3+}$ ions at Bi-site that reduces the variable valances of Fe [202]. Here, the $M_s$ value registered with Dy-doping is quite higher than that reported by Qian et al. [130].

Correlation between magnetism and particle size of 15% Dy-doped $BiFeO_3$ nanoparticles is clearly revealed by Fig. 3.20. It has been observed that particle size controls the overall magnetism of the Dy-doped nanoparticles. The magnetization has been found to rise drastically with decreasing particle size (Table 3.3), similar to the other size dependent reports on $BiFeO_3$ nanoparticles [108, 110]. The reasons responsible are decreasing oxygen ion vacancies [130, 133, 135] and increasing surface to volume ratio [110, 130]. As explained above, in case of antiferromagnetic nanoparticles, the incomplete spin compensation at the surface of antiferromagnetic $BiFeO_3$ becomes measurable on reducing its size. With the decrease in particle size, the surface to volume ratio increases and so does the contribution of non-compensated spins present on particle's surface [110]. Since, Dy4 nanoparticles possess the smallest particle size (as revealed by TEM) it exhibits highest saturation magnetization value (13.8 emu/g) which is also well in accordance with Néel's modelling of the present system. The saturation magnetization value decreases for Dy5 and Dy6 accordingly as, the particle size increases. Thus, the present study depicts strong correlation between magnetism

and particle size in Dy-substituted $BiFeO_3$ nanoparticles. Also, in $BiFeO_3$ nanoparticles of size below 62 nm (spin cycloid wavelength) magnetic properties are strongly size-dependent, owing to the grain size confinement effect [110]. It is an effect which modulates the spin spiral structure present in $BiFeO_3$. The remarkably high saturation magnetization value at room temperature for Dy4 nanoparticles is of great interest from device application point of view.

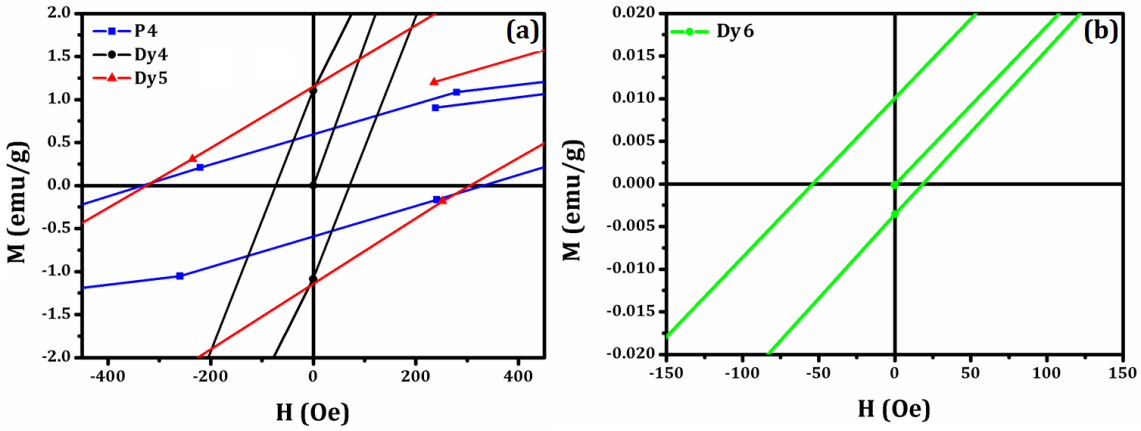


Fig. 3.21 Zoomed in view of magnetization hysteresis loops of (a) P4, Dy4, Dy5, and (b) Dy6 nanoparticles

A shift in the magnetic hysteresis loops indicating $H_{eb}$ as well as $M_{shift}$ has been observed for all the synthesized nanoparticles (Fig. 3.21). The shift is due to the exchange coupling amongst the ferromagnetic surfaces and antiferromagnetic cores [135]. The values of $H_{eb}$ (Table 3.3) have been calculated using Eq. 3.4. The presence of finite coercivity as well as exchange bias field rules out the possibility of superparamagnetism. Also, it approves the ferromagnetism and pinning of spins at the ferromagnetic-antiferromagnetic interfaces [107]. This further supports the Néel's modelling of the magnetization of synthesized nanoparticles. The room temperature coercivity is of high interest from application point of view.

The rarely observed $M_{shift}$ in the M-H loops is ascribed to the presence of uncompensated spins at the ferromagnetic-antiferromagnet interface. It is calculated using Eq. 3.5 [199]. The values thus obtained are summarized in Table 3.3. It has been observed to increase with reduction in particle size. It may be owed to the lowering density of uncompensated spins with the decreasing particle surface area, which corroborates well with the Néel's modelling of the system.

Table 3.3 Structural, magnetic and electric parameters of P4, Dy4, Dy5 and Dy6 nanoparticles

| | Structural parameters | | | | | Magnetic parameters | | | Electric parameters | | | | |
|---|---|---|---|---|---|---|---|---|---|---|---|---|---|
| Sample | D nm | a Å | b Å | c Å | V Å$^3$ | $M_s$ emu/g | $H_{eb}$ Oe | $M_{shift}$ emu/g | $\varepsilon$ Loss @ 0.1 kHz | | $P_r$ μC/cm$^2$ | $P_s$ μC/cm$^2$ | $E_c$ kV/cm |
| P4 | 14.8 | 5.57 | 5.57 | 13.86 | 430.0 | 2.2 | 2.0 | 0.82 | 699 | 0.38 | 4.2 | 3.4 | 13.4 |
| Dy4 | 6.2 | 3.19 | 5.54 | 7.83 | 138.5 | 13.8 | 2.2 | 0.07 | 11,645 | 0.36 | 12.4 | 8.3 | 41.3 |
| Dy5 | 8.9 | 3.20 | 5.55 | 7.84 | 139.3 | 4.4 | 1.8 | 0.05 | 2067 | 1.55 | 8.3 | 5.4 | 37.4 |
| Dy6 | 10.5 | 3.21 | 5.55 | 7.85 | 139.7 | 0.5 | 16.1 | 0.005 | 640 | 1.31 | 2.1 | 1.4 | 19.4 |

### 3.4.2.4 Electrical analysis

#### 3.4.2.4.1 Dielectric analysis

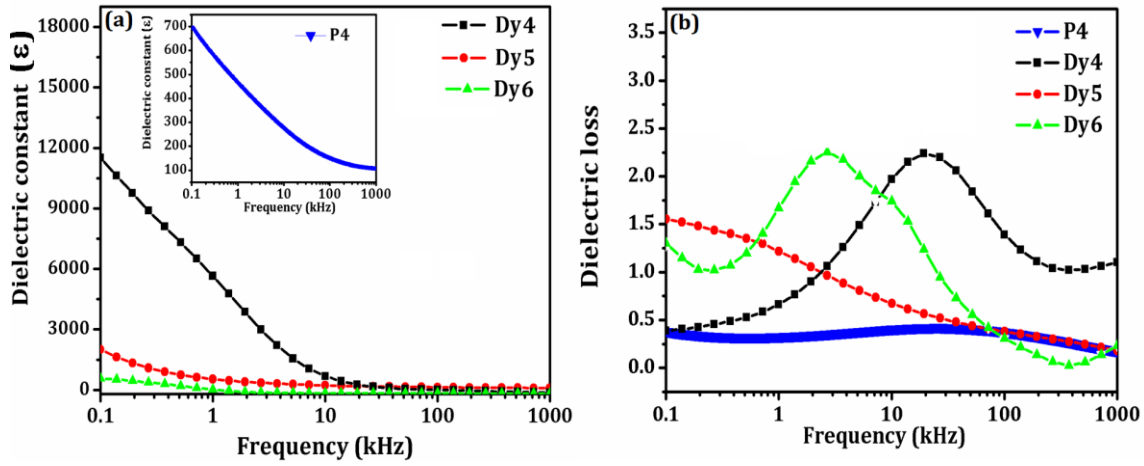


Fig. 3.22 Room temperature frequency dependence of the (a) dielectric constant of Dy4, Dy5 and Dy6 nanoparticles (b) dielectric loss of P4, Dy4, Dy5 and Dy6 nanoparticles in the range 0.1-1000 kHz. Inset shows frequency dependence of dielectric constant of P4 nanoparticles

Fig. 3.22 (a) displays the room temperature frequency dependence of dielectric constant and dielectric loss in the range 0.1-1000 kHz on the log scale. It has been observed that in all the synthesized nanoparticles the dielectric constant values descend in the lower frequency range and becomes constant thereafter. These dispersions in the dielectric behaviour are maximum for Dy4 and minimum for Dy6 (Fig. 3.22 (a)). Frequency dependence of dielectric constant has been witnessed to decrease with increasing frequency. Two reasons may be attributed to this. First, is the space charge relaxation according to the Maxwell-Wagner model associated to interfacial charge relaxation [130, 133, 135]. Oxygen and bismuth vacancies, lattice distortions, defects at the interfaces and in the grains are the sources of space charges in $BiFeO_3$ [152]. They contribute towards the dielectric constant at lower frequencies as, they are able to follow the applied field but unable to do so at higher frequencies. Secondly, different kinds of polarizations that contribute towards dielectric

constant at lower frequencies are electronic, atomic, interfacial and ionic. While, only electronic polarization contributes at higher frequencies thereby, resulting in the decrease of dielectric constant with the increasing frequency [202].

The dielectric constant for all the nanoparticles was witnessed to be of Debye-type [137]. The room temperature dielectric constant values at 0.1 kHz are summarized in Table 3.3. These values points towards a significant rise in the dielectric constant value with the Dy-doping. The reason may be attributed to the substitution induced lattice distortion (as revealed by XRD) which happens due to the smaller ionic radius of $Dy^{3+}$ ion (0.912 Å) than the $Bi^{3+}$ ion (1.17 Å) [152] and suppression of oxygen vacancies [133, 135]. Here, the Dy-doping has been found to register quite high value of the dielectric constant as compared to that reported by Qian et al. [130]. Further, dielectric constant of Dy-doped $BiFeO_3$ nanoparticles has been found to be greatly particle size-dependent. Fig. 3.22 (a) illustrates the decrease of dielectric constant with the increasing particle size. Two reasons may be attributed to this. Firstly, as grain and grain boundaries play an important role in deciding the overall dielectric properties in a material. The reason for it may be owed to the presence of nanosized grains in the synthesized nanoparticles [130]. These act as large insulating barrier for the mobile charge carriers. As, from the FEG-SEM micrographs average grain size has been found to increase with the increasing calcination temperature. The dielectric constant values have been observed to decay accordingly. So, Dy4 comprising of smallest nanograins, gives rise to large insulation as compared to Dy5 and Dy6. Thus, it indicates that grain and grain boundaries play a crucial role. Secondly, this behaviour may be due to the oxygen ion vacancies, which also play a crucial role [135]. These give rise to dc conductivity thereby, deteriorating the dielectric constant. As discussed previously, oxygen vacancies increase as

we move from Dy4 to Dy5 to Dy6. Consequently, dielectric constant has been found to decrease.

Fig. 3.22 (b) represents the frequency dependence of dielectric loss. The loss values at 0.1 k Hz have been summarized in Table 3.3. These low loss values pertain to the nanosized grains (as revealed by FEG-SEM) [130]. The dielectric loss has been found to decrease with Dy- substitution in $BiFeO_3$ (Dy4). Thus, indicating the improvement of dielectric properties with the doping. The appearance of dielectric relaxation peak has been witnessed for all the synthesized nanoparticles. The resonance peak is attributed to the matching of the natural frequency of jumping of the ions with that of the applied external field [152]. At the resonance, ions oscillate with maximum electrical energy thus, the loss values enhance remarkably.

### 3.4.2.4.2 Ferroelectric analysis

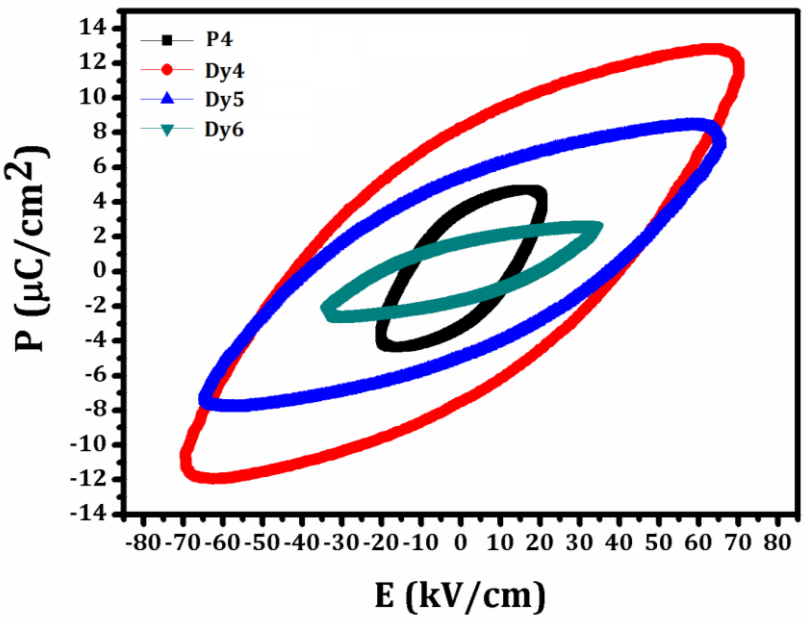


Fig. 3.23 P-E loops of P4, Dy4, Dy5 and Dy6 nanoparticles at room temperature

Room temperature ferroelectric behaviour of the synthesized nanoparticles at frequency of 100 Hz is shown in Fig. 3.23. Various polarization parameters are summarized in Table 3.3. Bulk $BiFeO_3$ is known to suffer from high leakage problems arising due to variable oxidation state of Fe, defects, oxygen vacancies, volatile nature of Bi, non-stochiometric issues and secondary phases [150-152]. Undoped $BiFeO_3$ nanoparticles have been found to exhibit better ferroelectric behaviour with respect to its bulk counterpart. The nanoscale particle size leads to increased density of the pellets (FEG-SEM; Fig. 3.19), which thus reduces the current conduction [130].

On introduction of $Dy^{3+}$ ions in $BiFeO_3$ lattice the polarization as well as the applied electric field values (Table 3.3) have been found to enhance, which means improvement of ferroelectric property by $Dy^{3+}$ ions. Dy-substitution induced rhombohedral distortion of $BiFeO_3$ due to ionic mismatch between $Dy^{3+}$ ions (0.912 Å) and $Bi^{3+}$ (1.17 Å) ions remarkably enhanced the polarization values. The bond dissociation energy of the rare-earth metal ion-oxygen (Dy-O) bond is higher than the Bi-O bond [150]. This in turn reduces the non-stoichiometric issues, space charge defect (oxygen and bismuth vacancies) and secondary phases as the $Dy^{3+}$ ions substitute volatile $Bi^{3+}$ ions. Grain and grain boundaries significantly contribute towards the electric properties. Polycrystalline nanoparticles, consisting of high grain boundary region and inhomogenity amongst the grain and grain boundaries, enhance the resistivity [133]. Since Dy-doping has been found to reduce the grain size it implies that the smaller grains in this sample (FEG-SEM; Fig. 3.19) provide better insulation barrier to the conductivity of mobile charge carriers.

Influence of particle size of Dy-doped $BiFeO_3$ nanoparticles on the ferroelectric property has also been analysed. It has been revealed that the remnant polarization and applied electric field values enhance as the particle size reduces. The possible reason is the

presence of nano-sized grains (FEG-SEM; Fig. 3.19) in the synthesized nanoparticles [130]. The smaller grains act as a better insulating barrier for the conducting charge carriers than the larger ones. Therefore, ferroelectricity has been found to enhance with the reducing particle size of Dy-doped $BiFeO_3$ nanoparticles.

## 3.5 Gd-doped $BiFeO_3$ nanoparticles ($Bi_{1-x}Gd_xFeO_3$; x = 0, 0.15)

### 3.5.1 Synthesis

The synthesis of $Bi_{1-x}Gd_xFeO_3$ (x = 0.15) nanoparticles was carried out via sol-gel method same as described in section (3.2.1). $BiFeO_3$ nanoparticles were acquired by calcining at 450 $^0$C (Bi4). 15% Gd-doped $BiFeO_3$ nanoparticles of different sizes were then obtained by the calcination at different temperatures viz., 450 $^0$C (Gd4), 550 $^0$C (Gd5) and 650 $^0$C (Gd6) for 4 hour.

### 3.5.2 Results and discussion

#### 3.5.2.1 Structural and phase analyses

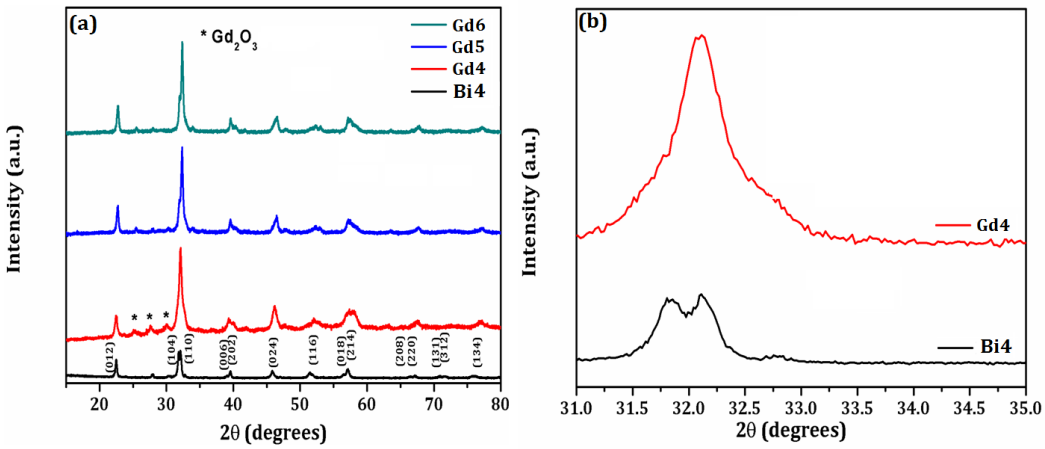


Fig. 3.24 (a) XRD patterns of Bi4, Gd4, Gd5 and Gd6 nanoparticles and (b) enlarged view of XRD patterns of Bi4 and Gd4 nanoparticles

The influence of Gd-doping and varying particle size on the crystal structure of $BiFeO_3$ has been studied by XRD. Fig. 3.24 (a) shows XRD patterns Bi4, Gd4, Gd5 and Gd6 nanoparticles. The diffraction peaks associated with undoped $BiFeO_3$ correspond to rhomb-centered lattice with $R_{3c}$space group (JCPDS Card No. 86-1518). Minute traces of impurity denoted by # and * (Fig. 3.26 (a)) correspond to $Bi_{24}Fe_2O_{39}$ (JCPDS Card No. 42-0201) and $Gd_2O_3$ (JCPDS Card No. 43-1015), respectively.

Gd-doping introduces some noticeable features in the XRD patterns. It has been observed that the doping of $Gd^{3+}$ ions results in a structural transformation. Fig. 3.24 (b) clearly reveals two distinctive diffraction peaks i.e. (104) and (110) around 2 $\theta \sim 32°$ in undoped $BiFeO_3$ nanoparticles merge to form a single peak with Gd-doping, which is further shifted to the higher 2θ. It indicates the structural transformation from rhombohedral phase to orthorhombic phase owing to the substitution of smaller $Gd^{3+}$ ions (0.938 Å) at larger $Bi^{3+}$ ions (1.17 Å) place [132]. The shifting of diffraction peaks of Gd4 nanoparticles towards the higher angle approves the successful substitution of $Gd^{3+}$ ions in $BiFeO_3$ lattice. As if the substitution would have been at interstitial site the shifting of diffraction peaks takes place towards the lower angle [152]. The values of various lattice parameters are given in Table 3.4. The doping of smaller $Gd^{3+}$ ions are observed to compress the $BiFeO_3$ lattice. The average crystallite size of the nanoparticles was calculated using the Debye–Scherrer equation [196]. The values obtained are summarized in Table 3.4. It has been found that Gd-doping leads to remarkable reduction of the crystallite size and is well reflected in the broadened diffraction peak in Gd4 nanoparticles (Fig. 3.24 (b)). The reason may be attributed to the substitution of smaller $Gd^{3+}$ ions at larger Bi-site.

The variation of calcination temperature has been found to influence the XRD patterns. All the Gd-doped $BiFeO_3$ nanoparticles have been observed to possess the

orthorhombic phase. As XRD patterns of Gd4, Gd5 and Gd6 nanoparticles correspond to the orthorhombic phase of $GdFeO_3$ (JCPDS Card No 74-1477). The impurity phase detected in the XRD pattern of Gd4 nanoparticles has been observed to diminish with the increase in calcination temperature. The average crystallite size values (Table 3.4) of the Gd-doped $BiFeO_3$ nanoparticles indicate the decrease in crystallite size with calcination temperature, which is well reflected in the broadening of the peaks (Fig. 3.24 (a)).

### 3.5.2.2 Morphological analysis

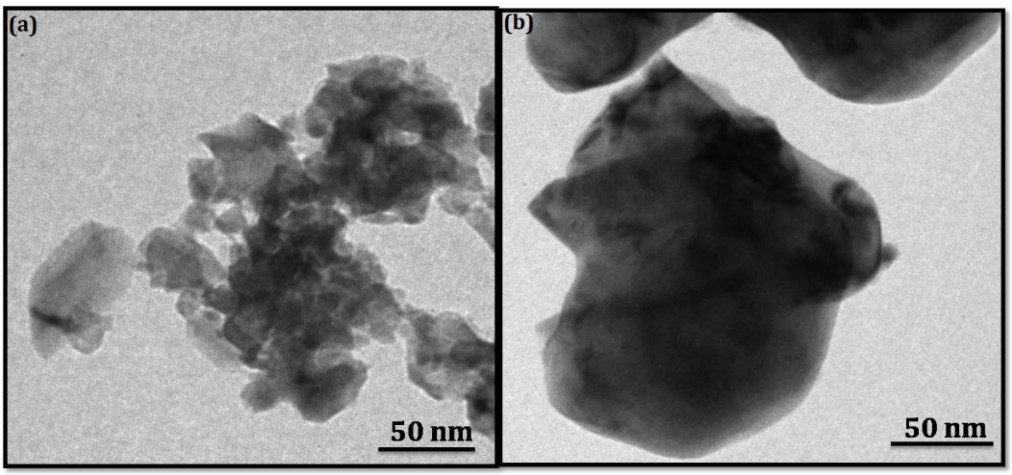


Fig. 3.25 TEM micrographs of (a) Gd4 and (b) Gd6 nanoparticles

Fig. 3.25 (a) and (b) represent TEM micrographs of Gd4 and Gd6 nanoparticles. The highly agglomerated nanoparticles of irregular morphology have been observed to form similar to previous reports [108, 130, 133]. The reason of agglomeration may be attributed to the high surface energy of nanoparticles [108]. The average particle size has been found out to be 16 and 150 nm, respectively, for Gd4 and Gd6 nanoparticles. Here the growth mechanism of nanoparticles formed by sol-gel has been found to take place via homogeneous nucleation [18]. The details of the mechanism are described in section 3.1.2.2.

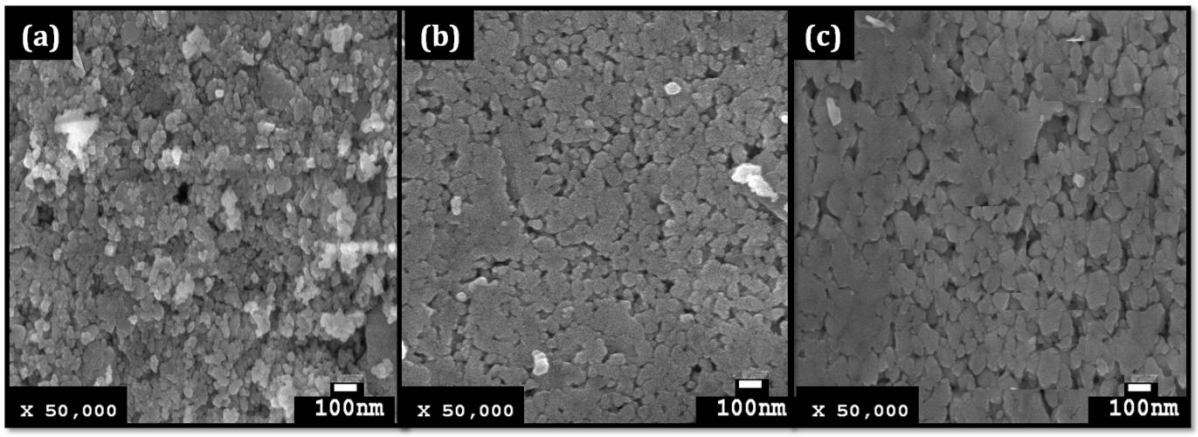


Fig. 3.26 FEG-SEM micrographs of (a) Gd4 (b) Gd5 and (c) Gd6 nanoparticles at 50k X

Fig. 3.26 illustrates the FEG-SEM micrographs of Gd4, Gd5 and Gd6 nanoparticles at 50k X (magnification) and 100 nm (scale). The microstructures have been found to possess uniformly distributed densely packed grains having well-defined boundaries, which reveal their crystalline nature. The morphology of all the nanoparticles has been observed to be almost spherical. On comparing the microstructures, the increase in grain size with calcination temperature has been observed. This indicates grain growth with temperature. The reason may be attributed to the coalescence of grains via grain boundaries with rise in temperature [197].

### 3.5.2.3 Magnetic analysis

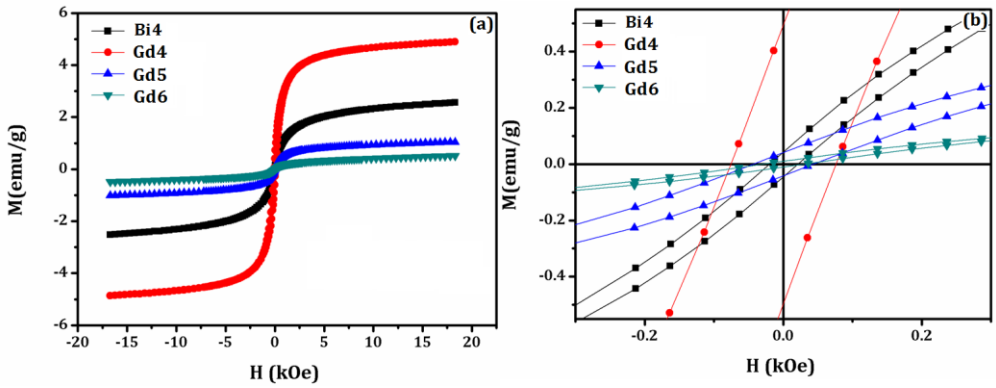


Fig. 3.27 (a) Room temperature magnetization hysteresis loops of Bi4, Gd4, Gd5, and Gd6 nanoparticles and (b) their enlarged views

Fig. 3.27 shows M-H loops of the synthesized nanoparticles. All the nanoparticles have been found to exhibit ferromagnetism. The impurity (revealed in XRD; Fig. 3.24) contribution, towards the observed magnetism, is ruled out as it doesn't exhibit room temperature ferromagnetism [208]. Undoped $BiFeO_3$ nanoparticles are found to possess ferromagnetism, contrary to its bulk counterpart (antiferromagnetic) [107]. Following are the attributed reasons [110]: (i) incomplete spin compensation between two spin sublattices in small antiferromagnetic nanoparticles leads to measurable magnetization, according to Néel's theory and (ii) at nanoscale the large surface to volume ratio enhances the contribution of uncompensated surface spin.

Various magnetic parameters obtained from the enlarged view of M-H curves (Fig. 3.27 (b)) are summarized in Table 3.4. Saturation magnetization value has been found to increase with Gd-doping in $BiFeO_3$ lattice (Table 3.4). The observation is similar to other rare earth doped-$BiFeO_3$ nanoparticles [129-133]. Gd-doping induces large lattice distortion owing to its smaller ionic radius (0.938 Å) as compared to $Bi^{3+}$ (1.17 Å), which in turn suppress the spin cycloid structure of $BiFeO_3$ and thus enhances the magnetization [129, 132]. Also, Guo and Liu et al observed enhanced magnetism due to the coupling of magnetically active rare earth ion ($Eu^{3+}$) with $Fe^{3+}$ by the first-principle calculations [132]. As $Gd^{3+}$ possesses quite high magnetic moment (8.0 $\mu_B$), its coupling with $Fe^{3+}$ ions leads to enhancement of ferromagnetism in the present system. Here, the $M_s$ value observed with Gd-doping is quite large as compared to the sol-gel synthesized Gd-doped $BiFeO_3$ nanoparticles reported by Guo et al. [132].

Saturation magnetization value has been found to increase with reduction in particle size (Table 3.4) - behavior typical for antiferromagnetic nanoparticles [133]. As surface to volume ratio increases with reducing particle size, the density of number of uncompensated

spins increases, which results in enhanced magnetization. Also, grain size confinement effect comes into play for particles below 62 nm [110]. It modulates the spin cycloid structure of $BiFeO_3$ and thus leads to strongly size-dependent magnetism.

In magnetoelectric material, the exchange bias mechanism allows the exploitation of coupling of antiferromagnetic and ferroelectric orders, for device application [198]. The exchange bias field ( $H_{eb}$ ) has been observed in the present system and is calculated using Eq. 3.4 [107]. Exchange bias results from exchange interactions between pinned uncompensated spins in antiferromagnetic core and moments in ferromagnetic surface [135]. The calculated $H_{eb}$ values are shown in Table 3.4. It has been found to tune with variation in particle size. It enhances with reduction in particle size. The reason is attributed to the decrease in the density of uncompensated spins on the particle surface with size [107]. It is well in agreement with the Néel's modelling of the synthesized samples. This observation indicates that in the present system oxygen vacancies increase with calcination temperature. As the unstable charge configuration of $Fe^{2+}$ require generation of oxygen vacancies and hence decrease the uncompensated spins, which in turn decrease the exchange bias.

Also, the presence of $M_{shift}$ along with horizontal sift has been observed in the magnetic hysteresis curves. It has been calculated using Eq. 3.5 [199]. The rarely found $M_{shift}$ is indicative of the uncompensated spins at the ferromagnetic-antiferromagnet interface. It has been found to be influenced by variation in particle size. Both $H_{eb}$ and $M_{shift}$ have been observed to follow the same trend i.e. increase with decrease in particle size (Table 3.4). Thus, particle size plays a significant role in deciding the various magnetic parameters ($M_s$, $H_{eb}$ and $M_{shift}$).

Table 3.4 Structural, magnetic and electric parameters of Bi4, Gd4, Gd5 and Gd6 nanoparticles

| Sample | Structural parameters | | | | | Magnetic parameters | | | Electric parameters | | | | |
|---|---|---|---|---|---|---|---|---|---|---|---|---|---|
| | D nm | a Å | b Å | c Å | V $Å^3$ | $M_s$ emu/g | $H_{eb}$ Oe | $M_{shift}$ emu/g | $\varepsilon$ Loss @0.1 kHz | | $P_s$ μC/$cm^2$ | $P_r$ μC/$cm^2$ | $E_c$ kV/cm |
| Bi4 | 21.2 | 5.56 | 5.56 | 13.9 | 429.6 | 2.5 | 1.1 | 0.005 | 690 | 0.34 | 2.6 | 2.1 | 9.1 |
| Gd4 | 9.2 | 5.60 | 5.59 | 7.8 | 244.2 | 4.9 | 3.2 | 0.002 | 2193 | 0.32 | 8.4 | 7.0 | 13.3 |
| Gd5 | 16.2 | 5.53 | 5.54 | 7.6 | 232.8 | 1.1 | 1.0 | 0.001 | 777 | 1.3 | 7.1 | 6.2 | 13.4 |
| Gd6 | 20.1 | 5.51 | 5.36 | 8.1 | 239.2 | 0.6 | 0.5 | 6E-4 | 546 | 1.8 | 5.1 | 4.3 | 8.2 |

### 3.5.2.4 Electrical analysis

#### 3.5.2.4.1 Dielectric analysis

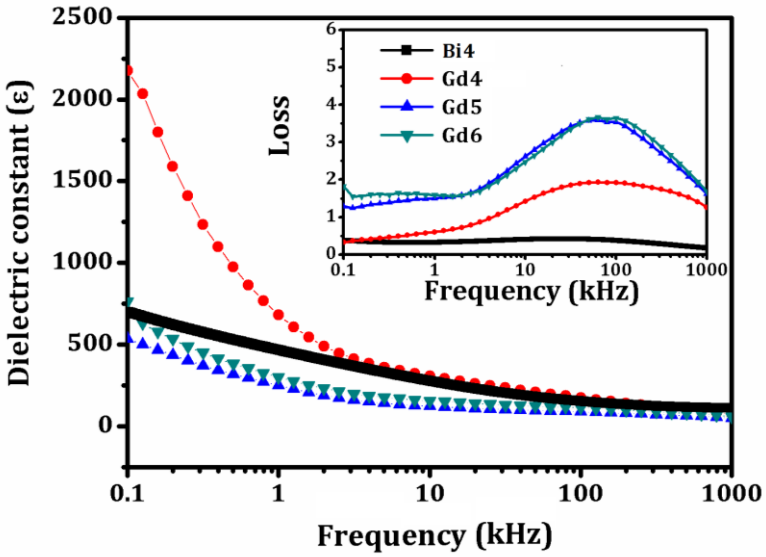


Fig. 3.28 Room temperature frequency response of dielectric constant and loss (Inset) of synthesized nanoparticles in the range 0.1-1000 kHz

Fig. 3.28 illustrates frequency response of dielectric constant and dielectric loss of synthesized nanoparticles in the range 0.1-1000 kHz. The dielectric behaviour has been observed to show dispersive behaviour, which approves the presence of space charges [137]. The observation can be explained by the dipole relaxation phenomenon where the space charges are able to follow the lower frequencies of the applied field however fail to do so at higher frequencies [133]. These space charges are trapped by the grains, defects of nanoparticles at the interfaces, lattice distortions, and oxygen and bismuth vacancies [152]. Moreover, dielectric constant is dependent on different kinds of polarization (electronic, interfacial, atomic, and ionic etc) at low frequency but at higher frequencies only electronic polarization contributes thereby resulting in its decrease [202].

All the synthesized nanoparticles have been found to display Debye-type relaxation [137]. The various dielectric parameters are summarized in Table 3.4. It has been observed that Gd-doping enhances the dielectric constant value owing to the rhombohedral lattice distortion by substitution of smaller $Gd^{3+}$ ion (0.938 Å) at larger $Bi^{3+}$ ion (1.17 Å) [76-77]. It results in orthorhombic phase formation, which being less centrosymmetric crystal structure gives rise to more polar displacements and thus, higher dielectric constant value [149]. The dielectric loss (inset Fig. 3.28) has been found to decrease with Gd-doping (Table 3.4). This result indicates that $Gd^{3+}$ ions improve the dielectric properties of $BiFeO_3$. The substitution of smaller $Gd^{3+}$ ions (0.938 Å) at A-site decreases the average ionic radius of A-site and decreases Fe–O–Fe bond angle (θ). The smaller θ lowers the electronic bandwidth, which, in turn, increases the charge-transfer gap between oxygen 2p valence band and Fe 3d conduction band, which allows slow transfer of the charge carriers [152]. Moreover, the rare earth metal ions substitution strengthens random as well as Coulomb potential, which further strengthens the localization degree of $Fe^{3+}$ and enhances the resistivity [152].

Further, particle size significantly influences the dielectric properties of Gd-doped $BiFeO_3$ nanoparticles (Table 3.4). It has been observed that the dielectric constant decreases with increase in particle size. The reason may be attributed to the nanosized grains present in the synthesized nanoparticles as revealed by FEG-SEM (Fig. 3.26) [130]. These act as large insulating barriers to mobile charge carriers, which thus result in reduced conductivity in the system [130]. Here, FEG-SEM micrographs reveal decreasing grain size with calcination temperature. Hence, smaller the grain size better is the insulation consequently higher the dielectric constant. The polycrystalline nanoparticles have large grain boundary region. Grain and grain boundary regions are crucial in deciding the electrical properties as the inhomogenity amongst them reduces the mobility of charge carriers [202].

A decrease in dielectric loss (energy dissipation in the dielectric system) has been observed with particle size (Table 3.4) indicating increased resistivity provided by the smaller nano-sized grains as described above. The resonance observed in loss spectra indicates correlation of dielectric polarization of the sample and conduction mechanism [133]. The peak appears when the hoping frequency matches with that of applied external electric field.

### 3.5.2.4.2 Ferroelectric analysis

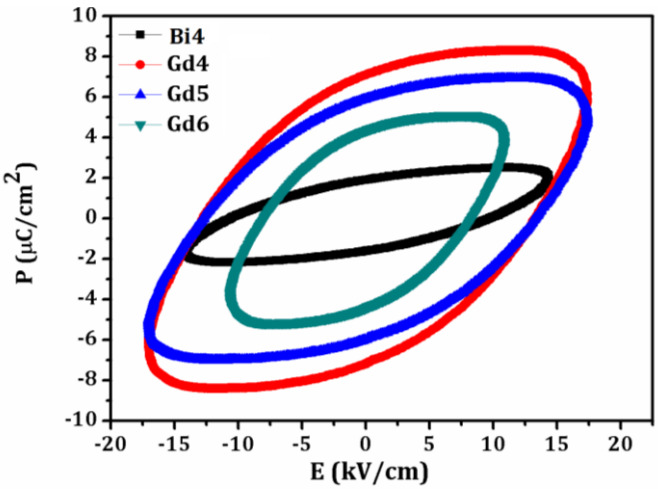


Fig. 3.29 Ferroelectric hysteresis loops of Bi4, Gd4, Gd5 and Gd6 nanoparticles at room temperature

Fig. 3.29 shows room temperature P-E hysteresis loops of the synthesized nanoparticles at frequency of 100 Hz. Table 3.4 summarizes various polarization parameters. Undpoed $BiFeO_3$ nanoparticles have been found to exhibit weak polarization. Bulk $BiFeO_3$ is reported to show poor ferroelectric behaviour due to non-stoichiometric issues, oxygen vacancies and space charge defects arising due to high volatility of $BiFeO_3$ [150]. Undoped $BiFeO_3$ nanoparticles have been found to exhibit better ferroelectric behaviour. The improved ferroelectric behaviour may be owed to increased density of the pellet in nano regime that reduces the current conduction [134]. The polarization values (Table 3.4) have been found to enhance in all the Gd-doped $BiFeO_3$ nanoparticles, thereby indicating improved polarization values. Three reasons may be attributed to this behaviour: (i) The substitution of $Gd^{3+}$ ions at $Bi^{3+}$ ion site reduces the said issues as the energy required to dissociate the rare-earth metal ions-oxygen (Gd-O) bond is higher than the Bi-O bond [150]. The reduced defects in turn lower the leakage current that results in polarization, (ii) Grain and grain boundaries also influence the leakage current. Gd-doping has been found to reduce the grain size and smaller grains provide insulation barrier to the conductivity by charge carrier [133, 202] and (iii) The rhombohedral structural distortion of $BiFeO_3$ by $Gd^{3+}$ ions into orthorhombic due to mismatch between their ionic radii also leads to the enhancement of ferroelectricity as the later structure is less centrosymmetric [150].

Varying particle size has significantly influenced the ferroelectric behaviour of Gd-doped $BiFeO_3$ nanoparticles. The spontaneous polarization and the applied electric field values have been found to enhance with reduction in particle size. The reason may be attributed to the nano-sized grains [130]. The smaller the grain size better is the obstruction to the charge carriers, which in turn increases the insulation of the nanoparticles having smaller grain size giving rise to increasing saturation polarization values.

# *Chapter 4*

# *ALKALINE EARTH METAL IONS*

# *DOPED-$BiFeO_3$*

# *NANOPARTICLES*

# Chapter 4

The present chapter deals with the experimental procedures employed for synthesizing the alkaline earth doped $BiFeO_3$ nanoparticles and varying their particle size. Their structural, morphological, magnetic, dielectric and ferroelectric properties have been discussed.

Following is the communication corresponding to alkaline earth doped $BiFeO_3$ nanoparticles. Some of the results have been discussed in this chapter.

1. Gitanjali Dhir, Poonam Uniyal, N. K. Verma, 'Effect of particle size on multiferroism of barium-doped bismuth ferrite nanoparticles', Mater. Sci. in Semicond. Process. 27 (2014) 611–61.
2. Gitanjali Dhir, Poonam Uniyal, N. K. Verma, 'Sol-gel synthesized Sr-doped $BiFeO_3$ nanoparticles : Enhanced multiferroic properties with reduced particle size', Mater. Sci. in Semicond. Process. (Under review with minor revisions).

## 4.1 Ca-doped $BiFeO_3$ nanoparticles ($Bi_{1-x}Ca_xFeO_3$; x = 0, 0.15)

### 4.1.1 Synthesis

The procedure followed for the synthesis of undoped and Ca-doped $BiFeO_3$ (x = 0.15) nanoparticles is same as described in section (3.2.1). The undoped $BiFeO_3$ nanoparticles were obtained by calcination at 450 $^0$C (U4) for 4 hour. Nanoparticles of Ca-doped $BiFeO_3$ of different sizes have been obtained by the calcination at different temperatures viz., 450 $^0$C (Ca4), 550 $^0$C (Ca5) and 650 $^0$C (Ca6) for 4 hour.

### 4.1.2 Results and discussion

#### 4.1.2.1 Structural and phase analyses

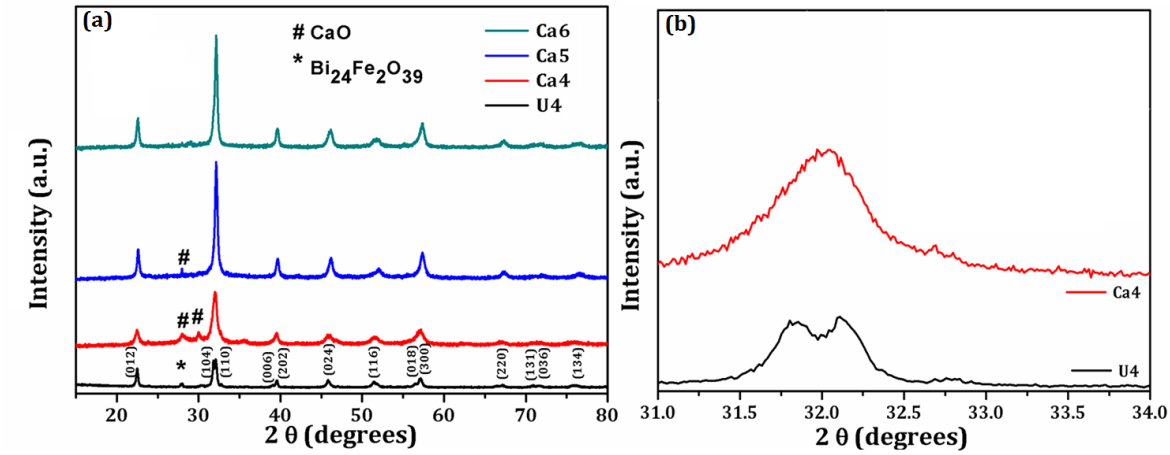


Fig.4.1 (a) XRD patterns of U4, Ca4, Ca5 and Ca6 nanoparticles and (b) enlarged patterns of U4 and Ca4 nanoparticles

The phase formation and structural analysis was carried out using XRD. Fig. 4.1 (a) shows XRD patterns of U4, Ca4, Ca5 and Ca6 nanoparticles. All the diffraction peaks of undoped $BiFeO_3$ characterize rhombohedral structure having $R_{3c}$ space group (JCPDS Card No. 86-1518). Minute traces of impurity denoted by * and # (Fig. 4.1 (a)) correspond to $Bi_{24}Fe_2O_{39}$ (JCPDS Card No. 42-0201) and CaO (JCPDS Card No. 28-0775), respectively.

Ca-doping in $BiFeO_3$ has been observed to show two features. One is that the twin peaks (104) and (110) merge on doping $Ca^{2+}$ ions in $BiFeO_3$ nanoparticles (enlarged view at around $2\theta \sim 32^{o}$; Fig. 4.1(b)) to form a single peak in Ca-doped samples. It indicates induction of structural transformation from rhomboheral to orthorhombic phase by $Ca^{2+}$ ions [129]. Second feature is that the merged peak is further shifted towards higher $2\theta$, which is attributed to the substitution of smaller $Ca^{2+}$ (1.00 Å) ions in the place of larger $Bi^{3+}$ (1.17 Å) ions [137]. The various structural parameters are summarized in Table 4.1. Ca-doping has

been found to contract the lattice as it reduces the volume. The analysis of varying calcination temperature effects on the crystal structure has also been done with the help of XRD data. The crystallite size values (Table 4.1) calculated using Debye-Scherrer equation has been found to increase with calcination temperature [196]. The diffraction peaks have been found to sharpen with enhancement in calcination temperature. This indicates the increase of crystallinity. The average crystallite size values summarized in Table 4.1, point towards remarkable reduction of the crystallite size by Ca-doping, which is also illustrated by the relatively broadened diffraction peaks of Ca-doped $BiFeO_3$ nanoparticles as compared to undoped $BiFeO_3$ nanoparticles (Fig. 4.1(b)). This is due to the substitution of comparatively smaller $Ca^{2+}$ ions in place of larger $Bi^{3+}$ ions [137].

### 4.1.2.2 Morphological analysis

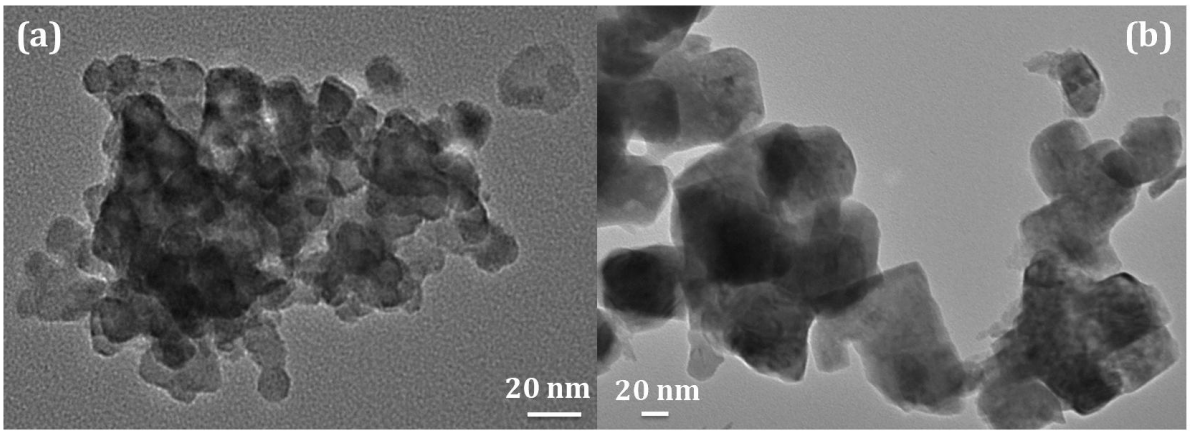


Fig. 4.2 TEM micrographs of (a) Ca4 and (b) Ca6 nanoparticles

To see the calcination temperature dependence on shape and size of nanoparticles, TEM has been employed. The topographical analysis reveals high agglomeration; it is precisely due to nanoparticles' high surface energy [108].

The nanoparticles exhibit almost spherical morphology (Fig. 4.2 (a)) at lower calcination temperature (450°C; Ca4) but these, when exposed to higher calcination temperature (650°C; Ca6), agglomerate irregularly (Fig. 4.2 (b)). The average particle size has been found out to be 11 and 53 nm, respectively, for Ca4 and Ca6 nanoparticles.

Nanoparticles of almost spherical morphology at lower calcination temperature (Ca4) tend to merge asymmetrically to form bigger particles (Ca6). Many phenomena are attributed to growth of nanoparticles [18]. Here the growth mechanism of nanoparticles formed by sol-gel can be explained by thermodynamic homogeneous nucleation given in section 3.1.2.2.

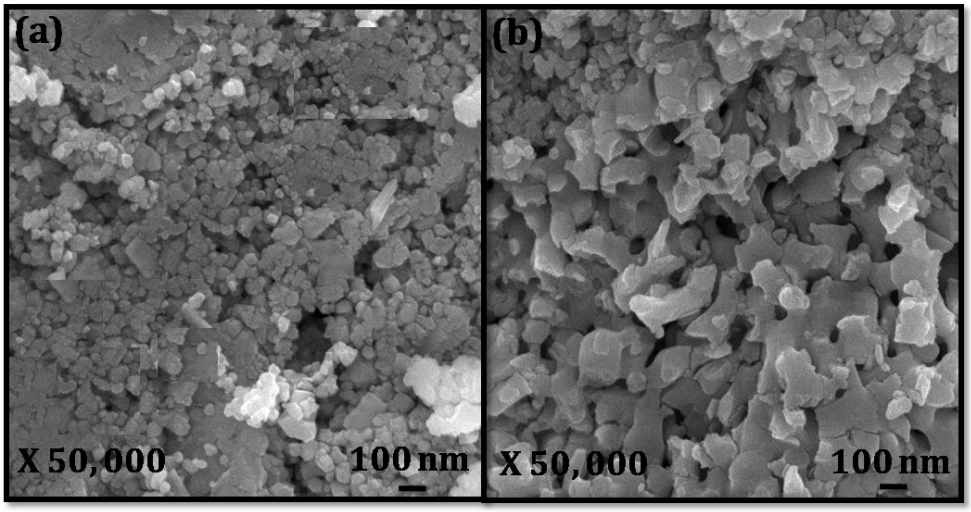


Fig. 4.3 FEG-SEM micrographs of (a) Ca4 and (b) Ca6 nanoparticles at 50k X

A comparative illustration at length scale of 100 nm and magnification of 50k X presented in Fig. 4.3 reveals increasing grain size with calcination temperature. Coalescence of grains via grain boundaries takes place with increasing temperature, which results in growth [197]. The morphological analysis reveals uniform distribution of almost spherical grains, which are densely packed and have well-defined boundaries. This indicates their crystalline nature.

### 4.1.2.3 Magnetic analysis

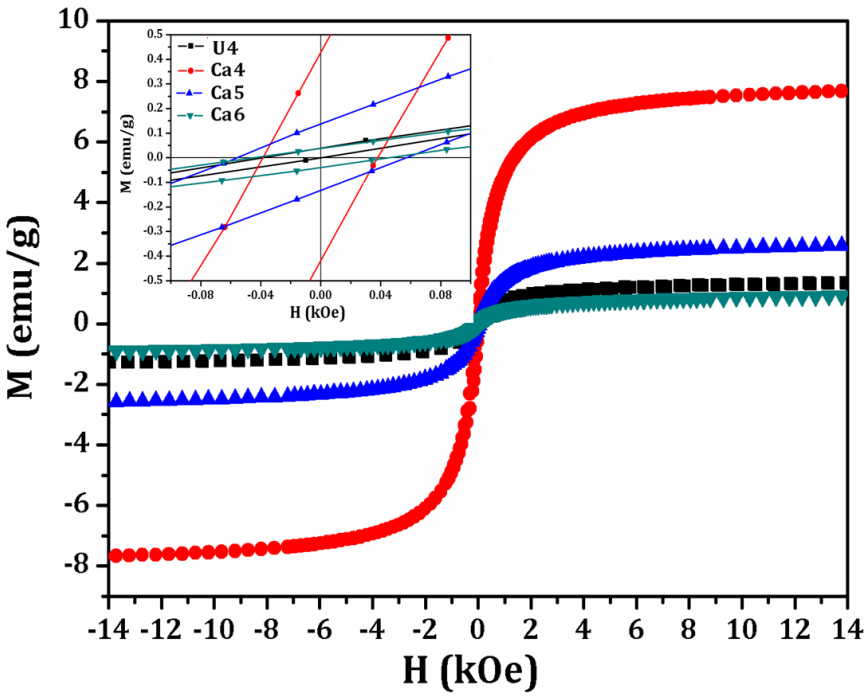


Fig. 4.4 Room temperature magnetization hysteresis loops of U4, Ca4, Ca5 and Ca6 nanoparticles. The inset shows their enlarged views

Fig. 4.4 shows room temperature M-H loops of synthesized nanoparticles and the magnetic parameters obtained are given in Table 4.1. All the loops have been found to display ferromagnetism. The contribution of minute traces of impurities (observed in XRD; Fig. 4.1 (a)) towards observed magnetic behavior is ruled out as these do not exhibit room temperature magnetism [209]. Undoped $BiFeO_3$ has been found to display ferromagnetism in contrast to its bulk counterpart, which is antiferromagnetic [92]. Three possible reasons may be attributed to this behaviour. Firstly, small antiferromagnetic nanoparticles possess measurable magnetic moment [110]. An antiferromagnet consists of spin sublattices, which have intra ferromagnetic and inter antiferromagnetic interactions. According to Néel's theory, incomplete spin compensation between sublattices results in magnetic moment as, the antiferromagnetic order gets interrupted at the particle's surface in small

antiferromagnetically ordered systems [152]. Secondly, the large surface to volume ratio raises the number of uncompensated spins at the particle's surface contributing towards enhancement of overall magnetization.

Magnetic parameters obtained from the enlarged view of hysteresis loops (inset Fig. 4.4) have been summarized in Table 4.1. Enhancement in saturation magnetization value has been observed with the Ca-doping. Three reasons may be attributed to it: (i) substitution-induced distortion of rhombohedral lattice [132], (ii) suppression of spin spiral structure of $BiFeO_3$ due to reduction in particle size (TEM) and (iii) the divalent ($Ca^{2+}$) ion substitution at trivalent ($Bi^{3+}$) site creating oxygen vacancies, which result in destabilization of the system due to charge imbalance [137-138]. Subsequently, two alkaline earth metal ions create one oxygen vacancy to keep the system neutral. These oxygen vacancies suppress spiral spin structure, and, thus, increase ferromagnetism.

Remarkable impact of particle size on magnetic parameters has been observed (Table 4.1). $M_s$ increases as the particle size decreases (Table 4.1). The increasing surface to volume ratio with decreasing particle size increases the contribution of uncompensated magnetic spins and thus enhances the magnetization [110]. The grain size confinement effect comes into play for particles having dimensions below 62 nm due to which the spin spiral structure of $BiFeO_3$ gets modulated and results in strong size dependence of magnetism [110].

The exploitation of magnetoelectric coupling in a material, with antiferromagentic and ferroelectric orders, for practical application is possible by exchange bias mechanism as it allows electric field control of magnetization [198]. So, its presence was investigated in the present system and it has been found that exchange interaction between pinned uncompensated spins in antiferromagnetic core and moments in ferromagnetic surface results

in exchange bias [135]. The exchange bias field ($H_{eb}$) values [107] are calculated using Eq. 3.4. Particle size variation has resulted in tuning of exchange bias in the Ca-doped $BiFeO_3$ system. It has been observed to increase with reducing size (Table 4.1). It may be owed to the lowering density of uncompensated spins with the decreasing particle surface area, which is consistent with the explanation done using Néel's modelling.

In addition to horizontal, the presence of rarely observed vertical shift ($M_{shift}$) has been revealed by the M-H loops, which has been calculated using Eq. 3.5. It is indicative of uncompensated spins at the ferromagnetic-antiferromagnet interface [199]. The intriguing $M_{shift}$ varies with particle size and follows the same trend as $H_{eb}$ (Table 4.1). Thus, particle size has a vital role.

Table 4.1 Structural, magnetic and electric parameters of U4, Ca4, Ca5 and Ca6 nanoparticles

| Sample | Structural parameters | | | | Magnetic parameters | | | Electric parameters | | | | |
|---|---|---|---|---|---|---|---|---|---|---|---|---|
| | D nm | a Å | c Å | V $Å^3$ | $M_s$ emu/g | $H_{eb}$ Oe | $M_{shift}$ emu/g | $\varepsilon$ Loss @ 0.1 kHz | | $P_s$ $\mu C/cm^2$ | $P_r$ $\mu C/cm^2$ | $E_c$ kV/cm |
| U4 | 15.0 | 5.57 | 13.89 | 373.13 | 1.29 | 17.4 | 0.017 | 733 | 0.3 | 2.02 | 1.43 | 4.07 |
| Ca4 | 10.4 | 5.58 | 13.77 | 372.05 | 7.68 | 0.40 | 0.005 | 1678 | 3.6 | 3.32 | 2.50 | 3.47 |
| Ca5 | 20.6 | 5.54 | 13.60 | 362.74 | 2.58 | 0.38 | 0.003 | 642 | 1.3 | 0.48 | 0.50 | 5.85 |
| Ca6 | 21.3 | 5.56 | 13.65 | 365.76 | 0.91 | 0.25 | 8.4E-4 | 474 | 1.7 | 0.61 | 0.36 | 5.61 |

### 4.1.2.4 Electrical analysis

#### 4.1.2.4.1 Dielectric analysis

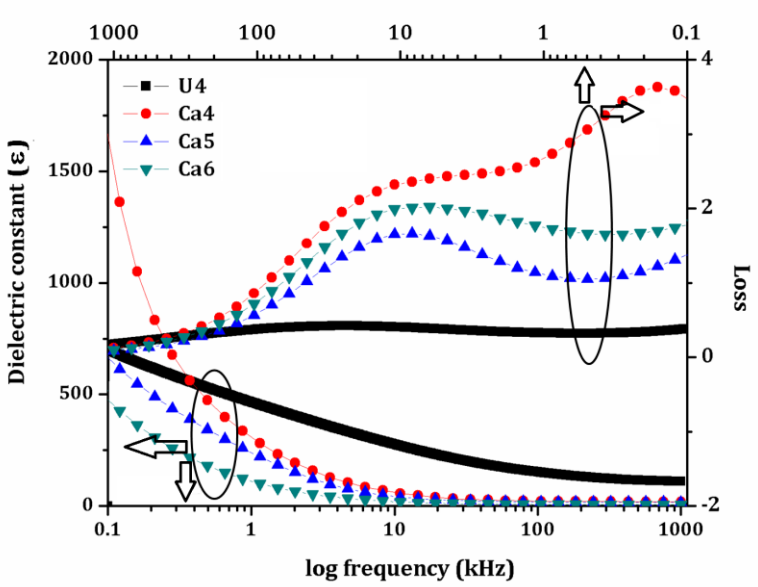


Fig. 4.5 Room temperature frequency response of dielectric constant and dielectric loss of synthesized nanoparticles in the range 0.1-1000 kHz

Fig. 4.5 illustrates the frequency dependence of dielectric constant and loss (tan δ) in the range 0.1 – 1000 kHz. The dispersions observed in the dielectric behaviour unveil the presence of space charges. In $BiFeO_3$, oxygen and bismuth vacancies, lattice distortions and defects act as sources of space charges [156]. These space charges are able to follow the applied electric field at lower frequencies but unable to do so at higher frequencies, subsequently, the dielectric constant decreases at higher frequencies. Also, various polarizations (electronic, atomic, ionic and interfacial) contribute towards dielectric constant. However, only electronic polarization contributes towards dielectric constant at higher frequencies thereby, resulting in its decrease [76].

The synthesized nanoparticles have been found to exhibit Debye-type relaxation [137]. Table 4.1 summarizes the dielectric parameters. Ca-doping has been observed to enhance the dielectric constant value. The reason may be attributed to the rhombohedral distortion of the $BiFeO_3$ lattice induced by Ca-doping, which forms orthorhombic phase. This being less centrosymmetric allows more polar displacements and hence, the enhanced dielectric constant value [149]. However, high loss value has been also observed with Ca-doping. The defect chemistry corresponds to the creation of oxygen vacancies for charge maintenance owing to the substitution of divalent ions ($Ca^{2+}$) at the trivalent ($Bi^{3+}$) site [137-138]. Since oxygen vacancies are well-known sources for inducing conductivity in the system loss has been observed to increase [150].

The particle size has a crucial role in deciding the dielectric properties of Ca-doped $BiFeO_3$ nanoparticles (Table 4.1). The dielectric constant has been found to decrease with increasing particle size. The reason is owed to the presence of nanosized grains (FEG-SEM) [130]. These provide large insulating barriers to mobile charge carriers thereby, resulting in decreasing the conductivity of the system [152]. FEG-SEM micrographs reveal increasing grain size with calcination temperature, thus consequently, the dielectric constant decreases. Ca-doping has also resulted in reduction of the crystallite size as well, which, also attributes to its enhanced dielectric constant value.

### 4.1.2.4.2 Ferroelectric analysis

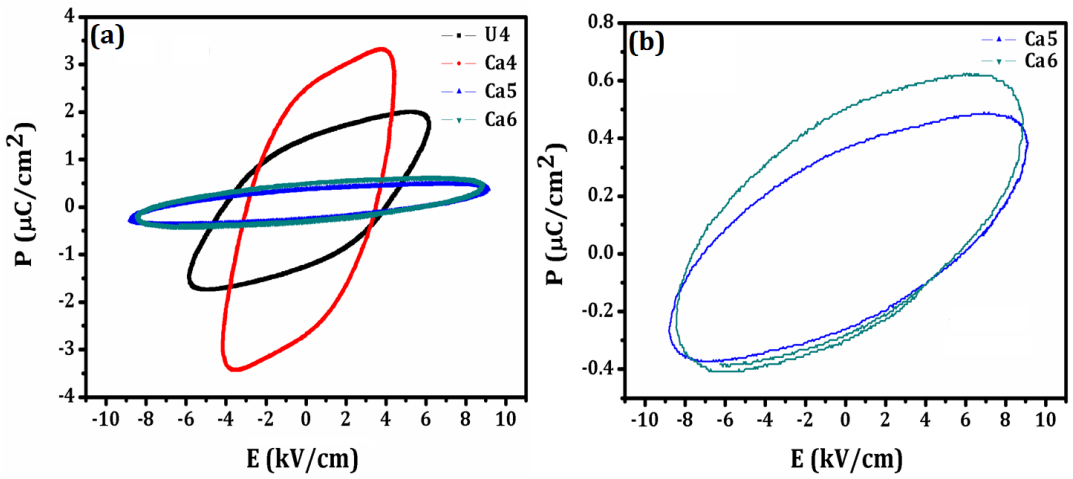


Fig. 4.6 Room temperature ferroelectric hysteresis (P-E) loops of (a) U4, Ca4, Ca5 and Ca6 nanoparticles and (b) the P-E loops of Ca5 and Ca6 nanoparticles

Room temperature ferroelectric behavior of the synthesized nanoparticles was analysed at frequency of 100 Hz, as shown in Fig. 4.6. Various electric hysteresis parameters obtained from P-E loops are summarized in Table 4.1. In $BiFeO_3$, polarization arises from the displacement of $6s^2$ electron lone pair of Bi with respect to $FeO_6$ octahedra [210]. Literature reveals poor ferroelectric behaviour for bulk $BiFeO_3$ owing to non-stoichiometric issues, secondary phases due to volatile nature of Bi as well as are the oxygen vacancies originating because of the unstable Fe (variable oxidation state $Fe^{2+}$, $Fe^{3+}$) [150]. However, reduction of size to nanoscale has been observed to improve the ferroelectricity of $BiFeO_3$ as it suppresses the secondary phase formation. Another possible reason may be that the bulk samples possess porosity, which enhances current conduction. However, the samples at the nano-regime become denser resulting in reduced leakage current and consequently giving rise to regular electric hysteresis loop [211]. Ca-doping has been observed to enhance the spontaneous polarization (Table 4.1) owing to the rhombohedral lattice distortion induced by it [76-77]

and reduction in grain size (FEG SEM; Fig. 4.3) [130, 134]. However, a well saturated polarization loop has not been observed; it is so because the divalent $Ca^{2+}$ ions substitution leads to the generation of oxygen vacancies in $BiFeO_3$ lattice that degrades the polarization [137].

Effect of particle size on the ferroelectric behaviour of Ca-doped $BiFeO_3$ nanoparticles has also been investigated. It has been observed that ferroelectricity deteriorates with increasing particle size. It can be understood from the role of grain and grain boundaries contribution towards the electric properties in nanoparticles. The inhomogenity in the grain and grain boundaries enhances the insulation of the system [133]. The synthesized nanoparticles consist of nano-sized grains and these acts as an insulating barrier for the charge carriers [130]. Smaller the grain size better is the obstruction of charge carriers. Thus, the spontaneous polarization value has been found to decrease with the increase in particle size. The coercive field has been found to enhance with the particle size. Two possible reasons may be owed [212] to it: (i) resistance to the off-centre displacement of $Ca^{2+}$ ions with respect to $FeO_6$ octahedra resulting in prevention of polarization reversal and enhancing the coercivity and (ii) the space charge defects (mainly oxygen vacancies) resulting from increasing particle size that subsequently enhance the coercivity.

## 4.2 Sr-doped $BiFeO_3$ nanoparticles ($Bi_{1-x}Sr_xFeO_3$; x= 0, 0.15)

### 4.2.1 Synthesis

The synthesis of $Bi_{1-x}Sr_xFeO_3$ (x = 0.15) nanoparticles was carried out via sol-gel method same as described in section (3.2.1). $BiFeO_3$ nanoparticles were acquired by calcining at $450^0$C (B4). 15% Sr-doped $BiFeO_3$ nanoparticles of different sizes were then obtained by the calcination at different temperatures viz., 450 $^0$C (Sr4), 550 $^0$C (Sr5) and 650 $^0$C (Sr6) for 4 hour.

### 4.2.2 Results and discussion

#### 4.2.2.1 Structural and phase analyses

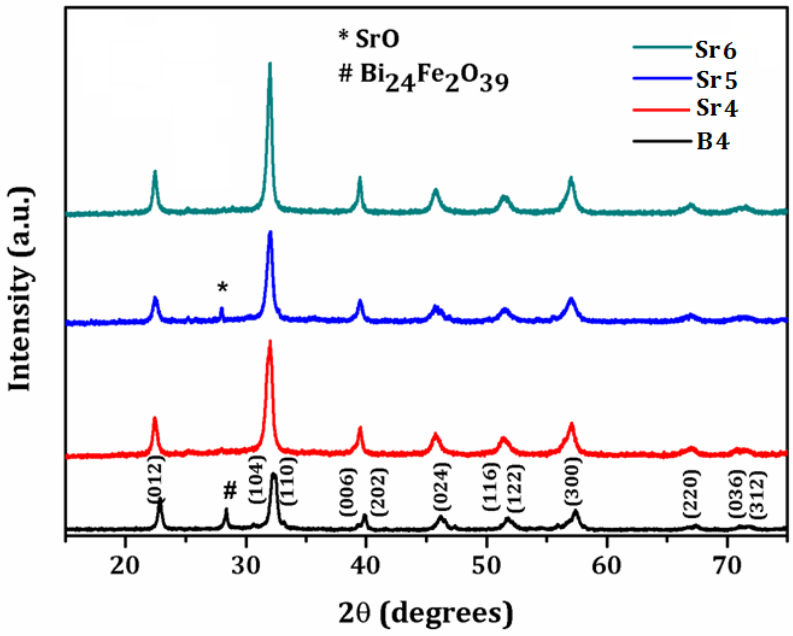


Fig. 4.7 XRD patterns of B4, Sr4, Sr5 and Sr6 nanoparticles at room temperature

The XRD patterns of the synthesized nanoparticles are shown in Fig. 4.7. From the diffraction patterns it has been observed that undoped $BiFeO_3$ nanoparticles could be indexed to rhombohedral structure having space group $R_{3c}$ using the standard crystal data (JCPDS Card No. 86-1518). Traces of impurities denoted by # and * (Fig. 4.7) correspond to $Bi_{24}Fe_2O_{39}$ (JCPDS Card No. 42-0201) and SrO (JCPDS Card No. 27-1304), respectively. Due to kinetics of formation some impurity phase are always formed during the synthesis [71].

Sr-doping in $BiFeO_3$ has not been found to affect the lattice symmetry. The various structural parameters of the synthesized nanoparticles have been listed in Table 4.2. Sr-doping has been found to reduce the crystallite size, which could be attributed to the

inhibition of the grain growth by $Sr^{2+}$ ions [138]. Varying calcination temperature has been found to affect the diffraction patterns. Scherrer formula indicates an increase in crystallite size values (Table 4.2) with calcination temperature. However, the lattice symmetry has been found to be consistent with varying calcination temperature. Variation in particle size has been observed to influence the lattice parameters. The unit cell volume increases with reduction in crystallite size, which is typical for partly covalent oxides [108].

### 4.2.2.2 Morphological analysis

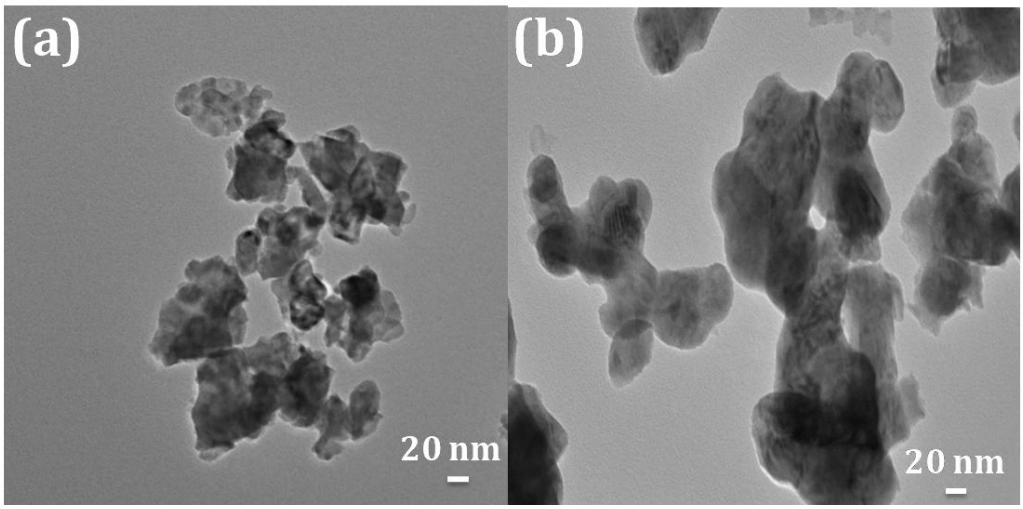


Fig. 4.8 TEM micrographs of (a) Sr4 (b) Sr6 nanoparticles

The topographical analysis has been carried out using TEM. Agglomerated nanoparticles have been formed as observed in Fig. 4.8. Similar observation due to the high surface energy of the nanoparticles has been reported previously [108]. Agglomeration has been observed to decrease as the particle size increases. Nanoparticles of almost spherical morphology at lower calcination temperature (Sr4) tend to merge asymmetrically to form bigger particles (Sr6). The average particle size has been found to be 16, and 50 nm, respectively, for Sr4 and Sr6 nanoparticles. Many phenomena (Ostwald ripening, kinetically controlled, homogeneous nucleation) are attributed to explain the growth of nanoparticles

[153]. For the present synthesized nanoparticles by sol-gel method, the growth mechanism is described by homogeneous nucleation explained as in section 3.1.2.2.

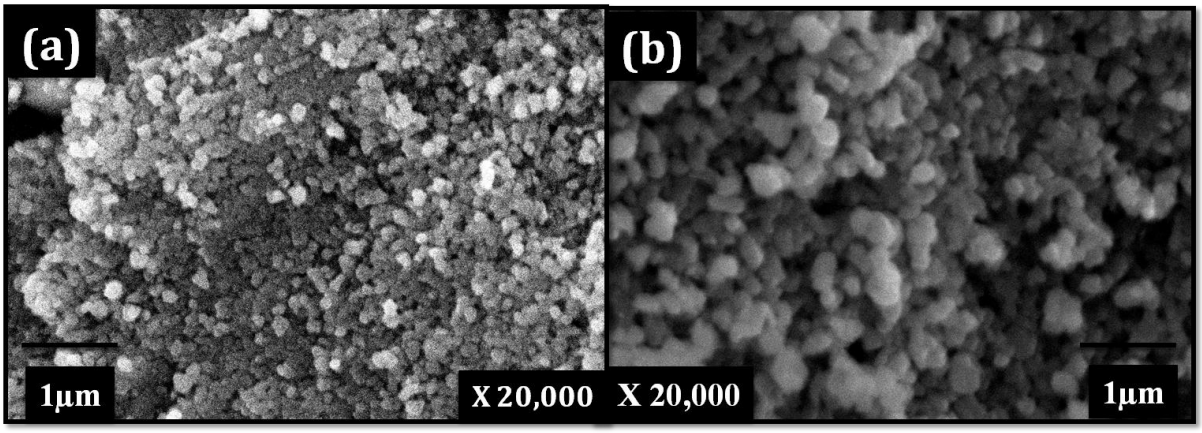


Fig. 4.9 FEG-SEM micrographs of (a) Sr4 and (d) Sr6 nanoparticles at 20k X

A comparative demonstration of variation in microstructure at 20k X and length scale of 1 µm is presented in Fig. 4.9. The micrographs are observed to possess uniformly distributed and densely packed grains having well-defined boundaries, which indicate their crystalline nature. The morphology of the nanoparticles is almost spherical.

### 4.2.2.3 Magnetic analysis

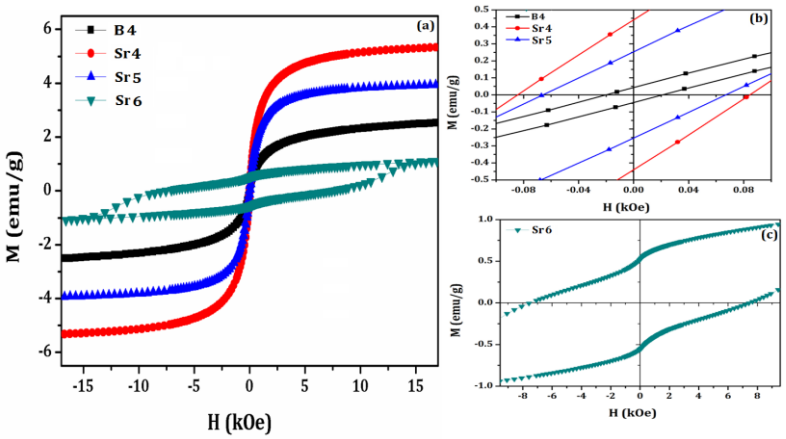


Fig. 4.10 (a) Room temperature magnetization hysteresis loops of B4, Sr4, Sr5 and Sr6 nanoparticles and the enlarged views of (b) B4, Sr4, Sr5 and (c) Sr6

Fig. 4.10 illustrates magnetic curves of the synthesized nanoparticles. The impurity phase does not contribute towards observed magnetic behaviour as these do not exhibit room temperature ferromagnetism [209]. Various magnetic parameters calculated from the enlarged magnetic curves (Fig. 4.10 (b, c)) are summarized in Table 4.2. All the synthesized nanoparticles have been found to exhibit ferromagnetism. Bulk $BiFeO_3$ is antiferromagnetic [147]. However, in nano regime it displays magnetism [107]. The antiferromagnetic nanoparticles possess incomplete spin compensation between sublattices due to ferromagnetic interactions within the sublattice however, antiferromagnetic interactions between the sublattices [110]. The incomplete spin compensation becomes considerable in small antiferromagnetic nanoparticles as the antiferromagnetic order gets interrupted at the particle's surface. This leads to net magnetization owing to incomplete spin compensation between sublattices, according to Néel's theory [152]. The large surface to volume ratio enhances the number of uncompensated spins present at the surface of nanoparticles thereby resulting in their enhanced contribution towards magnetization.

Sr-doping has enhanced saturation magnetization value (Table 4.2). Two reasons may be attributed to it: (i) the reduction in particle size resulting in suppression of spin cycloidal structure (below 62 nm, as revealed by the TEM image) [110] and (ii) $Sr^{2+}$ ions (divalent), when substituted at trivalent ($Bi^{3+}$ ions) sites, creates one oxygen vacancy for every two alkaline earth metal ions due to charge imbalance and thus suppressing spiral spin structure, and, enhancing magnetization [138].

$M_s$ increases with reduction in particle size (Table 4.2) owing to increasing surface to volume ratio, which enhances the number of uncompensated spins participating towards magnetism [132, 202]. The grain size confinement effect modulates the spin cycloid structure for particles below 62 nm thereby making magnetism strongly size-dependent [110]. With the

reduction in particle size enhanced strain of the nanoparticles leads to coordination distortion as well as lattice disorder, which is confined not only to the surface alone but to the whole particle thereby results in creation of different frustrated spin structure [110].

Enlarged magnetic hysteresis loops are observed to show both horizontal and vertical asymmetry (Fig. 4.10 (b) and (c)). These corroborate well with the observed ferromagnetism in the synthesized nanoparticles. $H_{eb}$ and $M_{shift}$ stand for exchange interactions between pinned uncompensated spins in antiferromagnetic core and moments in ferromagnetic surface [107, 199]. The exchange bias field and vertical shift (Table 4.2) for the synthesized nanoparticles has been calculated using Eq. 3.4 and 3.5, respectively. The presence of finite coercivity as well as exchange bias field rules out the possibility of superparamagnetism. Also, it confirms the ferromagnetism and pinning of spins at the ferromagnetic-antiferromagnetic interfaces [107]. This further supports the Néel's modelling of the magnetization of synthesized nanoparticles. The room temperature coercivity is of high interest from application point of view. $M_{shift}$ is indicative of uncompensated spins at the ferromagnetic-antiferromagnet interface [199]. It has been found to enhance with reduction in particle size thereby revealing increasing density of uncompensated spins. Thus, particle size has a vital role.

Table 4.2 Structural, magnetic and electric parameters of B4, Sr4, Sr5 and Sr6 nanoparticles

| Sample | Structural parameters | | | | Magnetic parameters | | | Electric parameters | | | | |
|---|---|---|---|---|---|---|---|---|---|---|---|---|
| | D nm | a Å | c Å | V $Å^3$ | $M_s$ emu/g | $H_{eb}$ Oe | $M_{shift}$ emu/g | $\varepsilon$ Loss @ 0.1 kHz | | $P_s$ $\mu C/cm^2$ | $P_r$ $\mu C/cm^2$ | $E_c$ kV/cm |
| B4 | 21.3 | 5.57 | 13.84 | 373.06 | 2.5 | 0.69 | 0.0035 | 699 | 0.4 | 2.5 | 2.4 | 19.4 |
| Sr4 | 15.3 | 5.59 | 13.78 | 373.63 | 5.3 | 0.28 | 0.2171 | 654 | 1.0 | 1.6 | 1.0 | 3.3 |
| Sr5 | 16.7 | 5.61 | 13.69 | 373.60 | 3.9 | 0.01 | 0.0015 | 551 | 1.2 | 1.4 | 0.8 | -7.4 |
| Sr6 | 20.2 | 5.59 | 13.76 | 372.54 | 1.1 | 6.2 | 0.0005 | 93 | 2.2 | 0.8 | 0.4 | 3.6 |

### 4.2.2.4 Electrical analysis

#### 4.2.2.4.1 Dielectric analysis

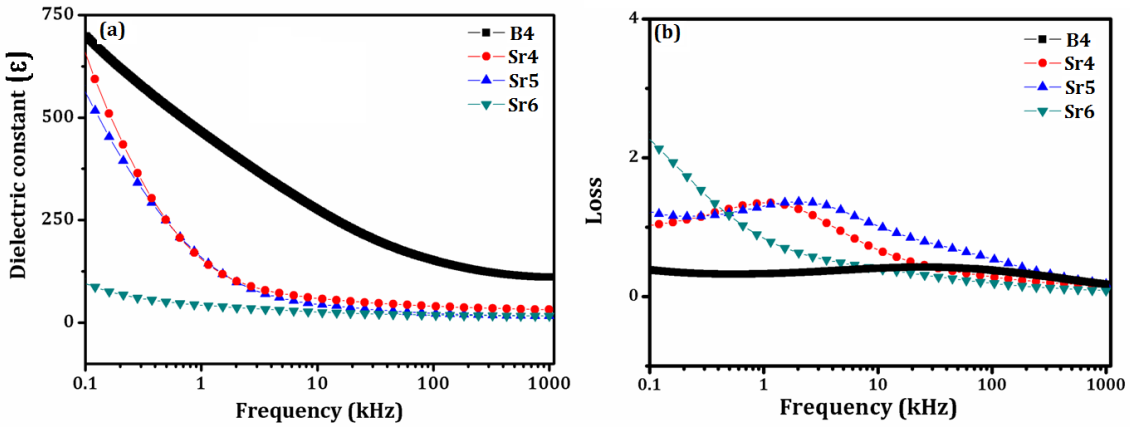


Fig. 4.11 Room temperature frequency response of dielectric constant and loss of B4, Sr4, Sr5 and Sr6 nanoparticles in the range 0.1-1000 kHz

Fig. 4.11 illustrates the room temperature frequency dependence of dielectric constant and loss of the synthesized nanoparticles in the frequency range of 0.1-1000 kHz. The

presence of space charges in the synthesized nanoparticles manifests from the observed dispersions in the dielectric behavior [92]. The dispersions in dielectric constant and a corresponding relaxation peak in loss are apparently due to Maxwell-Wagner relaxation mechanism [212]. The mechanism states that space charges are able to follow the applied field at lower frequencies but they are unable to do so at higher frequencies. Oxygen and bismuth vacancies, various lattice distortions, and defects at the interfaces as well as inside grains, act as the sources of space charges in $BiFeO_3$ [152]. Higher strain in the nanoscale systems results in strongly coupled electric and magnetic orders. The higher values of dielectric constant at lower frequencies are also due to the presence of different kinds of polarizations, namely, electrode, dipolar, electronic, atomic, ionic and interfacial. However, at higher frequencies only electronic polarization contributes [202], which results in the decrease of dielectric constant.

All the nanoparticles have been observed to exhibit Debye-type relaxation [137]. The as-obtained values of dielectric constant and loss are summarized in Table 4.2. The values point toward decay of dielectric constant with the inclusion of $Sr^{2+}$ ions in $BiFeO_3$ lattice similar to previous report [137]. Sr-substitution has resulted in enhanced loss, which indicates deterioration of dielectric properties (Fig. 4.11). The reason may be attributed to the creation of oxygen vacancies due to the substitution of $Sr^{2+}$ (divalent ions) at the trivalent ($Bi^{3+}$) site for the maintenance of charge neutrality in the system [138]. Oxygen vacancies induce conductivity, which enhance leakage current density and thus lowers the dielectric constant.

Particle size has been found to effectively influence the dielectric constant values of Sr-doped $BiFeO_3$ nanoparticles (Table 4.2). The reason is attributed to the size effects of nanosized grains (as revealed by FEG-SEM micrographs) [130]. The decrease in calcination temperature has been found to lower the grain size as well. It indicates the increase in volume

fraction of grain boundaries. These act as large insulating barriers between the grains when the grain size is very small and hampers the mobility of charge carriers resulting in decrease of conductivity in the system [152]. Thus, accordingly the dielectric constant value has been found to increase with the decreasing grain size. It indicates the decrease of oxygen vacancies with reducing particle size.

The crystallite size value has been found to decrease with the Sr-doping. However, the formation of oxygen vacancies for charge neutrality has possibly resulted in the degradation of dielectric constant, according to the defect chemistry [92].

#### 4.2.2.4.2 Ferroelectric analysis

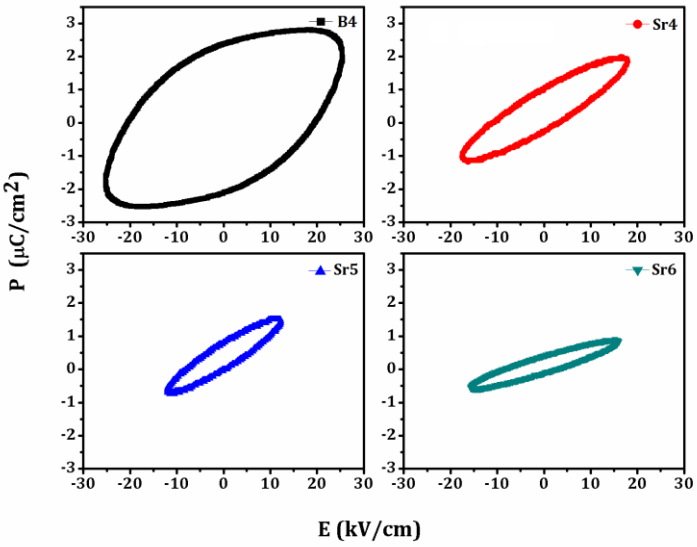


Fig. 4.12 P-E loops of B4, Sr4, Sr5 and Sr6 nanoparticles at room temperature

Fig. 4.12 shows room temperature P-E loops of the synthesized nanoparticles at frequency of 100 Hz. Table 4.2 summarizes various electric hysteresis parameters obtained from P-E loops. It has been observed that $BiFeO_3$ nanoparticles show well saturated P-E loop in contrast to its bulk counterpart. In $BiFeO_3$, Bi being volatile deviates oxygen

stoichiometry, which results in creation of oxygen vacancies, unstablization of oxidation state of Fe ($Fe^{2+}$, $Fe^{3+}$) and formation of secondary phases thereby leading to high conductivity issues in this material [76-77]. However, at nanoscale, the low formation temperature prevents volatization of Bi and thus preserves Bi content in the material, which consequently avoids the high conductivity related issues in $BiFeO_3$.

Sr-doping has been found to degrade the ferroelectricity of $BiFeO_3$, which is due to the formation of oxygen vacancies when divalent ion ($Sr^{2+}$) substitutes the trivalent ion ($Bi^{3+}$) for maintaining the charge neutrality of the system [137].

Particle size variation has been observed to influence the ferroelectric behaviour of Sr-doped $BiFeO_3$ nanoparticles. It has been found that increasing particle size deteriorates the spontaneous and remnant polarization values. The reason may be attributed to the presence of nano-sized grains in the synthesized nanoparticles. These act as insulating barrier for the mobile charge carriers in the system [152]. Larger the grain size, poorer is the insulation and thus ferroelectricity decreases.

## 4.3 Ba-doped $BiFeO_3$ nanoparticles ($Bi_{1-x}Ba_xFeO_3$; x = 0, 0.15)

### 4.3.1 Synthesis

The procedure followed for the synthesis of undoped and Ba-doped $BiFeO_3$ (x = 0.15) nanoparticles is same as described in section (3.2.1). The undoped $BiFeO_3$ nanoparticles were obtained by calcination at $450^0$C (Bi4) for 4 hour. Nanoparticles of Ba-doped $BiFeO_3$ of different sizes have been obtained by the calcination at different temperatures viz., 450 $^0$C (Ba4), 550 $^0$C (Ba5) and 650 $^0$C (Ba6) for 4 hour.

### 4.3.2 Results and discussion

#### 4.3.2.1 Structural and phase analyses

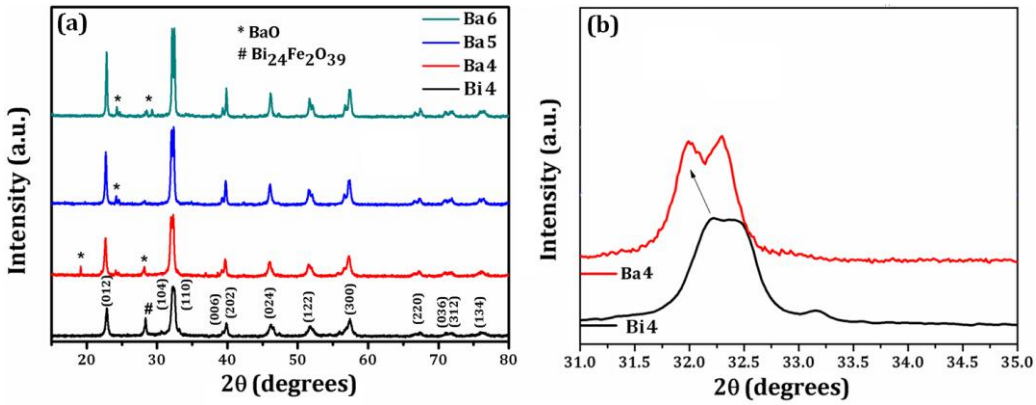


Fig. 4.13 (a) XRD patterns of Bi4, Ba4, Ba5 and Ba6 nanoparticles at room temperature and (b) enlarged view of XRD patterns at around 2θ ~ 32° for Bi4 and Ba4 nanoparticles

Fig. 4.13 (a) shows XRD patterns of Bi4, Ba4, Ba5 and Ba6 nanoparticles. All the diffraction peaks characterize rhombohedral structure of undoped $BiFeO_3$ having $R_{3c}$ space group (JCPDS Card No. 86-1518). Traces of impurities denoted by # and * (Fig. 4.13 (a)) correspond to $Bi_{24}Fe_2O_{39}$ (JCPDS Card No. 42-0201) and BaO (JCPDS Card No. 26-0177), respectively. Structural parameters, namely, crystallite size and lattice parameters are summarized in Table 4.3.

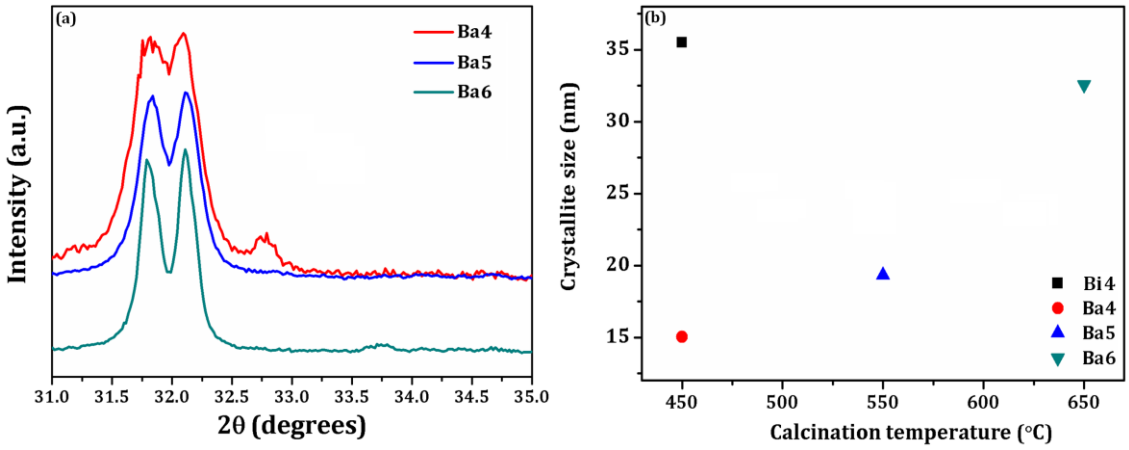


Fig. 4.14 (a) Enlarged view of XRD patterns at around 2θ ~ 32° for Ba4, Ba5, Ba6 nanoparticles and (b) variation of crystallite size of all the synthesized nanoparticles with calcination temperature

Remarkable features have been observed with Ba-substitution in $BiFeO_3$ lattice. Enlarged view of XRD patterns at around 2θ ~ 32º in Fig. 4.13 (b) reveals that Ba-substitution has not resulted in structural transformation of rhombohedral phase of undoped $BiFeO_3$ since splitting of (104) and (110) peaks in Bi4 do not merge into a single peak; this is one of the signatures of structural transformation. This indicates no reduction in lattice symmetry in the present system. Similar observations reporting no structural transformations are available for alkaline earth metal doped $BiFeO_3$ [92]. However, substitution of $Ba^{2+}$ ions in $BiFeO_3$ lattice is confirmed by the shifting of diffraction peaks towards lower 2θ with respect to the undoped $BiFeO_3$ (Fig. 4.13 (b)). The reason may be attributed to the substitution of $Ba^{2+}$ (1.42 Å) ions having larger ionic radii at smaller Bi (1.17 Å) site [97].

The various structural parameters of the synthesized nanoparticles have been given in Table 4.3. From the values summarized in Table 4.3, it has been found that the doping leads to remarkable reduction of the crystallite size, which is also, illustrated by the relatively broadened diffraction peaks of Ba-doped $BiFeO_3$ nanoparticles with respect to undoped nanoparticles (Fig. 4.14 (a)). Reason for reduction may be attributed to the inhibited crystal growth caused by the substitution of divalent ion ($Ba^{2+}$) in place of trivalent ion ($Bi^{3+}$) [97, 137].

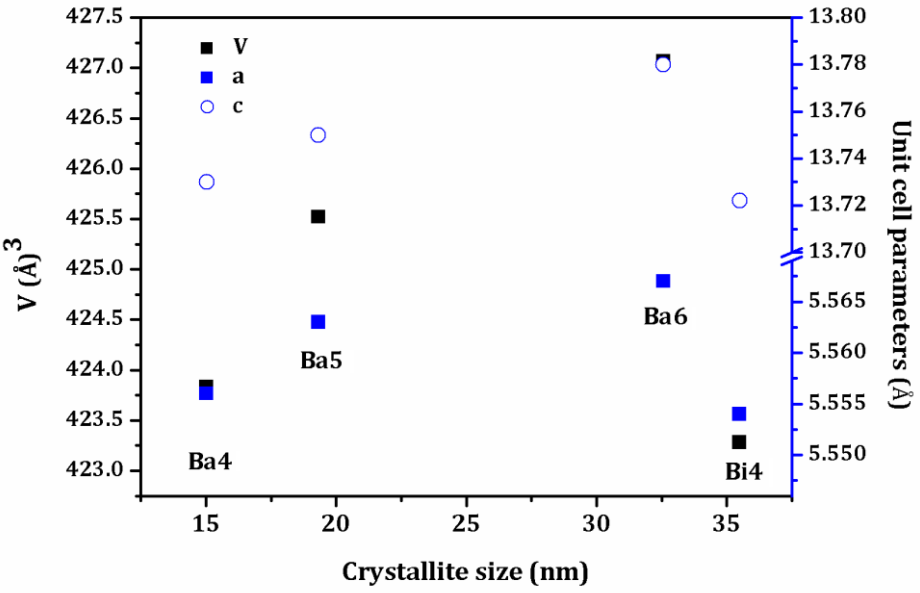


Fig. 4.15 Volume and lattice parameters of Bi4, Ba4, Ba5 and Ba6 nanoparticles as a function of crystallite size

The influence of increasing calcination temperature for $Bi_{1-x}Ba_xFeO_3$ (x = 0.15) nanoparticles has been observed. The diffraction peaks has been found to sharpen with the increasing calcination temperature (Fig. 4.15 (a)). This reveals the increase of crystallinity and crystallite size - an observation well in agreement with the values of crystallite size calculated using Debye-Scherrer equation (Table 4.3). It has been observed that crystallite size increases as a function of increasing calcination temperature (4.14 (b)). Fig. 4.14 (a) also illustrates the shifting of diffraction peaks towards higher 2θ with the decreasing crystallite size. It indicates the decrease of lattice parameters with the decrease of crystallite size, shown in Fig. 4.15. This observation corroborates well with the calculated lattice parameters (Table 4.3).

### 4.3.2.2 Morphological analysis

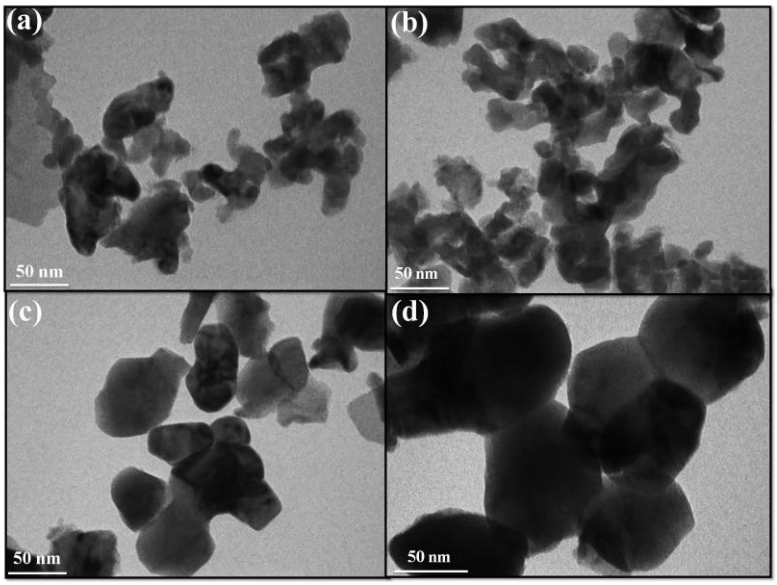


Fig. 4.16 TEM micrographs of (a) Bi4 (b) Ba4 (c) Ba5 and (d) Ba6 nanoparticles

The topographical analysis has been carried out with the help of TEM. Fig. 4.16 represents TEM micrographs of Bi4, Ba4, Ba5 and Ba6 nanoparticles. The irregular morphology of the agglomerated nanoparticles has been observed whose reason is attributed to the high surface energy of nanoparticles [107-108, 202]. Agglomeration has been observed to decrease as the particle size increases. The average particle size has been found out to be 31, 19, 53, and 74 nm, respectively, for Bi4, Ba4, Ba5 and Ba6 nanoparticles. The reduction in particle size by the substitution is well in agreement with XRD analysis. The growth mechanism of the synthesized nanoparticles formed by sol-gel has been found to take place via homogeneous nucleation [18]. The details of the mechanism are described in section 3.1.2.2.

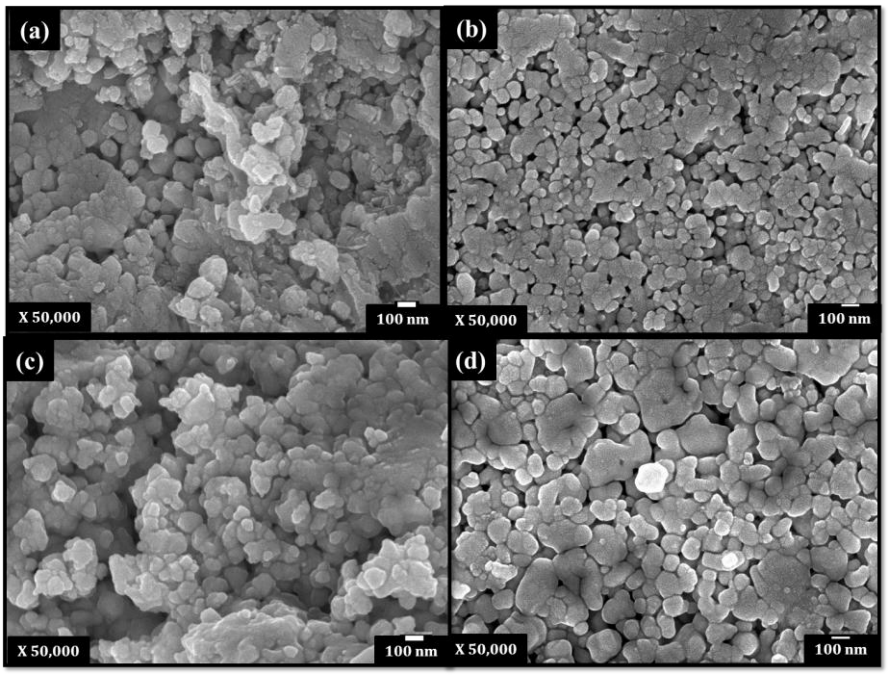


Fig. 4.17 FEG-SEM micrographs of (a) Bi4 (b) Ba4 (c) Ba5 and (d) Ba6 nanoparticles at 50k X

Fig. 4.17 illustrates the FEG-SEM micrographs of Bi4, Ba4, Ba5 and Ba6 nanoparticles at same magnification (50k X) and scale (100 nm). The morphological analysis reveals uniformly distributed densely packed grains having well-defined boundaries. This is indicative of their crystalline nature. Fig. 4.17 depicts the morphology of all the nanoparticles to be almost spherical. A comparative demonstration of microstructures, shown in Fig. 4.17, at 50k X, reveals that doping of $Ba^{2+}$ ions remarkably reduced the grain size. This happens due to the inhibited grain growth by $Ba^{2+}$ ions resulting from divalent substitution for trivalent ions, and, thus, helps in the densification [97, 137]. Also, the grain size has been observed to increase with calcination temperature. Coalescence of grains via grain boundaries results in the growth with the increase of temperature [197]. Thus, morphological analysis supports that the calcination temperature has direct effect nanoparticles' size.

### 4.3.2.3 Magnetic analysis

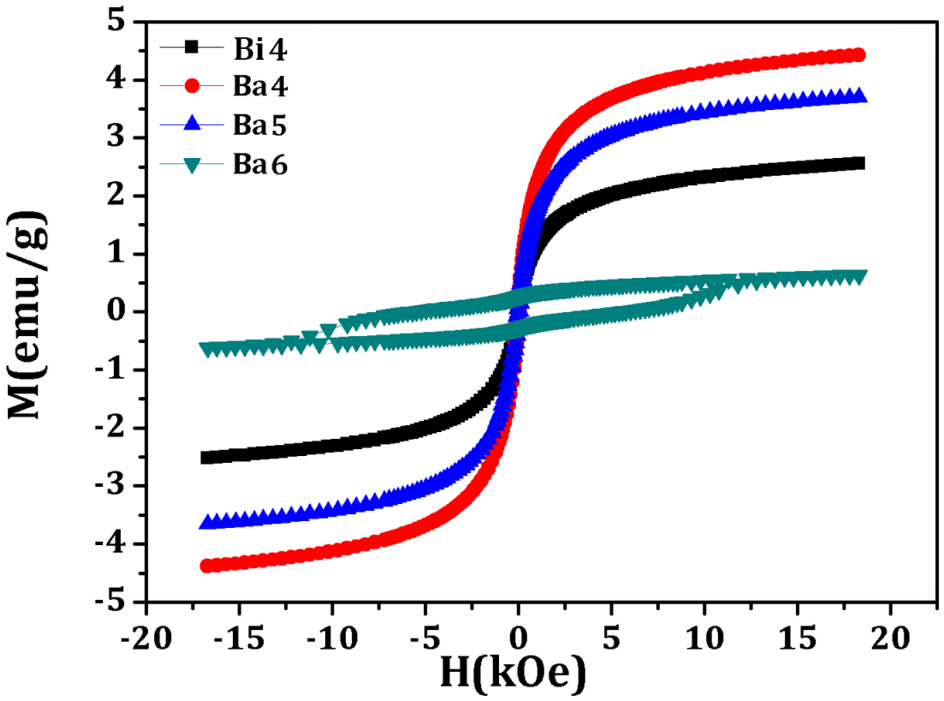


Fig. 4.18 Room temperature magnetization hysteresis loops of Bi4, Ba4, Ba5 and Ba6 nanoparticles

Fig. 4.18 illustrates room temperature magnetic hysteresis loops of Bi4, Ba4, Ba5 and Ba6 nanoparticles. All the loops exhibit ferromagnetism similar to other alkaline earth metal ions doped $BiFeO_3$ nanoparticles [137, 153]. Various magnetic parameters are summarized in Table 4.3. Traces of impurities, namely, $Bi_{24}Fe_2O_{39}$ [130] and BaO [209] do not exhibit room temperature magnetism, and, hence, rules out the possibility of their contribution towards room temperature magnetic behavior. Undoped $BiFeO_3$ nanoparticles have been found to display ferromagnetism contrary to the antiferromagnetic nature of its bulk counterpart [107-108]. Two reasons may be attributed to this behaviour. Firstly, it is the modulation of long-range spin spiral structure of $BiFeO_3$ due to its size (31 nm, as revealed by TEM) being less than its incommensurate period of 62 nm, due to which, the effect known as grain size confinement effect comes into play. It partially destroys the long-range spin cycloidal

structure thereby, leading to ferromagnetism [110]. Secondly, it is the antiferromagnetic nature of $BiFeO_3$ [107-108, 110, 130, 137], which possess spin sublattices having ferromagnetic interactions within the sublattice and antiferromagnetic interactions between sublattices. This results in magnetic moment due to incomplete spin compensation between sublattices, as the antiferromagnetic order gets interrupted at the particle's surface as per the Néel's theory [152]. Further, owing to the large surface to volume ratio in case of antiferromagnetic nanoparticles, the uncompensated spins at the surface becomes remarkable, and, hence, enhances overall magnetization of the system [110].

Enhancement in saturation magnetization value has been observed with the doping of $Ba^{2+}$ ions, which is consistent with the other alkaline earth metal ions doped $BiFeO_3$ nanoparticles [137-138]. The saturation magnetization for undoped $BiFeO_3$ has been found to be 2.5 emu/g and with Ba-substitution it enhances by 1.7 times. Two reasons may be attributed to this behaviour. First, it is the suppression of spin spiral structure of $BiFeO_3$ by the reduction of particle size to 19 nm (below 62 nm, as revealed by the TEM image). Second, it is the substitution of divalent ion ($Ba^{2+}$ ions) at trivalent ($Bi^{3+}$ ions) sites in the lattice [137]. This creates charge imbalance thereby destabilizing the system. So, one oxygen vacancy is created for every two alkaline earth metal ions to maintain the neutrality in the system. These oxygen vacancies suppress spin spiral structure, and, thus, result in the enhanced ferromagnetism in the Ba-substituted $BiFeO_3$ nanoparticles [137].

Strong correlation between particle size and magnetic property has been observed. The magnetization increases remarkably as the particle size decreases (Table 4.3). This observation is consistent with other size-dependent reports. The reason may be attributed to the increase in surface to volume ratio [107, 110]. Since, in antiferromagnetic nanoparticles, as discussed above, the contribution of uncompensated magnetic spins increases with the

surface to volume ratio, therefore, the magnetism enhances as the particle size reduces. This observation is well in accordance with Néel's modelling of the present system. Moreover, the particles possessing size below 62 nm, depict strong size-dependent magnetism owing to the fact that the grain size confinement effect modulates the spin spiral structure of $BiFeO_3$ [110].

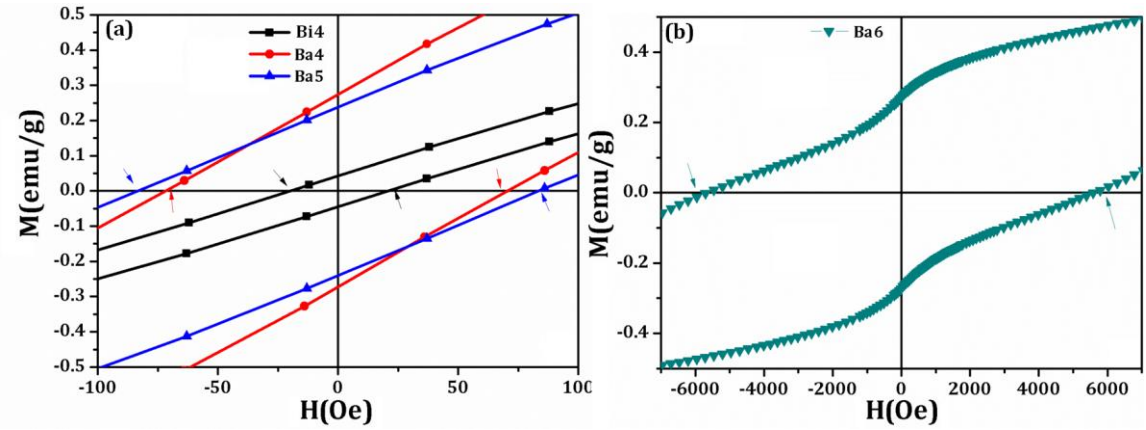


Fig. 4.19 Zoomed in view of magnetization hysteresis loops showing the presence of hysteresis and exchange bias coupling of (a) Bi4, Ba4, Ba5 and (b) Ba6 nanoparticles

The zoomed in view of magnetization hysteresis loops are shown in Fig. 4.19. These indicate vertical as well as horizontal asymmetry. The exchange bias field and vertical shift (Table 4.3) for the synthesized nanoparticles has been calculated using Eq. 3.4 and 3.5, respectively. These support ferromagnetism and spin pinning at the ferromagnetic – antiferromagnetic interfaces as well as rules out the possibility of superparamagnetism [107]. These shifts are attributed to exchange coupling between ferromagnetic surfaces and antiferromagnetic cores [135]. The rarely observed $M_{shift}$ indicates the presence of uncompensated spins at the ferromagnetic-antiferromagnet interface [199]. $M_{shift}$ has been observed to enhance with reducing size (Table 4.3) due to the lowering density of uncompensated spins. It is in consistence with the explanation done using Nèel's modelling. It also enhances with reducing particle size.

Table 4.3 Structural, magnetic and electric parameters of Bi4, Ba4, Ba5 and Ba6 nanoparticles

| Sample | Structural parameters | | | | Magnetic parameters | | | Electric parameters | | | | |
|---|---|---|---|---|---|---|---|---|---|---|---|---|
| | D nm | a Å | c Å | V $Å^3$ | $M_s$ emu/g | $H_{eb}$ Oe | $M_{shift}$ emu/g | $\varepsilon$ Loss @ 0.1 kHz | | $P_s$ $\mu C/cm^2$ | $P_r$ $\mu C/cm^2$ | $E_c$ kV/cm |
| Bi4 | 35.5 | 5.554 | 13.72 | 423.28 | 2.5 | 0.23 | 0.04 | 697 | 0.4 | 2.67 | 2.24 | 20.03 |
| Ba4 | 15.0 | 5.556 | 13.73 | 423.83 | 4.4 | 0.32 | 0.06 | 595 | 1.6 | 1.07 | 0.68 | 12.20 |
| Ba5 | 19.3 | 5.563 | 13.75 | 425.52 | 3.6 | 0.20 | 0.02 | 153 | 3.4 | 33.61 | 34.22 | 2.23 |
| Ba6 | 32.5 | 5.567 | 13.78 | 427.06 | 0.6 | 16.06 | 0.012 | 33 | 0.6 | 59.50 | 59.33 | 2.15 |

### 4.3.2.4 Electrical analysis

#### 4.3.2.4.1 Dielectric analysis

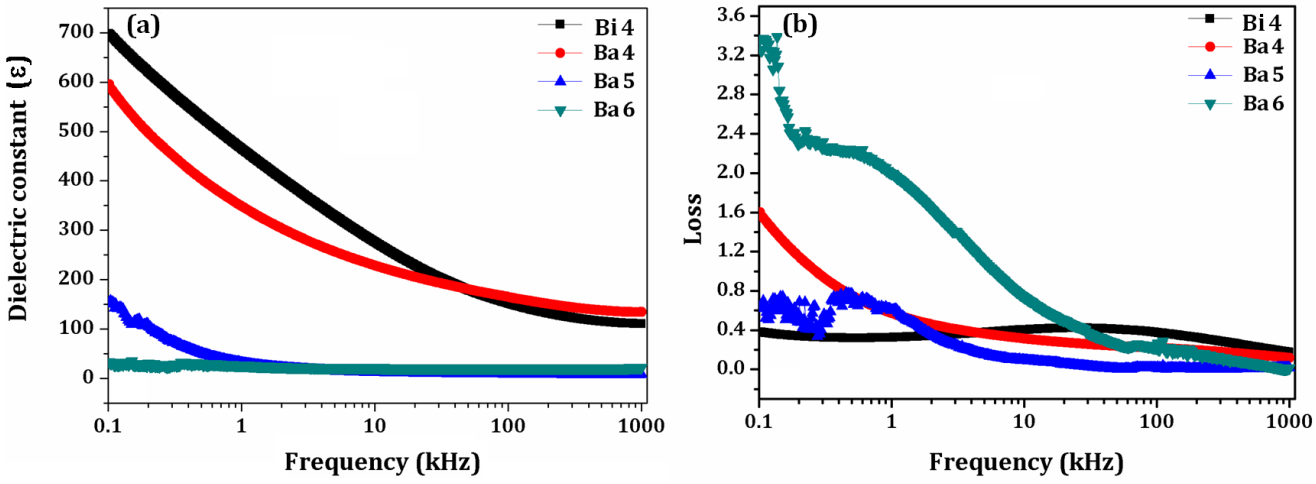


Fig. 4.20 Room temperature frequency dependence of (a) dielectric constant and (b) dielectric loss of Bi4, Ba4, Ba5 and Ba6 nanoparticles in the range 0.1-1000 kHz

Fig. 4.20 shows the room temperature frequency response of dielectric constant and loss in the range 0.1 – 1000 kHz. The dispersions in the dielectric behaviour have been observed in all the nanoparticles. This phenomenon is related to space charge relaxation effect. Lattice distortions, oxygen and bismuth vacancies, and defects at the interfaces as well as inside grains are the sources of space charges in $BiFeO_3$ [152]. These space charges are able to follow the applied field at lower frequencies but they are unable to do so at higher frequencies [137]. Also, different kinds of polarizations contribute towards dielectric constant, namely, electronic, atomic, ionic and interfacial. However, at higher frequencies only electronic polarization contributes [202], which also leads to the decrease of dielectric constant at higher frequencies.

` Debye-like relaxation has been observed for all the nanoparticles [137]. Undoped $BiFeO_3$ nanoparticles have been found to possess dielectric constant of 697. However, on Ba-substitution in $BiFeO_3$, a decay of 0.85 times has been registered. Increase in loss value with Ba-substitution also indicates degradation of dielectric properties (Fig. 4.20 (b)). Addition of divalent ions ($Ba^{2+}$) at the trivalent site ($Bi^{3+}$) results in the formation of oxygen vacancies for maintaining neutrality in the system [137]. These are the well-known sources responsible for the decay of dielectric constant as they induce dc conductivity [135]. Thus, consequently, a decrease has been observed in the dielectric constant.

The dielectric constant of Ba-doped $BiFeO_3$ nanoparticles shows particle size dependence. The values summarized in Table 4.3 points towards decrease of dielectric constant with the increasing particle size. Reason may be attributed to formation of nanosized grains indicated by FEG-SEM micrographs. These provide large insulation to the mobile charge carriers thereby decreasing conductivity of the system [130]. As, the grain size has been found to increase with increasing calcination temperature, consequently, the dielectric

constant registers decrease. Although, a decrease of crystallite size has been observed with Ba-doping as well, but the defect chemistry corresponds to the formation of oxygen ion vacancies for charge compensation; these possibly lead to the degradation of dielectric constant value [92].

#### 4.3.2.4.2 Ferroelectric analysis

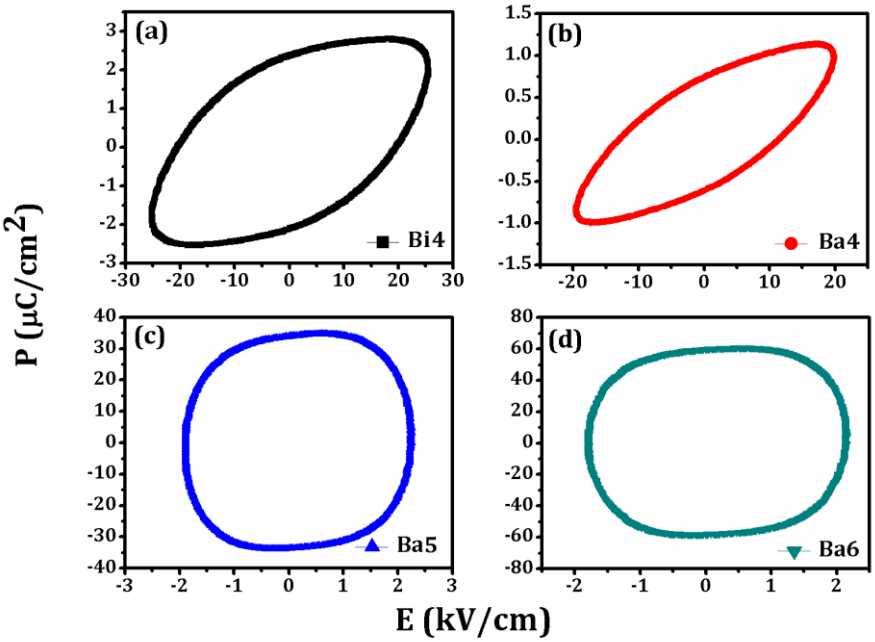


Fig. 4.21 Ferroelectric hysteresis loops of (a) Bi4, (b) Ba4, (c) Ba5, and (d) Ba6 nanoparticles at room temperature

Fig. 4.21 shows the room temperature ferroelectric measurements of the synthesized nanoparticles were performed at frequency of 100 Hz. The electric hysteresis parameters obtained from P-E loops are summarized in Table 4.3. The stereochemical activity of $6s^2$ lone pair of Bi with respect to oxygen octahedra results in polarization in $BiFeO_3$ [210]. Bulk $BiFeO_3$ is known to suffer from impurities and non-stoichiometric issues as the thermodynamic stability of $BiFeO_3$ is in low temperature range [71], which hampers its

complete polarization. However, reduction of size to nanoscale has been observed to improve the ferroelectric behavior of $BiFeO_3$. Two reasons may be attributed to it [76-77, 110, 211]: (i) the suppression of the secondary phase formation at nanoscale as the formation temperature involved is quite low that prevents the Bi from volatizing and (ii) the nanoscale samples are denser and possess less porosity as compared to bulk, which results in reduction of leakage current.

Ba-doping has been observed to degrade the ferroelectric behaviour of $BiFeO_3$ (Table 4.3). The reason may be attributed to the creation of oxygen vacancies for the charge maintenance in the system as the divalent $Ba^{2+}$ ions substitutes $Bi^{3+}$ ions [137]. The oxygen vacancies enhance the conduction and thus lower the polarization value.

Particle size has been found to influence the ferroelectric behaviour of Ba-doped $BiFeO_3$ nanoparticles. It has been observed that the ferroelectricity deteriorates as the particle size increases (Fig. 4.21). The reason may be attributed to the presence of nano-sized grains in the synthesized nanoparticles. These are effective in obstructing the mobile charge carriers [130]. The smaller grain size thus provides better hindrance to the mobility of charge carriers. Accordingly, the spontaneous polarization value has been observed to decrease with the increase in particle size (Table 4.3). The round shaped P-E loops are indicative of high leakage current, which is the case with Ba5 nanoparticles (Fig. 4.21 (c)). It happens due to the contribution from mobile charges resulting from the valence fluctuations of Fe ions [110, 120-121]. On raising the temperature further to 650 ºC, the Ba6 nanoparticles (Fig. 4.21 (d)) exhibit a complete circle like P-E loop that indicates severe leakage current and implies that the sample is highly conductive at room temperature [97].

# *Chapter 5*

# *CONCLUSIONS*

# Chapter 5

This chapter concludes the entire work done, along with an insight into the future possibilities of the present research work.

## 5.1 Conclusions

This thesis presents a study on undoped $BiFeO_3$ nanoparticles, rare earth (Tb, Dy, Gd) and alkaline earth metal ions (Ca, Sr, Ba)-doped $BiFeO_3$ nanoparticles. Further, the particle size of these systems varied, and their structural, morphological, magnetic and electrical analyses done. The research work presented is divided into three sections with dopant systems having three combinations each, as given below.

### I. $BiFeO_3$ nanoparticles

- $BiFeO_3$ nanoparticles were synthesized by sol-gel method. Their particle size was tailored by varying the calcinations temperature.
- XRD patterns showed the rhombohedral structure for all the synthesized nanoparticles.
- Topographical investigations, done by TEM, revealed agglomerated nanoparticles with average particle size, 27.3 and 153.2 nm, for Bi4 and Bi6 nanoparticles, respectively. The microstructural analysis by FEG-SEM has been found to show densely packed grains having well-defined boundaries. The average grain size was found to increase with calcination temperature.
- Magnetic analysis confirmed ferromagnetic nature of all the synthesized nanoparticles. The incomplete spin compensation in small antiferromagnetic

nanoparticles exhibited measurable magnetization with particle size below 62 nm suppressing the spin spiral structure of $BiFeO_3$, which results in ferromagnetism. The effect of particle size on the magnetic properties was studied. The saturation magnetization value was observed to enhance with reducing particle size due to the increase in the number of uncompensated spins.

- The dielectric as well as ferroelectric properties were found to improve with reduction in particle size of $BiFeO_3$ nanoparticles. The reason is attributed to the presence of nanosized grains. The grain boundaries increase with reduction in size that provide large insulating barrier to the conduction current. The smaller grains efficiently prevent conductivity compared to the larger ones. Consequently, the dielectric constant and ferroelectric properties registered an improvement.

Table 5.1 summarises the structural, magnetic and electric parameters obtained for the undoped $BiFeO_3$ nanoparticles. .

Table 5.1 A comparison of structural, magnetic and electric parameters obtained for the undoped-$BiFeO_3$ nanoparticles

| Sample | Structural parameters | | | | Magnetic parameters | | | Electric parameters | | | | |
|---|---|---|---|---|---|---|---|---|---|---|---|---|
| | D nm | a Å | c Å | V $Å^3$ | $M_s$ emu/g | $H_{eb}$ Oe | $M_{shift}$ emu/g | $\varepsilon$ Loss @ 0.1 kHz | | $P_r$ $\mu C/cm^2$ | $P_s$ $\mu C/cm^2$ | $E_c$ kV/cm |
| Bi4 | 12.7 | 5.585 | 13.822 | 431.1 | 3.12 | 0.1650 | 0.2001 | 272 | 0.03 | 3.32 | 4.82 | 11.59 |
| Bi5 | 28.6 | 5.582 | 13.825 | 430.7 | 2.13 | 0.0025 | 0.0203 | 246 | 0.08 | 1.41 | 2.00 | 4.08 |
| Bi6 | 53.2 | 5.573 | 13.842 | 429.9 | 0.38 | 0.0020 | 0.0052 | 233 | 4.20 | 9.03 | 0.80 | 3.63 |

## II. Rare earth-doped $BiFeO_3$ nanoparticles

### 1. Tb-doped $BiFeO_3$ nanoparticles ($Bi_{1-x}Tb_xFeO_3$; x = 0, 0.15)

- The synthesis of Tb-doped $BiFeO_3$ nanoparticles was done by sol-gel method.
- XRD patterns showed the structural transformation from rhombohedral to orthorhombic structure with the doping of $Tb^{3+}$ ions in $BiFeO_3$ lattice.
- TEM micrographs revealed highly agglomerated $BiFeO_3$ nanoparticles of average particle size 40 nm. High agglomeration is attributed to the high surface energy of the nanoparticles.
- SEM analysis revealed reduction in grain size with Tb-doping. Further, the grain size of Tb-doped $BiFeO_3$ nanoparticles was observed to increase with calcination temperature. The grains coalesce via grain boundaries with the rise in temperature
- Magnetic analysis showed enhancement in saturation magnetization value with Tb-doping, as the smaller ionic radii of $Tb^{3+}$ ions distort the rhombohedral lattice that suppresses the spin spiral structure of $BiFeO_3$. This value further enhanced on reducing the particle size owing to the increasing surface to volume ratio, which in turn increases the density of the uncompensated spins contributing towards the magnetism.
- The dielectric property was found to improve with Tb-doping owing to the rhombohedral distortion of $BiFeO_3$. The influence of particle size on the dielectric properties of the Tb-doped $BiFeO_3$ nanoparticles reveals the reduction in the dielectric constant with the increase in the size of the nanoparticles; the reason is their smaller nanosized grains providing better obstruction to the charge carriers compared to the larger ones.

- The doping of $Tb^{3+}$ ions in $BiFeO_3$ lattice has resulted in enhanced ferroelectric properties as it leads to the formation of less centrosymmetric orthorhombic structure. The spontaneous polarization and applied electric field values were observed to decrease with increasing particle size of Tb-doped $BiFeO_3$ nanoparticles, thereby indicating the degradation of the ferroelectric property.

**2. Dy-doped $BiFeO_3$ nanoparticles ($Bi_{1-x}Dy_xFeO_3$; x = 0, 0.15)**

- Sol-gel method was used to synthesize the Dy-doped $BiFeO_3$ nanoparticles.
- The structural analysis by XRD revealed rhombohedral to orthorhombic structural transformation due to the doping of $Dy^{3+}$ ions in $BiFeO_3$ lattice.
- TEM micrographs exhibited nanoparticles having average particle size 30, 20, 45 and 86 nm for P4, Dy4, Dy5 and Dy6, respectively. Agglomeration was observed to decrease with increasing particle size of Dy-doped $BiFeO_3$ nanoparticles.
- The FEG-SEM micrographs revealed uniform distribution of densely packed grains with well-defined boundaries. Doping of $Dy^{3+}$ ions resulted in reduction of the grain size. The grain size was observed to increase with the increase in calcinations temperature of Dy-doped $BiFeO_3$ nanoparticles.
- Magnetic analysis, by VSM, revealed that Dy-doping enhanced the saturation magnetization value as it induces rhombohedral distortion due to its smaller ionic radii as compared to $Bi^{3+}$ ions. Further, the saturation magnetization value was found to increase with reducing particle size owing to the increasing surface to volume ratio.
- Dy-doping in $BiFeO_3$ lattice enhanced the dielectric and ferroelectric properties owing to the structural transformation to orthorhombic phase. Further, these

properties were observed to enhance on the reduction of particle size of Dy-doped $BiFeO_3$ nanoparticles. These comprise of nanosized grains that act as insulating barrier to the mobile charge carriers.

### 3. Gd-doped $BiFeO_3$ nanoparticles ($Bi_{1-x}Gd_xFeO_3$; x = 0, 0.15)

- Sol-gel method was employed for the synthesis of Gd-doped $BiFeO_3$ nanoparticles.
- XRD patterns revealed rhombohedral distortion of $BiFeO_3$ lattice by $Gd^{3+}$ ions.
- TEM micrographs revealed highly agglomerated Gd4 and Gd6 nanoparticles of irregular morphology. Their average particle size was found out to be 16 and 150 nm, respectively.
- The FEG-SEM micrographs illustrated the increase in grain size with calcination temperature for the Gd-doped $BiFeO_3$ nanoparticles, thereby indicating grain growth with temperature.
- Magnetic measurements exhibited enhanced magnetization by $Gd^{3+}$ ions owing to its high magnetic moment and induction of large lattice distortion in $BiFeO_3$ lattice. Further, the magnetization was found to increase with decreasing particle size of Gd-doped $BiFeO_3$ nanoparticles; the reason being that the surface to volume ratio increases. It increases the density of uncompensated spins on the surface, which thus enhances magnetization.
- The dielectric and ferroelectric properties have been observed to improve by $Gd^{3+}$ ions. The rhombohedral lattice distortion by substitution of smaller $Gd^{3+}$ ion (0.938 Å) at larger $Bi^{3+}$ ion (1.17 Å) results in less centrosymmetric crystal

structure that gives rise to more polar displacements and thus, higher dielectric constant and polarization values. Further, these properties were observed to enhance with reducing particle size of Gd-doped $BiFeO_3$ nanoparticles. The attributed reason is the presence of nanosized grains, which act as large insulating barriers to mobile charge carriers.

Table 5.2 summarises the structural, magnetic and electric parameters obtained for for the rare earth (Tb, Dy, Gd) doped-$BiFeO_3$ nanoparticles.

Table 5.2 A comparison of structural, magnetic and electric parameters obtained for the rare earth (Tb, Dy, Gd) doped-$BiFeO_3$ nanoparticles

| Property → / Sample ↓ | | Structural parameters | | | | | Magnetic parameters | | | Electric parameters | | | | |
|---|---|---|---|---|---|---|---|---|---|---|---|---|---|---|
| | | D nm | a Å | b Å | c Å | V $Å^3$ | $M_s$ emu/g | $H_{eb}$ Oe | $M_{shift}$ emu/g | $\varepsilon$ Loss @ 0.1 kHz | | $P_r$ μC/$cm^2$ | $P_s$ μC/$cm^2$ | $E_c$ kV/cm |
| $Bi_{1-x}Tb_xFeO_3$ (x = 0, 0.15) | Und-oped | 31.7 | 5.574 | 5.574 | 13.781 | 428.2 | 1.3 | 5.2 | 1.300 | 725 | 0.40 | 2.6 | 1.4 | 10.4 |
| | Tb4 | 14.5 | 5.411 | 5.573 | 7.700 | 232.2 | 3.1 | 11.2 | 3.200 | 4163 | 1.20 | 10.0 | 6.2 | 30.1 |
| | Tb5 | 20.2 | 5.570 | 5.590 | 7.710 | 232.4 | 2.0 | 7.9 | 1.940 | 2083 | 1.00 | 6.1 | 4.1 | 25.4 |
| | Tb6 | 28.6 | 5.577 | 5.578 | 7.754 | 234.0 | 0.8 | 44.3 | 0.720 | 1388 | 1.10 | 4.2 | 2.4 | 26.3 |
| $Bi_{1-x}Dy_xFeO_3$ (x = 0, 0.15) | P4 | 14.8 | 5.570 | 5.570 | 13.86 | 430.0 | 2.2 | 2.0 | 0.820 | 699 | 0.38 | 4.2 | 3.4 | 13.4 |
| | Dy4 | 6.2 | 3.190 | 5.540 | 7.830 | 138.5 | 13.8 | 2.2 | 0.070 | 11,645 | 0.36 | 12.4 | 8.3 | 41.3 |
| | Dy5 | 8.9 | 3.200 | 5.550 | 7.840 | 139.3 | 4.4 | 1.8 | 0.050 | 2067 | 1.55 | 8.3 | 5.4 | 37.4 |
| | Dy6 | 10.5 | 3.210 | 5.550 | 7.850 | 139.7 | 0.5 | 16.1 | 0.005 | 640 | 1.31 | 2.1 | 1.4 | 19.4 |
| $Bi_{1-x}Gd_xFeO_3$ (x = 0, 0.15) | Bi4 | 21.2 | 5.560 | 5.560 | 13.900 | 429.6 | 2.5 | 1.1 | 0.005 | 690 | 0.34 | 2.6 | 2.1 | 9.1 |
| | Gd4 | 9.2 | 5.600 | 5.590 | 7.800 | 244.2 | 4.9 | 3.2 | 0.002 | 2193 | 0.32 | 8.4 | 7.0 | 13.3 |
| | Gd5 | 16.2 | 5.530 | 5.540 | 7.600 | 232.8 | 1.1 | 1.0 | 0.001 | 777 | 1.30 | 7.1 | 6.2 | 13.4 |
| | Gd6 | 20.1 | 5.510 | 5.360 | 8.100 | 239.2 | 0.6 | 0.5 | 6E-4 | 546 | 1.80 | 5.1 | 4.3 | 8.2 |

## III. Alkaline earth-doped $BiFeO_3$ nanoparticles

### 1. Ca-doped $BiFeO_3$ nanoparticles ($Bi_{1-x}Ca_xFeO_3$; x = 0, 0.15)

- The synthesis of Ca-doped $BiFeO_3$ nanoparticles was done by sol-gel method.
- XRD patterns showed the structural transformation from rhombohedral to orthorhombic structure with the Ca-doping in $BiFeO_3$ lattice.
- The topographical analysis by TEM reveals high agglomeration due to the high surface energy of nanoparticles. The average particle size has been found out to be 11 and 53 nm, for Ca4 and Ca6 nanoparticles respectively.
- The FEG-SEM micrographs exhibited uniform distribution of spherical grains having well-defined boundaries. The comparative illustration at the same length scale revealed increasing grain size with calcination temperature as the smaller grains coalesce via grain boundaries with increasing temperature.
- Magnetic analysis, by VSM, revealed increase in magnetization by Ca-doping as it induces large lattice distortion in $BiFeO_3$ lattice. The magnetization further enhanced on reducing the particle size of Ca-doped $BiFeO_3$ nanoparticles. The increased particle surface area with reduction in particle size increases the number of uncompensated spins on the surface contributing towards magnetization.

- The electrical (dielectric and ferroelectric) properties were observed to enhance with doping of $Ca^{2+}$ ions in $BiFeO_3$. The rhombohedral distortion of the $BiFeO_3$ lattice induced by Ca-doping, results in less centrosymmetric phase, which enhances the dielectric constant and polarization values. Moreover, these properties further show improvement on reduction of the particle size of Ca-doped $BiFeO_3$ nanoparticles owing to the nanosized grains. The smaller nanosized grains are better in obstructing the mobile charge carriers than the larger ones.

**2. Sr-doped $BiFeO_3$ nanoparticles ($Bi_{1-x}Sr_xFeO_3$; x = 0, 0.15)**

- Sol-gel method was used to synthesize the Sr-doped $BiFeO_3$ nanoparticles.
- The structural analysis done by XRD illustrated rhombohedral phase of the synthesized nanoparticles.
- TEM micrographs exhibited agglomerated nanoparticles having average particle size of 16, and 50 nm, respectively, for Sr4 and Sr6.
- The FEG-SEM micrographs showed uniformly distributed densely packed grains with well-defined boundaries. The comparative analysis demonstrated increase in grain size with calcination temperature.
- Magnetic measurements confirmed enhancement in saturation magnetization value owing to the suppression of spin spiral structure by oxygen vacancies as the divalent ion ($Sr^{2+}$) substitutes the trivalent ($Bi^{3+}$) sites. Further, the magnetism of this system enhances on reducing the particle size as it increases surface to volume ratio and, consequently

increasing the number of uncompensated spins contributing towards the magnetization.

- Sr-doping in $BiFeO_3$ lattice degrades the dielectric and ferroelectric properties. The attributed reason is the creation of oxygen vacancies due to the doping of $Sr^{2+}$ (divalent) ions at the trivalent ($Bi^{3+}$) site for maintaining the charge neutrality. Particle size variation has been observed to influence both the dielectric as well as ferroelectric behaviour of Sr-doped $BiFeO_3$ nanoparticles. These enhance with the reducing particle size as the nanosized grains present in the nanoparticles act as insulating barrier for the mobile charge carriers.

**3. Ba-doped $BiFeO_3$ nanoparticles ($Bi_{1-x}Ba_xFeO_3$; x = 0, 0.15)**

- Sol-gel method was employed for the synthesis of Ba-doped $BiFeO_3$ nanoparticles.
- XRD patterns showed that Ba-substitution resulted in no structural transformation of rhombohedral phase of undoped $BiFeO_3$.
- TEM micrographs exhibited agglomerated nanoparticles of irregular morphology due to the high surface energy of the nanoparticles. The agglomeration decreases as the particle size increases. The average particle size has been found out to be 31, 19, 53, and 74 nm, respectively, for Bi4, Ba4, Ba5 and Ba6 nanoparticles.
- FEG SEM micrographs reveal uniformly distributed densely packed spherical grains having well-defined boundaries that indicate crystalline nature of all the synthesized nanoparticles. The smaller grains were observed to coalesce via grain

boundaries to form bigger grains on increasing calcination temperature of Ba-doped $BiFeO_3$ nanoparticles.

- Magnetic analysis showed enhancement in saturation magnetization value with Ba-doping, as the substitution of divalent ion ($Ba^{2+}$ ions) at trivalent ($Bi^{3+}$ ions) sites creates oxygen vacancies, which suppress spin spiral structure of $BiFeO_3$. The saturation magnetization value was further observed to enhance on reducing the particle size of Ba-doped $BiFeO_3$ nanoparticles. The reduction in particle size results in the increasing surface to volume ratio, which, thus, increases the density of the uncompensated spins on the particle surface contributing towards the magnetism.

- The dielectric and ferroelectric properties were found to degrade with Ba-doping owing to the creation of well known source of conductivity i.e. oxygen vacancies as the divalent ions ($Ba^{2+}$) substitutes at the trivalent site ($Bi^{3+}$). Further, these properties witness enhancement on reducing the particle size of the Ba-doped $BiFeO_3$ nanoparticles; the reason the nanosized grains providing insulation to the conduction of charge carriers. The smaller grains obstruct the conductivity of the mobile ions better than the larger grains and hence, improve the dielectric constant and ferroelectric property of the system.

Table 5.3 summarises a comparison of structural, magnetic and electric parameters obtained for the alkaline earth (Ca, Sr, Ba) doped-$BiFeO_3$ nanoparticles

Table 5.3 A comparison of structural, magnetic and electric parameters obtained for the alkaline earth (Ca, Sr, Ba) doped-$BiFeO_3$ nanoparticles

| Property → / Sample ↓ | | Structural parameters | | | | | Magnetic parameters | | | Electric parameters | | | | |
|---|---|---|---|---|---|---|---|---|---|---|---|---|---|---|
| | | D nm | a Å | b Å | c Å | V $Å^3$ | $M_s$ emu/g | $H_{eb}$ Oe | $M_{shift}$ emu/g | $\varepsilon$ Loss @ 0.1 kHz | | $P_r$ μC/$cm^2$ | $P_s$ μC/$cm^2$ | $E_c$ kV/cm |
| $Bi_{1-x}Ca_xFeO_3$ (x = 0, 0.15) | U4 | 15.0 | 5.570 | 5.570 | 13.89 | 373.13 | 1.29 | 17.4 | 0.0170 | 733 | 0.3 | 2.02 | 1.43 | 4.07 |
| | Ca4 | 10.4 | 5.580 | 5.580 | 13.77 | 372.05 | 7.68 | 0.40 | 0.0050 | 1678 | 3.6 | 3.32 | 2.50 | 3.47 |
| | Ca5 | 20.6 | 5.540 | 5.540 | 13.60 | 362.74 | 2.58 | 0.38 | 0.0030 | 642 | 1.3 | 0.48 | 0.50 | 5.85 |
| | Ca6 | 21.3 | 5.560 | 5.560 | 13.65 | 365.76 | 0.91 | 0.25 | 8.4E-4 | 474 | 1.7 | 0.61 | 0.36 | 5.61 |
| $Bi_{1-x}Sr_xFeO_3$ (x = 0, 0.15) | B4 | 21.3 | 5.570 | 5.570 | 13.84 | 373.06 | 2.50 | 0.69 | 0.0035 | 699 | 0.4 | 2.50 | 2.40 | 19.40 |
| | Sr4 | 15.3 | 5.590 | 5.590 | 13.78 | 373.63 | 5.30 | 0.28 | 0.2171 | 654 | 1.0 | 1.60 | 1.00 | 3.30 |
| | Sr5 | 16.7 | 5.610 | 5.610 | 13.69 | 373.60 | 3.90 | 0.01 | 0.0015 | 551 | 1.2 | 1.40 | 0.80 | -7.40 |
| | Sr6 | 20.2 | 5.590 | 5.590 | 13.76 | 372.54 | 1.10 | 6.20 | 0.0005 | 93 | 2.2 | 0.80 | 0.40 | 3.60 |
| $Bi_{1-x}Ba_xFeO_3$ (x = 0, 0.15) | Bi4 | 35.5 | 5.554 | 5.554 | 13.72 | 423.28 | 2.50 | 0.23 | 0.0400 | 697 | 0.4 | 2.67 | 2.24 | 20.03 |
| | Ba4 | 15.0 | 5.556 | 5.556 | 13.73 | 423.83 | 4.40 | 0.32 | 0.0600 | 595 | 1.6 | 1.07 | 0.68 | 12.20 |
| | Ba5 | 19.3 | 5.563 | 5.563 | 13.75 | 425.52 | 3.60 | 0.20 | 0.0200 | 153 | 3.4 | 33.61 | 34.22 | 2.23 |
| | Ba6 | 32.5 | 5.567 | 5.567 | 13.78 | 427.06 | 0.60 | 16.06 | 0.0120 | 33 | 0.6 | 59.50 | 59.33 | 2.15 |

## 5.2 Future Scope

The work can be further extended to study the influence of different nanostructures on the multiferroic properties of doped-$BiFeO_3$ at nanoscale. It is motivated by the fact that varying shape as well as dimensionality has a critical role in determining the properties of a material owing to the different ways the electrons interact in three-dimensional, two-dimensional and one- dimensional structures. This has had pronounced effects on the multiferroic properties of $BiFeO_3$ and thus the size investigations on the multiferroic properties of doped $BiFeO_3$ can be studied. Various dopants, such as rare earth, alkaline earth, transition metals, can be studied as each category of dopants has its own influence on multiferroism of $BiFeO_3$. The particle size investigation of multiferroic properties of co-doped $BiFeO_3$ nanoparticles is another possibility. Also, a number of parameters influence the multiferroics properties of $BiFeO_3$, such as (i) synthesis method, (ii) particle size varying method, (iii) site of doping, (iv) nature of dopant, (v) dopant size. All these parameters need to be comprehensively analysed.

## References


1. H.C. Oersted, A. Larsen, The Discovery of Electromagnetism made in the Year 1820, H.H. Thieles Bogtr., USA, 1920.
2. C. A. F. Vaz, H. Jason, H. A. Charles, R. Ramesh, Adv. Mater. **22** (2010) 2900 - 2918.
3. N. A. Spaldin, S. W. Cheong, R. Ramesh, Phys. Today **63** (2010) 38-43.
4. R. Ramamoorthy, Nature **461** (2009) 1218-1219.
5. D. Khomskii, Phys. **2** (2009) 20.
6. N. A. Hill, J Phys. Chem. B **104** (2000) 6694-6709.
7. Y. Xu, Ferroelectric Materials ad Their Applications, Elsevier, USA, 2013.
8. A. D. Maynard, R. J. Aitken, T. Butz, V. Colvin, K. Donaldson, G. Oberdörster, S.S. Tinkle, Nature **444** (2006) 267-269.
9. G. Vimal, K. P. Mani, D. Alexander, P. R. Biju, N. V. Unnikrishnan, M. A. Ittyachen, C. Joseph, Opt Mater. **50** (2015) 220-228.
10. M.L. Singla, M. Kumar, J Lumin. **129** (2009) 434–438.
11. A. S. Ahmed, M.L. Singla, S. Tabassum, A. H. Naqvi, A. Azam, J Lumin. **131** (2011) 1–6.
12. M. K. Kushwaha, A. Sil, S. Ray, J Nanosci. Nanotechno. **8** (2008) 4152-4158.
13. K. Rana, A. Sil, S. Ray, Adv. Mater. Res. **67** (2009) 197-202.
14. G. Singh, A. Panwar, A. Sil, S. Ghosh, Adv. Matrer. Res. **67** (2009) 227-232.
15. B.S. Murty, P. Shankar, Baldev Raj, B. B. Rath, James Murday, Textbook of Nanoscience and Nanotechnology, Springer, India, 2013.
16. M. Wilson, K. Kannangara, G. Smith, M. Simmons and B. Raguse, Nanotechnology: Basic Science and Emerging Technologies, CRC Press, USA, 2002.
17. M. A. Ratner and D. Ratner Nanotechnology: A Gentle Introduction to the Next Big Idea, Prentice Hall Professional, 2003.

18. G. Cao, Nanostructures and Nanomaterials: Synthesis, Properties, and Applications, Imperial College Press, London, 2004.
19. E. L. Wolf, Nanophysics and Nanotechnology: An Introduction to Modern Concepts in Nanoscience, John Wiley & Sons, Germany, 2015.
20. D. A. Dana, The Nanotechnology Challenge: Creating Legal Institutions for Uncertain Risks, Cambridge University Press, USA, 2011.
21. P. Uniyal, K. L. Yadav, J Alloy Compd. **511** (2012) 149-153.
22. P. Uniyal, K. L. Yadav, J Phys. Condens. Matter **21** (2008) 012205 1-4.
23. M. Alguero, Nanoscale Ferroelectrics and multiferroics: Key processing and characterization issues, and nanoscale effects, John Wiley & Sons, USA, 2016.
24. A. Saxena, A. Planes, Mesoscopic Phenomena in Multifunctional Materials: Synthesis, Characterization, Modeling and Applications, Springer, USA, 2014.
25. W. Eerenstein, N. D. Mathur, J. F. Scott, Nature, **442** (2006) 759-765.
26. H. Schmid, Ferroelectrics, **162** (1994) 317-338.
27. H. Bea, M. Gajek, M. Bibes, A. Barthèlèmy, J. Phys. Condens. Matter. **20** (2008) 434221.
28. N. A. Hill, Annu. Rev. Mater. Res. **32** (2002) 1–37.
29. G. Catalan, J. F. Scott, Adv. Mater. **21** (2009) 2463–2485.
30. W. Prellier, M. P. Singh, P. Murugavel, J. Phys. Condens. Matter, **17** (2005) R803–R832.
31. M. K. Singh, Y. Yang, C. G. Takoudis, Coordin. Chem. Rev. **253** (2009) 2920–2934.
32. L. L. Mitoseriu, Bol. Soc. Esp. Ceram. V. **44** (2005) 177-184.
33. M. Fiebig, J. Phys. D Appl. Phys. **38** (2005) R123–R152.
34. D. I. Khomskii, J. Mag. Mag. Mat. **306** (2006) 1-8.

35. S. Toyoda, N. Abe, S. Kimura, Y. H. Matsuda, T. Nomura, A. Ikeda, S. Takeyama, T. Arima, Phys. Rev. Lett. **115** (2015) 267207.

36. J.V. D. Brink, D. I. Khomski, J. Phys.: Condens. Matter. **20** (2008) 434217.

37. D. Schumacher, Interplay between Magnetic and Dielectric Phenomena at Tranistion Metal Oxide Interfaces, Forschungszentrum Julich, Germany, 2013.

38. A. Roy, R. Gupta, A. Garg, Adv. Condens. Matter. Phys. **926290** (2012) 1-12.

39. J. F. Scott, Nature Mat. **6** (2007) 256 – 257.

40. R. Palai, R. S. Katiyar, H. Schmid, P. Tissot, S. J. Clark, J. Robertson, S. A. T. Redfern, G. Catalan, J. F. Scott, Phys. Rev. B **77** (2008) 014110.

41. D. S. Jeong, R. Thomas, R. S. Katiyar, J. F. Scott, H. Kohlstedt, A. Petraru, Rep. Prog. Phy. **75** (2012) 076502.

42. A. K. Pradhan, K. Zhang, D. Hunter, J. B. Dadson, G. B. Loutts, P. Bhattacharya, R. Katiyar, J. Zhang, D. J. Sellmyer, U. N. Roy, Y. Cui, A. Burger, J. Appl. Phys. 97 (2005) 093903.

43. L. W. Martin, S. P. Crane, Y. H. Chu, M. B. Holcomb, M. Gajek, M. Huijben, C. H. Yang, N. Balke, R. Ramesh, J. Phys. Condens. Matter. **20** (2008) 434220.

44. M. K. Niranjan, J. P. Velev, C. G. Duan, S. S. Jaswal, E. Y. Tsymbal, Phys. Rev. B **78** (2008) 104405.

45. G. Lawes, G Srinivasan, J. Phys. D Appl. Phys. **44** (2011) 243001.

46. I. E. Dzyaloshinskii, Sov. Phys. JETP **10** (1959) 628-629.

47. D. N. Astrov, Sov. Phys. JETP **11** (1609) 708.

48. C. H. Yang, D. Kan, I. Takeuchi, V. Nagarajan, J. Seidel, Phys. Chem. Chem. Phys. **14** (2012) 15953-15962.

49. G. A. Smolensky, V. A. Isupov, A. I. Agronovskaya, Sov. Phys. Solid State **1** (1959) 149-150.

## References


50. G.D. Achenbach, W.J. James, R. Gerson, Am. J. Ceram. Soc. **50** (1967) 437-437.

51. S. V. Kiselev, R. P. Ozerov, G. S. Zhdanov, Sov. Phys. Dokl. **7** (1963) 742-744.

52. C. Michel, J. M. Moreau, G. D. Achenbach, R. Gerson, W. J. James, Solid State Commun. **7** (1969) 701-704.

53. J. Wang, J. B. Neaton, H. Zheng, V. Nagarajan, S. B. Ogale, B. Liu, D. Viehland, V. Vaithyanathan, D. G. Schlom, U. V. Waghmare, N. A. Spaldin, K. M. Rabe, M. Wuttig, R. Ramesh, Sci. **299** (2003) 1719-1721.

54. D. Lebeugle, D. Colson, A. Forget, M. Viret, Appl. Phys. Lett. **91** (2007) 022907.

55. A. M. Kadomtseva, Y. F. Popov, A. P. Pyatakov, G. P. Vorob'ev, A. K. Zvezdin, D. Viehland, Phase Transit. **79** (2006) 1019–1042.

56. A. Lubk, S. Gemming, N. A. Spaldin, Phys. Rev. B **80** (2009) 104110.

57. Y. Jian, C. JunHao, Chinese Sci. Bull. **53** (2008) 2097-2112.

58. K. F. Wang, J. M. Liu, Z. F. Ren. Adv. Phys. **58** (2009) 321-448.

59. Y. H. Chu, L. W. Martin, M. B. Holcomb, R. Ramesh, Mater. Today **10** (2007) 16-23.

60. S. V. V. Khikhlovskyi, G. Blake. University of Groningen (2010).

61. T. Zhao, A. Scholl, F. Zavaliche, K. Lee, M. Barry, A. Doran, M. P. Cruz, Y. H. Chu, C. Ederer, N. A. Spaldin, R. R. Das, Nat. Mater. **5** (2006) 823-829.

62. F. Zavaliche, P. Shafer, R. Ramesh, M. P. Cruz, R. R. Das, D. M. Kim, C. B. Eom, Appl. Phys. Lett. **87** (2005) 252902.

63. S. M. Selbach, T. Tybell, M. A. Einarsrud, T. Grande, Adv. Mater. **20** (2008) 3692–3696.

64. I. Sosnowska, T. P. Neumaier, E. Steichele, J. Phys. C Solid State Phys. **15** (1982) 4835-4846.

65. C. Ederer, N. A. Spaldin, Phys. Rev. B **71** (2005) 060401.

66. I. Sosnowska, M. Loewenhaupt, W.I. F. Davie, R. M. Ibberson, Physica B **180** (1992) 117-118.

67. Y. A. Chaudhari, A. Singh , C. M. Mahajan, P. P. Jagtap, E. M. Abuassaj, R. Chatterjee, S. T. Bendre, J. Magn. Magn. Mater. **347** (2013) 153–160.

68. A. Singh, R. Chatterjee, S. K. Mishra, P. S. R. Krishna, S. L. Chaplot, J. Appl. Phys. **111** (2012) 014113.

69. S. Dutta, A. Pandey, I. Yadav, O. P. Thakur, R. Laishram, R. Pal, R. Chatterjee, J. Appl. Phys. **112** (2012) 084101.

70. A. Singh, R. Chatterjee, Ferroelectrics **433** (2012) 180-189.

71. S. K. Srivastav, N. S. Gajbhiye, J Am. Ceram. Soc. **95** (2012) 3678-3682.

72. R. K. Mishra, D. K. Pradhan, R. N. P. Choudhary, A. Banerjee, J Phys. Condens. Matter. **20** (2008) 045218.

73. P. Curie, J. Physique **3** (1894) 393-416.

74. L. D. Landau, E. M. Lifshitz, Pergamon Press **16** (1961) 359-360.

75. G. A. Smolenskii, I. E. Chupis, Sov. Phys. Usp. **25** (1982) 475-482.

76. G. S. Lotey, N. K. Verma, J. Nanopart. Res. **14** (2012) 1-11.

77. G. S. Lotey, N. K. Verma, Superlattice. Microst. **53** (2012) 184-194.

78. M. Starucha, D. Violette, M. Jain, Mater. Chem. Phys. **139** (2013) 897-900.

79. P. Uniyal, K. L. Yadav, Mater. Lett. **62** (2008) 2858-2861.

80. S. Karimi I. M. Reaney, Y. Han, J. Pokorny, I. Sterianou, J Mater. Sci. **44** (2009) 5102-5112.

81. X. Zhang, Y. Sui, X. Wang, Y. Wang, Z. Wang, J Alloys Compd. **507** (2010) 157-161.

82. P. Pandit, S. Satapathy, P. K. Gupta, Physica B **406** (2011) 2669-2677.

83. F. Yan, M. O. Lai, Li. Lu, J. Phys. D Appl. Phys. **45** (2012) 325001.

84. V. A. Khomchenko, D. A. Kiselev, I. K. Bdikin, V. V. Shvartsman, P. Borisov, Appl. Phys. Lett. **93** (2008) 262905.

85. S. K. Pradhan, B. K. Roul, J Phys. Chem. Solids **72** (2011) 1180-1187.

86. B. Yu, M. Li, J. Wang, L. Pei, D. Guo, X. Zhao, J Phys. D Appl. Phys. **41** (2008) 185401.

87. B. Yu, M. Li, Z. Hu, L. Pei, D. Guo, X. Zhao, S. Dong, Appl. Phys. Lett. **93** (2008) 182909.

88. N. Jeon, D. Rout, I. W. Kim, S. J. L. Kang, Appl. Phys. Lett. **98** (2011) 072901.

89. O. P. Thakur, C. Prakash, D. K. Agrawal, Mater. Lett. **56** (2006) 970-973.

90. N. Masó, A. R. West, Chem. Mater. **24** (2012) 2127-2132.

91. G. Catalan, K. Sardar, N. S. Church, J. F. Scott, R. J. Harrison, S. A. T. Redfern, Phys. Rev. B **79** (2009) 212415.

92. V. A. Khomchenko, D. A. Kiselev, M. Kopcewicz, M. Maglione, V. V. Shvartsman, P. Borisov, W. Kleemannd, A. M. L. Lopes, Y. G. Pogorelov, J. P. Araujo, R. M. Rubinger, N. A. Sobolev, J. M. Vieira, A. L. Kholkin, J. Magn. Magn. Mater. **321** (2009) 1692-1698.

93. I. O. Troyanchuk, D. V. Karpinsky, M. V. Bushinskii, O. Prokhnenko, M. Kopceviczc, R. Szymczak, J. Pietosa, J Appl. Phys. **112** (2012) 073516.

94. B. Ramachandran, M. S. Ramachandra, J Phys.: Condens. Matter. **24** (2012) 045905.

95. K. Sardar, J. Hong, G. Catalan, P. K. Biswas, M. R. Lees, R. I. Walton, J. F. Scott, S. A. T. Redfern, J Phys.: Condens. Matter. **24** (2012) 045905.

96. D. H. Wang, W. C. Goh, M. Ning, C. K. Ong, Appl. Phys. Lett. **88** (2006) 212907.

97. A. Gautam, V. S. Rangra, Cryst. Res. Technol. **45** (2010) 953-956.

98. R. Das, K. Mandal, J. Magn. Magn. Mater. **324** (2012) 1913-1918.

99. O. P Thakur, C. Prakash, D. K Agrawal, Mater. Sci. Eng. B **96** (2002) 221-225.

100. J. Wei, R. Haumont, R. Jarrier, P. Berhtet, B. Dkhil, Appl. Phys. Lett. **96** (2010) 102509.

101. P. Kharel, S. Talebi, B. Ramachandran, A. Dixit, V. M. Naik, M. B. Sahana, C. Sudakar, R. Naik, M. S. R. Rao, G. Lawes, J. Phys. Condens. Matter **21** (2009) 036001.

102. I. O. Troyanchuk, A. N. Chobot, O. S. Mantytskaya, N. V. Tereshko, Inorg. Mater. **46** (2010) 424-428.

103. Q. Xu, H. Zai, D. Wu, T. Qiu, M. X. Xu, Appl. Phys. Lett. **95** (2009) 112510.

104. M. Kumar, K. L. Yadav, Appl. Phys. Lett. **91** (2007) 242901.

105. Y.A. Chaudhari, A. Singh, E.M. Abuassaj, R. Chatterjee, S. T. Bendre, J. Alloys Compd. **518** (2012) 51-57.

106. R. Mazumder, S. Ghosh, P. Mondal, D. Bhattacharya, S. Dasgupta, N. Das, A. Sen, J. Appl. Phys. **100** (2006) 033908.

107. R. Mazumder, P. S. Devi, D. Bhattacharya, P. Choudhury, A. Sen, Appl. Phys. Lett. **91** (2007) 062510.

108. S. M. Selbach, T. Tybell, Ma. A. Einarsrud, T. Grande, Chem. Mater. **19** (2007) 6478-6484.

109. F. Gao, X. Chen, K. Yin, S. Dong, Z. Ren, F. Yuan, T. Yu, Z. Zou, J. M. Liu, Adv. Mater. **19** (2007) 2889-2892.

110. T. J. Park, G. C. Papaefthymiou, A. J. Viescas, A. R. Moodenbaugh, S. S. Wong, Nano Lett. **7** (2007) 766-772.

111. I. Apostolova, A. T. Apostolov, J. M. Wesselinowa, J. Phys. Condens. Matter **21** (2009) 036002.

112. S. Li, Y. H. Lin, B. P. Zhang, C. We. Nan, Y. Wang, J. Appl. Phys. **105** (2009) 056105.

113. S. Vijayanand, M. B. Mahajan, H. S. Potdar, P. A. Joy, Phys. Rev. B: Condens. Matter **80** (2009) 064423.

114. T. Liu, J. Am. Ceram. Soc. **93** (2010) 3637-3641.

115. A. Jaiswal, R. Das, T. Maity, K. Vivekanand, S. Adyanthaya, P. Poddar, J. Phys. Chem. C **114** (2010) 12432-12439.

116. P. Chen, X. Xu, C. Koenigsmann, A. C. Santulli, S. S. Wong, J. L. Musfeldt, Nano Lett. **10** (2010) 4526-4532.

117. A. Jaiswal, R. Das, K. Vivekanand, P. M. Abraham, S. Adyanthaya, P. Poddar, J. Phys. Chem. C **114** (2010) 2108-2115.

118. H. Yang, T. Xian, Z. Q. Wei, J. F. Dai, J. L. Jiang, W. J. Feng, J. Sol-Gel. Sci. Technol. **58** (2011) 238-243.

119. S. Goswami, D. Bhattacharya, P. Choudhury, J. App. Phys. **109** (2011) 07D737.

120. M. E. Castillo, V. V. Shvartsman, D. Gobeljic, Y. Gao, J. Landers, H. Wende and D. C. Lupascu, Nanotechnology **24** (2013) 355701.

121. L. C. Wang, Z. -H. Wang, S. L. He, X. Li, P. T. Lin, J. R. Sun, B. G. Shen, Physica B **407** (2012) 1196–1202.

122. S. K. Pradhan, B. K. Roul, J Sol-Gel Sci Technol **64** (2012) 375–380.

123. Z. Liu, Y. Qi, C. Lu, J Mater Sci: Mater Electron **21** (2010) 380–384.

124. P. P. Nampi, C. C. Kartha, G. Jose, A. K. Anil, T. A. Kumar, H. B. Varma, Chemical. **185** (2013) 252-257.

125. G. Jose, V. Thomas, C. Joseph, M. A. Ittyachen, N. V. Unnikrishnan, J Fluoresc. **14** (2004) 733-738.

126. S. Slavov, M. Krapchanska, E. Kashchieva, S. Parvanov, Y. Dimitriev, J. Chem. Technol. **48** (2013) 174-178.

127. P. E. Kashchieva, Z. M. Krapchanska, S. Stanislav S. Slavov, Yanko B. Dimitriev, Proc. Appl. Ceram. **3** (2009) 1-6.

128. S. Y. Limaye, D. K. Agrawa, R. Roy, Y. Mehrotra, J. Mater. Sci. **26** (1991) 93-98.

129. Y. Wang, Ce-Wen Nan, J. Appl. Phys. **103** (2008) 024103.

130. F. Z. Qian, J. S. Jiang, S. Z. Guo, D. M. Jiang, W. G. Zhang, J. Appl. Phys. **106** (2009) 084312.

131. J. Liu, L. Fang, F. Zheng, S. Ju, M. Shen, App. Phys. Lett. **95** (2009) 022511.

132. R. Guo, L. Fang, W. Dong, F. Zheng, M. Shen, J. Phys. Chem. C **114** (2010) 21390–21396.

133. K. Chakrabarti, K. Das, B. Sarkar, S. K. De, J. App. Phys. **110** (2011) 103905.

134. W. Hu, Y Chen, H. Yuan, G. Li, Y. Qiao, Y. Qin, S. Feng, J. Phys. Chem. C **115** (2011) 8869–8875.

135. B. Bhushan, Z. Wang, J. V. Tol, N. S. Dalal, A. Basumallick, N. Y. Vasanthacharya, S. Kumar, D. Das, J. Am. Ceram. Soc. **95** (2012) 1985–1992.

136. J. W. Lin, T. Tite, Y. H. Tang, C. S. Lue, Y. M. Chang, J. G. Lin, J. App. Phys. **111** (2012) 07D910.

137. B. Bhushan, A. Basumallick, S. K. Bandopadhyay, N. Y. Vasanthacharya, D. Das,J. Phys. D Appl. Phys. **42** (2009) 065004.

138. B. Wang, S. Wang, L. Gong, Z. Zhou, Ceram. Int. **38** (2012) 6643–6649.

139. J. Li, D. Cai, J. Song, D. Jin, S. Yu, J. Cheng, IEEE International Symposium on the Applications of Ferroelectrics (ISAF) , (2010) 1-4.

140. C. Yang, C. Z. Liu, C. M. Wang, W. G. Zhang, J. S. Jiang, J. Magn. Magn. Mater. **324** (2012) 1483–1487.

141. B. Bhushan, D. Das, A. Priyam, N. Y. Vasanthacharya, S. Kumar, Mater. Chem. and Phys. **135** (2012) 144-149.

142. Y. N. Feng, H. C. Wang, D. Y. Luo, Y. Shen, H. Y. Lin, J. Appl. Phys.**113** (2013) 146101.

143. M. M. El-Desoky, M. M. Mostafa, M. S. Ayoub, M. A. Ahmed, J. Mater. Sci. Mater. Electron. **26** (2015) 6793-6800.

144. X. Wang, S. Y. Wang, W. F. Liu, X. J. Xi, H. Zhang, F. Guo, X. L. Xu, J. Nanopart. Res. **17** (2015) 1-14.

145. S. Chauhan, M. Kumar, S. Chhoker, S. C. Katyal, H. Singh, M. Jewariya, K. L. Yadav, Solid State Commun. **152** (2012) 525–529.

146. R. Das, G. G. Khan, K. Mandal, J. Appl. Phys. **111** (2012) 104115.

147. D. P. Dutta, O. D. Jayakumar, A. K. Tyagi, K. G. Girija, C. G. S. Pillai, G. Sharma, Nanoscale **2** (2010) 1149–1154.

148. F. Yan, M.O. Lai, Li Lu, J. Phys. D Appl. Phys. **45** (2012) 325001.

149. P. Tirupathi, A. Chandra, Phys. Status Solidi B **249** (2012) 1639–1645.

150. A. Mukherjee, M. Banerjee, S. Basu, M.D. Mukadam, S.M. Yusuf, M. Pal, Mater. Chem. Phys. **162** (2015) 140-148.

151. G. S. Lotey, N. K. Verma, Mater. Lett. **111** (2013) 55–58.

152. F. Z. Qian, J. S. Jiang, D. M. Jiang, W. G. Zhang, J. H. Liu, J. Phys. D Appl. Phys. **43** (2010) 025403.

153. S. K. Mandal, T. Rakshit, S. K. Ray, S. K. Mishra, P. S. R. Krishna, A. Chandra, J. Phys. Condens. Matter **25** (2013) 055303.

154. L. L. Hench, J. K. West, Chem. Rev. **90** (1990) 33-72.

155. S. Sakka, Handbook of Sol-Gel Science and Technology III: Applications of Sol-Gel Technology, Kluwer Academic Publishers, USA, 2005.

156. C. J. Brinker, G. W. Scherer, Sol-Gel Science, The Physics and Chemistry of Sol-Gel Processing, Academic Press, Inc., UK, 1990.

157. https://www.llnl.gov/str/May05/Satcher.html (last accessed 14-7-14)

158. M. Birkholz, Thin Film Analysis by X-Ray Scattering, Wiley-vch, Weinheim, 2006.

159. https://www.google.co.in/search?q=bragg%27s+law+diagram&newwindow=1&tbm=isch&imgil=OthoXYdSpI9wWM%253A%253BfznSJo6pR1Vl4M%253Bhttp%25253A%25252F%25252Fhyperphysics.phy-astr.gsu.edu%25252Fhbase%25252Fquantum%25252Fbragg.html&source=iu&pf=m&fir=OthoXYdSpI9wWM%253A%252CfznSJo6pR1Vl4M%252C_&usg=__D9mHGH2P6b-ab_RamDIGpqyzO9g%3D&biw=1366&bih=625&ved=0ahUKEwi2yZqJtIHOAhUW_WMKHelVBkMQyjcIMA&ei=IBmPV7a5GJb6jwPpq5mYBA (last accessed 20-7-16)

160. B. Fultz, J. M. Howe, Transmission Electron Microscopy and Diffractometry of Materials, Springer, London, 2001.

161. http://serc.carleton.edu/research_education/geochemsheets/techniques/XRD.html (last accessed 21-7-16)

162. http://www.ebah.com.br/content/ABAAAga1YAA/apostila-drx-continuacao (last accessed 21-7-16)

163. http://swes.cals.arizona.edu/rasmussen/lab3.htm (last accessed 21-7-16)

164. B.D. Cullity, Elements of X-Ray Diffraction, Addison-Wesley Publishing Company, Inc., USA, 1956.

165. B. L. Gabriel, Sem: A User's Manual for Materials Science, American Society for Metals, USA, 1985.

166. http://www.google.co.in/imgres?imgurl=http%3A%2F%2Fwww.ammrf.org.au%2Fmyscope%2Fimages%2Fsem%2Fvolumes08.png&imgrefurl=http%3A%2F%2Fwww.ammrf.org.au%2Fmyscope%2Fsem%2Fbackground%2Fconcepts%2Finteractions.php&docid=PkD_IiQTW1O_IM&tbnid=O8igd3wv6h8MjM&w=480&h=364&ei=fZncVL_ZBYmzuASdyoDoBw&ved=0CAQQxiAwAg&iact=c (last accessed 21-7-16)

167. https://www.google.co.in/search?q=working+principle+of+sem&biw=1366&bih=622&source=lnms&tbm=isch&sa=X&ved=0ahUKEwiYkd6404POAhVCuI8KHZekA8UQ_AUIBigB#imgrc=W66m7g6boaxTdM%3A (last accessed 21-7-16)

168. http://www.google.co.in/imgres?imgurl=https://roilbilad.files.wordpress.com/2010/10/sem.jpg&imgrefurl=http://www.wdyl.com/%23sem&h=1133&w=1297&tbnid=Xc4YGTfaoxLQHM:&zoom=1&docid=T7QaYydA5lVyM&ei=tZbcVP3mMoaj8AXP9YDQAg&tbm=isch&ved=0CDIQMygAMAA (last accessed 21-7-16)

169. http://serc.carleton.edu/research_education/geochemsheets/techniques/SEM.html (last accessed 21-7-16)

170. http://www.microscopemaster.com/scanning-electron-microscope.html (last accessed 21-7-16)

171. W. Zhou, Z. L. Wang, Scanning Microscopy for Nanotechnology: Techniques And Applications, Springer Science & Business Media, USA, 2007.

172. D. B. Williams, C. Barry Carter, Transmission Electron Microscopy: A Textbook for Materials Science, Springer Science Business Media, USA, 2009.

173. http://www.microscopemaster.com/transmission-electron-microscope.html (last accessed 21-7-16)

174. S. J. Pennycook, P. D. Nellist, Scanning Transmission Electron Microscopy: Imaging and Analysis, Springer Science Business Media, USA, 2011.

175. http://www.britannica.com/EBchecked/topic/602949/transmission-electron-microscope-TEM (last accessed 21-7-16)

176. http://www.google.co.in/imgres?imgurl=http://nptel.ac.in/courses/102103044/module3/lec18/images/1.png&imgrefurl=http://nptel.ac.in/courses/102103044/18&h=426&w=528&tbnid=26vdULrqiUk0WM:&zoom=1&docid=arABWR82RF8xgM&ei=Df_uVM_MNJSluQSStoCIDw&tbm=isch&ved=0CFAQMygqMCohttp://cbe.ivic.ve/mic250/pdf/thesebook-chap3.pdf (last accessed 21-7-16)

177. http://www.google.co.in/imgres?imgurl=http://konawaenahs.k12.hi.us/tem.jpg&imgrefurl=http://konawaenahs.k12.hi.us/Ms.%2520Martin%27s%2520Physics.htm&h=1712&w=1368&tbnid=kOWSBQZpzHfJ_M:&zoom=1&docid=CazuaEw3Rk_svM&ei=Df_uVM_MNJSluQSStoCIDw&tbm=isch&ved=0CGQQMyg-MD4 (last accessed 21-7-16)

## References


178. D. Jiles, Introduction to Magnetism and Magnetic Materials, CRC Press, USA, 2015.

179. B. D. Cultiy, C. D. Graham, Introduction to Magnetic Materials, IEEE press, Wiley a Johnson Wiley & Sons, Inc., USA, 2011.

180. W. Burgei, M. J. Pechan, H. Jaeger, Am. J. Phys. **71** (2003) 825-828.

181. http://family-held.org/website/Rudy/publications/unpublished/papers/vsm/VMS%20Paper.htm (last accessed 21-7-16)

182. http://iramis.cea.fr/Phocea/Vie_des_labos/Ast/ast_sstechnique.php?id_ast=498 (last accessed 21-7-16)

183. http://www3.imperial.ac.uk/pls/portallive/docs/1/11949698.PDF (last accessed 21-7-16)

184. http://www.radio-electronics.com/info/t_and_m/lcr-meter/basics-tutorial.php (last accessed 21-7-16)

185. http://www.murata.com/~/media/webrenewal/products/emiconfun/capacitor/2012/06/28/en-20120628-p1/sokutei.ashx (last accessed 21-7-16)

186. A. R. V. Hippel, A. S. Labounsky, Dielectric Materials and Applications, Artech House, London, 1995.

187. https://www.testworld.com/used-electronic-test-equipment/keysight-agilent-lcr-impedance-testers/keysight-agilenthp-4284a-precision-lcr-meter-20-hz-1-mhz/ (last accessed 21-7-16)

188. V. Raghavan, Material Science and Engineering: A First Course, PHI Learning Private Limited, New Delhi, 2004.

189. J. K. Sinha, J Sci. Instrum. **42** (1965) 696-698.

190. S. C. Das, A. Shahee, N. P. Lalla, T. Shripathi, Proceedings of the 54th DAE Solid State Physics Symposium, **54** (2009) 439-440.

191. K. M. Rabe, C. H. Ahn, J. M. Triscone, Physics of Ferroelectrics: A Modern Perspective, Springer, USA, 2007.

192. K. D. Sattler, Handbook of Nanophysics: Nanoelectronics and Nanophotonics, CRC press: Taylor and Francis group, USA, 2011.

193. R. Waser, U. Böttger, S. Tiedke, Polar Oxides: Properties, Characterization, and Imaging, Wiley-VCH, Weinheim, 2005.

194. http://www.eah-jena.de/~ploss/lehre/pdf/versuchsanleitungen.pdf (last accessed 21-7-16)

195. http://soauniversity.ac.in/home/research/multifunctional-advanced-materials-research-lab (last accessed 21-7-16)

196. P. Debye, Ann. Phys. **351** (1915) 809-823.

197. L. Khanna, N. K. Verma, J Magn. Magn. Mater. **336** (2013) 1–7.

198. J. Allibe, I. C. Infante, S. Fusil, et al., Appl. Phys. Lett. **95** (2009) 182503.

199. R. Rana, P. Pandey, R. P. Singh et al., Scientific reports **4** (2014).

200. Y.J. Yoo, J.S. Hwang, Y.P. Lee, et al., J Magn. Magn. Mater. **374** (2015) 669-675.

201. J. B. Macchesney, H. J. Williams, R. C. Sherwood, J. F. Potter, J. Chem. Phys. **44** (1966) 596-601.

202. K. Chakrabarti, K. Das, B. Sarkar, S. Ghosh, S. K. De, G. Sinha, J. Lahtinen, Appl. Phys. Lett. **101** (2012) 042401.

203. R. Das, T. Sarkar, K. Mandal, J. Phys. D: Appl. Phys. **45** (2012) 455002.

204. A. Mukherjee, Sk. M. Hossain, M. Pal, S. Basu, Appl. Nanosci. **2** (2012) 305-310.

205. X. Qi, J. Dho, R. Tomov, M. G. Blamire, J. L. M. Driscoll, Appl. Phys. Lett. **86** (2005) 062903.

206. G. S. Lotey, N. K. Verma, J. Mater. Sci. Mater. Electron **24** (2013) 3723-3729.

207. G. Adachi, N Imanaka,Chem. Rev. **98** (1998) 1479-1514.

208. N. Sakai, J. Phys. Conference Series **352** (2012) 012008.

209. V. Pardo, W. E. Pickett, Phys. Rev. B **78** (2008) 134427.

210. P. Priyadharsini, A. Pradeep, B. Sathyamoorthy, G. Chandrasekaran, J. Phys. Chem. Solids **75** (2014) 797–802.

211. Q. Q. Wang, Z. Wang, X. Qiang Liu, X. M. Chen, J. Am. Ceram. Soc. **95** (2012) 670–675.

212. J. Z. Huang, Y. Wang, Y. Lin, M. Li, C. W. Nan, J Appl. Phys. **106** (2009) 063911.